Electrochemical and Electrokinetic Tools for Surface Activity Characterization and Proteomics Analysis

THÈSE N^{O} 4846 (2010)

PRÉSENTÉE LE 25 OCTOBRE 2010

À LA FACULTÉ SCIENCES DE BASE

LABORATOIRE D'ÉLECTROCHIMIE PHYSIQUE ET ANALYTIQUE

PROGRAMME DOCTORAL EN CHIMIE ET GÉNIE CHIMIQUE

ÉCOLE POLYTECHNIQUE FÉDÉRALE DE LAUSANNE

POUR L'OBTENTION DU GRADE DE DOCTEUR ÈS SCIENCES

PAR

Fernando CORTES SALAZAR

acceptée sur proposition du jury:

Prof. C. Comninellis, président du jury
Prof. H. Girault, directeur de thèse
Prof. Z. Ding, rapporteur
Prof. Ph. Renaud, rapporteur
Prof. W. Schuhmann, rapporteur

ÉCOLE POLYTECHNIQUE
FÉDÉRALE DE LAUSANNE

Suisse
2010

The voyage of discovery lies not in seeking new horizons, but in seeing with new eyes…..

Marcel Proust

A mi familia:

Mis padres Gerardino y Nelsa, mis hermanas Andrea y Diana por su apoyo y cariño incondicional durante toda mi vida….

Y mi esposa Sofía que llena cada momento de mi vida con su amor y su alegria....

ACKNOWLEDGEMENTS

First, I want to say thanks to my supervisor Professor Hubert Girault, who not only trusted in my work during all my PhD, but also supported me during difficult moments, while in the good times always keep me busy with all of his great ideas. Thanks to his advices and his encouraging words this thesis was possible.

Secondly, I want to aknowledge to professor Zifheng Ding, professor Philippe Reanud and professor Wolfang Schuhmann, who all three kindly accepted to be part of the jury committee of my PhD. Additionally, I want to thank professor Christos Comminellis for being the president of the jury.

Part of this thesis was developed in collaboration with professor Dr. Gunther Wittstock at the University of Oldenburg. I would like to thank him and his team for all the support provided to me, especially to Markus Träeuble for the BEM simulations presented in chapter 5 and Andreas Lesch for the programming of the SECMx and MIRA softwares and his invaluable friendship.

I am very grateful to Maria Szuman, Valerie Devaud and Anne-lene Odergaard, for all the administrative and technical assistance that they have friendly offered to me during all my PhD. In the same way, I am pleased to all the people of the mechanical and electronic workshop, as well as, to Frederic Gumy for the priceless help provided to me.

I want to express my gratitude to all my former and current colleagues from LEPA, Meiqin, Bin, Fei Li, Hongxu, Melanie, Raheleh, Niels, Jacques, Christophe, Bi, Liang, Yu, Imren, Gaëlle, Brice, Rune and especially to Jean-Marc Busnel for showing me the proteomic world and provided me with a lot of advices and support for my thesis. I want

to give my especial thanks to my officemates Peiyu, Reza and Anne-laure for all the support and friendship that they have given to me and all the moments that we have shared specially the interesting discussions about life. I want to thank Dmitry for his friendship, help and motivation during the last part of my thesis, and for being with Andreas part of the community of the array!. Dmitry kindly provided me with the FEM simulations presented in chapter 7. Of course I cannot forget the Lebanese community of our lab, Momo and Nathalie for all their kindness and help. I am very grateful with Trang an out of category friend, with who I spent very nice moments working in the lab or having dinner in Mc Donalds. To Astrid, Manuel and Ray, for being like a Colombian family for me in Lausanne. Thanks for all the support and nice moments that we have spent together, which I will never forget, even if my memory is not to trust… I want also to thank to Pilar and Pedro my Iberian cousins for the great time that we got together. To all the group members of Maquerule: Erika, Paola, Monica, Amanda, Sandra, Manuela, Adriana, Rosa, Cesar, Alejandro, Wilson, Ricardo y Felician for teaching me some Colombian folkloric dances in Switzerland. To Christopher Chidley for all the running sessions and soccer matches. To Vera for her kindness and her friendship that I hope to treasure for all my life. To the professor Quijano for the confidence and to Jessica for her kindness. To all the Colombian and Latin American community from whom I have a lot of agreeable rememberings.

There are in Colombia a lot of friends that even being far away from Switzerland, always made me feel that I was accompanied by them. Nicolas, Javier, Ivan, Marcela, Esneda, Sandra, Isabel, Elizabeth, Carlos, Oscar, Francisco y Ernesto, thanks for all the unconditional friendship that you have offered to me during almost all my life. To Marco

for introducing me to the electrochemistry word and more important for his invaluable friendship.

I am deeply thankful to the Wist family to Isabelle and Max, as well as, to Hernan and Chata for the kindles offered to me when I arrived to Switzerland and for having always a place for me at their homes.

Well understood, of course I will not forget to express my gratitude to my dear friend Michel, who has encouraged me to pursuit my objective of graduating from the EPFL and to run the marathon. I hope that our friendship will last for a long time.

No solo este trabajo, sino tambien toda mi vida ha sido siempre gracias al apoyo incondicional que mi familia me ha brindado. Ellos son y seguiran siendo la motivacion que me impulsa a intentar hacer las cosas mejor cada dia. Les debo todo a ustedes Mi papa Gerardino, mi Mama Nelsa y mis hermanas Andrea y Diana. Y por supuesto, mi felicidad te la debo toda a ti Sofia, porque un *quizas porque* se convirtio en una *zamba del cielo* y permitio que nuestros caminos se hicieran uno para recorrerlo juntos. Gracias por tu amor, tu alegria y todo el apoyo que me has dado.

RESUME

La microscopie électrochimique à balayage (SECM) est devenue une technique puissante et versatile pour imager la réactivité chimique sur une surface. Par conséquent, ses applications couvrent un large éventail de domaines comme la biologie ou les sciences forensiques. Elle a également trouvé une application intéressante en protéomique, qui est explorée dans ce travail. Il s'agit de l'utilisation de la SECM comme outil de détection pour la micro-séparation de protéines. La recherche en protéomique est un long procédé comportant deux étapes principales: la séparation des protéines provenant d'un mélange et la détection de celles-ci avec une haute sensibilité ainsi qu'une haute sélectivité si nécessaire. Afin de gagner cette course, le temps expérimental de chacune de ces étapes devrait être raccourci tout en conservant voire en améliorant leur qualité. Bien que la micro-électrophorèse permette une séparation plus rapide, la petite quantité d'échantillon utilisé nécessite une méthode de détection très sensible. Dans la première partie de cette thèse, une approche pour pallier cet inconvénient a été développée en couplant une électrophorèse miniaturisée avec la SECM. Une séparation complète de protéines par focalisation isoélectrique miniaturisée (*i.e.* 1 cm *x* 0.5 cm) a été réalisée puis balayée par SECM, fournissant une détection extrêmement sensible ainsi qu'une haute résolution. De plus, la détection par SECM a été réalisée selon différentes stratégies allant d'une approche générale à des approches sélectives basées sur le marquage de cystéines libres et d'autres nucléophiles présents dans les protéines ou peptides par la benzoquinone. Les protéines marquées sont détectées par la réduction de la benzoquinone induite par une espèce redox produite électrochimiquement à la pointe de la SECM. Après une optimisation minutieuse, une sensibilité de l'ordre du ng mm^{-2} a été atteinte pour

l'albumine bovine. Un des principaux avantages de cette technique est que la sélectivité du marquage peut être modulée en changeant le pH du milieu de réaction. Selon les besoins, une détection générale ou sélective à l'aide de cystéine peut donc être obtenue avec une haute sensibilité.

Malgré le gain de temps obtenu en micro-électrophorèse et le couplage avec la SECM pour la détection de protéines, les montages de SECM conventionnels sont limités par un balayage de la zone d'étude ligne par ligne, demandant un temps expérimental considérable. De plus, comme la réponse de la micro-électrode dépend de la distance entre la sonde et le substrat, il n'est pas toujours évident de distinguer la réactivité de la surface d'artéfacts topographiques provenant de la topologie de l'échantillon. Ces inconvénients nous ont motivé à nous y intéresser dans la seconde partie de la thèse. Par conséquent, nous présentons quelques développements récents qui montrent comment la SECM peut être utilisée pour l'analyse de la réactivité de larges surfaces, ondulées, penchées et sèches. Cette extension de la SECM est rendue possible par l'utilisation de micro-électrodes spécialisées fabriquées dans un film polymère souple par exemple et de systèmes microfluidiques pour délivrer des volumes de l'ordre du microlitre de médiateur rédox-actif sur un échantillon sec. Ces structures souples sont ensuite balayées en mode contact sur le substrat et le courant produit par le cycle redox du médiateur est utilisé pour construire une image de la réactivité du spécimen. Grâce à l'utilisation de sondes contenant des électrodes multiplexées, il est possible de diminuer substantiellement le temps d'acquisition de l'image tout en conservant sa qualité. La caractérisation électrochimique de ces sondes a été réalisée par voltamétrie cyclique, par des courbes

d'approche et des balayages latéraux sur des substrats isolants et conducteurs de différentes rugosités.

Keywords: Microscopie Electrochimique à Balayage, Détection de Protéines, Microfabrication par ablation laser.

ABSTRACT

Scanning electrochemical microscopy (SECM) has developed into an excellent and versatile technique to image heterogeneous chemical reactivities on a surface. Therefore SECM applications cover a wide range of different fields such as biology and forensic sciences. One interesting application that has been found in proteomics, and explored herein, is the use of SECM as a read–out tool for protein microseparations. Proteomic research is a long process where two main steps are contained: separation of one protein from a protein mixture and detection of the separated proteins with a high sensitivity and if required selectivity. Shortening the experimental time of each one of these steps while their quality is kept or improved, should be the strategy to win this exciting race. Although microelectrophoresis affords faster protein separation, the smaller amount of sample employed requires a more sensitive protein detection method. In the first part of the present thesis an approach to solve the latter milestone has been found based on the coupling of miniaturized electrophoresis and SECM. As a result, a complete miniaturized (*i.e.* 1 cm *x* 0.5 cm) isoelectric focusing (IEF) protein separation was scanned by SECM, providing protein detection with a high sensitivity and high resolution. Additionally, protein detection by SECM was performed by different strategies ranging from general to selective approaches based on the tagging of free cysteines and other nucleophiles in proteins and peptides by benzoquinone. The tagged proteins are detected by the mediated reduction of benzoquinone with a redox species produced electrochemically at the SECM tip. After careful optimization, a sensitivity in the low ng mm^{-2} range was reached for bovine serum albumin. One of the major advantages of the present technique is that the selectivity of the protein tagging can be tuned by changing the pH of the reaction media.

Depending on the requirements, cysteine selective or general detection can therefore be achieved with a high sensitivity.

Despite the time reduction achieved with microelectrophoresis and the successful coupling with SECM for sensitive protein detection, conventional SECM setups are limited to scan line by line the whole studied area carrying long experimental times. Additionally, since the response of the sensing microelectrode depends on the probe–substrate distance, discrimination between surface reactivity and topographic artifacts coming from the sample topology is not obvious. The outlined above SECM drawbacks motivate us in the second part of this thesis to address those points. Therefore, some recent developments that show how SECM can be used for reactivity analysis of large, corrugated, tilted and dry surfaces are presented. This extension of SECM is made possible by the use of specialized microelectrode probes fabricated in a soft polymer film integrating for instance, microfluidic systems for delivering microliter volumes of redox–active mediator on a dry sample. These soft structures are then scanned in a contact mode on the substrate, and the originated current from the redox cycling of a mediator is used to construct a reactivity image of the specimen. Due to the use of probes containing individually addressable multiplexed electrodes, it is possible to substantially decrease the recording time while a high quality image resolution is maintained. The electrochemical characterization of the proposed probes was performed by cyclic voltammetry, approach curves and lateral line scans over insulating and conductive substrates of different roughness.

Keywords: Scanning Electrochemical Microscopy, Protein Detection, Microfabrication by laser ablation.

LIST OF ABBREVIATIONS

Abbreviation	Meaning
1D	One dimensional
2D	Two dimensional
3D	Three dimensional
AC	Alternating current
AFM	Atomic force microscopy
BEM	Boundary element method
BQ	Benzoquinone
BSA	Bovine serum albumin
CE	Counter electrode
CE	Capillary electrophoresis
CV	Cyclic voltammograms
DG–RG	Disc generation–ring generation
EOF	Electroosmotic flow
EPFL	Ecole Polytechnique Federale de Lausanne
ESTM	Electrochemical scanning tunneling microscopy
$FcCH_2OH$	Ferrocene methanol
FEM	Finite element method
FIB	Focused ion beam
HPLC	High performance liquid chromatography
IDL	Interface description language

IEF	Isoelectric focusing
IPG	Immobilized pH gradient
KFPM	Kelvin probe force microscopy
L	Lactoferrin
LC	Liquid chromatography
M	Myoglobin
MFP	Multipurpose microfluidic probe
MIRA	Microscopic image rapid analysis
MS	Mass spectrometry
MYO	Myoglobin
PAGE	Polyacrylamide gel electrophoresis
PDE	Partial differential equation
PE	Polyethylene
PET	Polyethylene terephthalate
PI	Piezo electric
p*I*	Isoelectric points
PVDF	Polyvinyldifluoride
QRE	Quasi–reference electrode
R	Protein containing free thiol groups
RE	Reference electrode
SARS	Severe acute respiratory syndrome
SDS	Sodium dodecyl sulfate
SECM	Scanning electrochemical microscopy

SNOM	Scanning near–field optical microscopy
SPM	Scanning probe microscopy
STM	Scanning tunneling microscopy
SWNT	Single–walled carbon nanotubes
TRIS	Trys(hidroxymethyl) amino methane
UME	Ultramicroelectrodes
UV	Ultraviolet
WE1	Working electrode (probe)
WE2	Working electrode (substrate)
WE32	32 individually addressable working electrodes unit
β–L	β–lactoglobulin
μCP	Microcontact printing

LIST OF SYMBOLS

Symbol	Meaning	Units
c	Concentration	mol m^{-3}
c_0	Maximum concentration	mol m^{-3}
c_{bulk}	Bulk concentration	mol m^{-3}
C_d	Double layer capacitance of the electrode	C
C_d^0	Specific interfacial capacitance	C
c_i	Concentration of species i	mol m^{-3}
c_O	Local concentration	mol m^{-3}
D	Diffusion coefficient	m^2 s^{-1}
d	Probe–substrate distance	µm
D_i	Diffusion coefficient of species i	cm^2 s^{-1}
E	Electric field strength	V cm^{-1}
E_g	Energy gap between the ground and the first excited level	eV
E_S	Substrate potential	V
E_T	Probe potential	V
F	Faraday constant (charge on one mole of electrons)	C
g	Factor that represents the influence of the RG on the $i_{T,\infty}$	none
h	Planck constant	J s
h_A	Distance from the sample surface to the probe attachment point	µm
h_P	Real probe–substrate distance for plastic microelectrodes	µm

i	Current	nA
i_c	Capacitive current	nA
I_T	Normalized current ($i_T/i_{T,\infty}$)	none
i_T	Steady–state diffusion current recorded at each point	nA
$i_T^{'}$	Corrected steady–state diffusion current	nA
$i_{T,\infty}$	Steady–state diffusion current recorded at the solution bulk	nA
$\boldsymbol{i}_{T,offset}$	Correction values vector for the current offset	nA
$i_{T,offset,i}$	Current offset between microelectrodes of the array	nA
I_T^{cond}	Normalized current obtained for a conductive substrate	none
I_T^{ins}	Normalized current obtained for an insulating substrate	none
k	Heterogeneous kinetic constant	m s^{-1}
L	Normalized distance (d/r_T)	none
l	Carbon track length	µm
l_T	Length of the probe in the unbent state	µm
l_{th}	Thermal penetration depth	nm
l_α	Optical penetration depth	nm
N_i^*	Normalized number densities of states i	none
n	Number of transfer electrons	none
O	Oxidized form of a redox couple	none
p	Variation of the electric mobility as a function of the distance x	cm V^{-1} s^{-1}
R	Resolution between two ampholytes	cm^{-2}
R	Resistance of the carbon track	Ω
R	Reduced form of a redox couple	none

RG	The ratio between r_{glass} and r_T	none
r_{glass}	Insulating glass sheath radius	µm
R_s	Specific resistance of carbon track	Ω
r	Radial distance measured from the center of the disk	nm
r_T	Tip radius	µm
R_u	Uncompensated resistance of the solution	Ω
$\mathbf{s}$	Correction values vector for the dimensionless scale factor	none
s_i	Dimensionless scale factor	none
t	Time	s
t_L	Polymeric film thickness	µm
u	Electric mobility	$m^2\ V^{-1}\ s^{-1}$
v	Frequency of light	s^{-1}
v_{probe}	Reaction rate at the electrode	$mol\ s^{-1}\ m^{-2}$
v_{sub}	Reaction rate at the substrate	$mol\ s^{-1}\ m^{-2}$
v_T	Translation rate	$\mu m\ s^{-1}$
w	Carbon track width	µm
$\boldsymbol{x}_{offs}$	Correction values vector for the offset in x	µm
$x_{offs,i}$	Offset of the particular electrode that acquired the data point i	µm
x_R	Horizontal registration shift	µm
z	Distance normal to the disk of the surface	nm
α	Probe bending angle	degrees
β	Slope angle	degrees
ϕ	Laser fluence	$mJ\ cm^{-2}$

ϕ_{th}	Fluence threshold of a material	mJ cm^{-2}
δ	Diffusion layer	µm
Δh	Ablation rate	µm $pulse^{-1}$
Δi_T	Current difference between an active and non active substrate	nA
Δl	Sample tilt along the scanning distance	µm
Δx	Required distance to resolve an active from a non active area	µm
κ	Conductivity of the solution	Ω^{-1} cm^{-1}
Λ	Apparent kinetic constant	none
τ_A	Time required for initiating a (photo)chemical process	none
τ_T	Thermal relaxation time	s
σ	Deviation of gaussian distributions	cm^2

TABLE OF CONTENTS

RESUME ..... **IV**

ABSTRACT ..... **VII**

LIST OF ABBREVIATIONS ..... **IX**

LIST OF SYMBOLS ..... **XII**

TABLE OF CONTENTS ..... **XVI**

1. GENERAL INTRODUCTION **1**

2. OVERVIEW ON SCANNING ELECTROCHEMICAL MICROSCOPY AND MICROMACHINING BY LASER ABLATION **4**

2.1. MICROELECTRODES **6**

2.2. INSTRUMENTAL ASPECTS OF SECM **11**

2.3. SECM FEEDBACK OPERATION MODE **13**

2.4. MICROMACHINING BY LASER ABLATION. **24**

3. MINIATURIZED ISOELECTRIC FOCUSING SEPARATION IMAGED BY SCANNING ELECTROCHEMICAL MICROSCOPY **31**

3.1. INTRODUCTION **31**

3.2. EXPERIMENTAL SECTION **36**

3.2.1. Chemicals *36*

3.2.2. IEF Electrophoresis *37*

3.2.3. SECM measurements *39*

3.3. RESULTS AND DISCUSSION **39**

3.4. CONCLUSIONS **43**

4. ADSORBED PROTEIN DETECTION BY SCANNING ELECTROCHEMICAL MICROSCOPY **45**

4.1. INTRODUCTION **45**

4.2. EXPERIMENTAL SECTION **47**

4.2.1. Chemicals *47*

4.2.2. Protein tagging and silver staining on PVDF membranes *48*

4.2.3. SECM measurements *48*

4.3. RESULTS AND DISCUSSION **49**

4.3.1. Protein tagging reaction and SECM detection principle *49*

4.3.2. Optimization of the tagging reaction *52*

4.3.3. Sensitivity and selectivity *54*

4.3.4. SECM imaging of human fingerprint *57*

4.3.5. Indirect protein detection technique *59*

4.4. CONCLUSIONS **63**

5. SOFT STYLUS PROBES FOR SCANNING ELECTROCHEMICAL MICROSCOPY **65**

5.1. INTRODUCTION **65**

5.2. EXPERIMENTAL SECTION **68**

5.2.1. Chemicals *68*

5.2.2. Soft stylus probe fabrication *68*

5.2.3. Preparation of gold films *69*

5.2.4. Preparation of carbon band electrode patterns *70*

5.2.5. SECM measurements and simulation 70
5.3. RESULTS AND DISCUSSION 71
5.3.1. Voltammetric characterisation 72
5.3.2. Approach curve characterisation 74
5.3.3. Contact mode scanning over flat surfaces 78
5.3.4. Contact mode scanning over 3D patterns 81
5.4. CONCLUSIONS 84
6. FOUNTAIN PEN FOR SCANNING ELECTROCHEMICAL MICROSCOPY 85
6.1. INTRODUCTION 85
6.2. EXPERIMENTAL SECTION 88
6.2.1. Chemicals 88
6.2.2. Preparation of a gold micro EPFL logo on glass 88
6.2.3. SECM measurements 89
6.2.4. Fountain pen probe preparation 90
6.3. RESULTS AND DISCUSSION 91
6.4. CONCLUSIONS 99
7. SOFT MICROELECTRODE LINEAR ARRAY FOR SCANNING ELECTROCHEMICAL MICROSCOPY 101
7.1. INTRODUCTION 101
7.2. EXPERIMENTAL SECTION 104
7.2.1. Chemicals 104
7.2.2. Preparation of gold electrodes 104
7.2.3. Finger printing on PVDF membranes 105
7.2.4. Soft microelectrodes array preparation 105
7.2.5. SECM measurements 106
7.2.6. Simulations 107
7.3. RESULTS AND DISCUSSION 108
7.3.1. Probe characterisation 108
7.3.2. Simulation of approach curves 112
7.3.3. Approach curves characterization 116
7.3.4. High throughput SECM imaging 118
7.4. CONCLUSIONS 124
8. PERSPECTIVES AND ON GOING WORK 126
9. BIBLIOGRAPHY 131
APPENDIX 1. CORROSION STABILITY STUDY OF A BALL ALLOY IN DIFFERENT COMMERCIAL INKS BY SECM. 140
CURRICULUM VITAE **..... 145**

1. GENERAL INTRODUCTION

The publication of the human genome few years ago has presented an outstanding impact on several sciences like biology, biochemistry, chemistry and medicine.[1] Nowadays genomic studies can by the examination of a newborn predict how the adult will be like, identify possible pathogens and guide therapies for sickness such as severe acute respiratory syndrome (SARS),[2] breast cancer[3] or improve the understanding of the role of specific genes in the causation of common conditions, such as obesity.[4]

However questions like what makes different humans from others organisms remain still open, since the number of genes found in humans (30000 to 40000) does not differ drastically from the number of genes in organisms such as bacteria, flies or yeast.[5] Taking into account that proteins play a relevant role in all the biological process (metabolism, cell signaling and structural functions), the principal candidate to fulfill the explanations missed by the genome is the proteome. The proteome is not only the study of the proteins that can be expressed by the genome, but also when and where they are expressed, how are involved in metabolic pathways and what type of interactions exists with one another.[6]

From the analytical chemistry point of view, the transition from the genome era to the proteome era has introduced new challenges due to an increment in the complexity of the sample (time dependant and wide concentration range) and the number of analytes. Thus, more stringent separation and detection techniques are required for the analysis of protein mixtures. Separation techniques like capillary electrophoresis (CE), high performance liquid chromatography (HPLC) and two dimensional polyacrylamide gel electrophoresis (2D–PAGE) have been coupled with mass spectrometry and bioinformatics tools for the isolation and identification of proteins.[7] 2D–PAGE has shown to be the most powerful tool for protein separation, due to the combination of two orthogonal separation techniques based on different parameters such as molecular mass and surface charge. In spite of the fact that 2D–PAGE is able to separate up to thousands of proteins or peptides, it is time consuming and requires high expertise.[8] Since the size reduction of the device could significantly decrease the analysis time without dramatically affecting the resolution, miniaturized separation systems could provide a practical solution to this problem.[8-11] However, it requires the use of more sensitive protein detection techniques since the protein loading capacity and thus the amount of loaded proteins has to be reduced to avoid a sample overloading and loss of resolution. As an alternative to fluorescence or radioactive detection, it has been shown elsewhere that the sensitivity of metal staining techniques can be enhanced by using scanning electrochemical microscopy (SECM).[12-14] Indeed, after the optimization of several parameters, protein concentrations down to 0.5 ng mm^{-2} were detected by SECM after silver staining.[15] The special features of SECM (high sensitivity, resolution and

versatility) make this technique an interesting alternative to standard methodologies for protein detection after miniaturized gel electrophoresis.

The present thesis aimed at the enhancement of the SECM technique in order to obtain a high throughput tool for surface activity characterization and proteomic analysis when hyphenated with a protein separation technique, such as isoelectric focusing (IEF) electrophoresis. The second chapter of this thesis presents an overview on SECM and micromachining by laser ablation. The third chapter describes the coupling of miniaturized IEF electrophoresis with SECM as a very sensitive protein separation and detection protocol. Chapter fourth deals with the different strategies for SECM protein detection that have been developed during the present work. In chapters five, six and seven the introduction of a new set of microelectrode probes that may extend the scope of SECM is presented. Finally, the perspectives of the present work are described in chapter eigth. Each chapter has been written in an independent manner for clarity purposes. Despite some experimental sections are redundant, only one list of bibliography has been employed for the whole manuscript.

During my PhD I was involved in different collaborations related to the SECM imaging of photographs, detection of hydrogen peroxide produced at the liquid/liquid interface using SECM and the voltammetric determination of extreme standard Gibss ion transfer energy. However, these collaborations are not included in the present thesis since I am not the author who made the main contribution to these works.

2. OVERVIEW ON SCANNING ELECTROCHEMICAL MICROSCOPY AND MICROMACHINING BY LASER ABLATION

The local characterization of physical surface properties (*e.g.* topography, morphology and reactivity) is one of the most important challenges that scientist from different fields have faced in the last decades. An answer to this problematic has been found with scanning probe microscope (SPM) techniques that take advantage of the interaction between a scanning microscopic probe and the sample, to map localized surface information. Normally, the property that is measured during SPM experiments depends on the intrinsic characteristics of the probe and the substrate, and its separation distance. As a consequence, by recording the probe response while scanning line by line over a substrate, a 3D–image that correlates surface characteristics (*e.g.* chemical activity) with spatial coordinates (*e.g.* in a *x,y*–plane) is obtained. The term SPM was coined in 1981 when the scanning tunneling microscopy (STM)[16] was developed as the first SPM technique that open the door for many other techniques such as atomic force microscopy (AFM),[17] electrochemical scanning tunneling microscopy (ESTM),[18] Kelvin probe force microscopy (KFPM),[19] scanning near–field optical microscopy (SNOM),[20] and scanning

electrochemical microscopy (SECM).[21-24] In general terms, SPM techniques provide the possibility of studying samples at atmospheric conditions (*i.e.* pressure and temperature) with a resolution mainly determined by the probe size. Therefore, striking atomic resolution can be achieved, when using atomic probes.[17] In addition, SPM allows precise nano– or micro–structuring of surfaces by physical or chemical meanings. In contrast, SPM techniques present a signal, which depends drastically on the probe–substrate distance and an excessive long time for acquiring an image of a large sample. As a consequence, SPM techniques are typically limited to the study of areas smaller than few hundreds of micrometers.

SECM is an outstanding SPM technique that not only holds all the SPM advantages, but can also overcome the disadvantages outlined before (*vide infra*). The first SECM experiments was first presented in 1986 by Engstrom *et al.*[22] where a microelectrode was employed for amperometrically measuring the species produced at a biased electrode–substrate. In an independent and contemporary work Bard *et al.*[23] reported in an ESTM–like configuration, the spatial characterization of a Pt–coated integrated circuit pattern with a lateral resolution of 30 nm. However, only until 1989, the principles[24] and theory[25] of SECM were reported attracting the attention of scientists from different fields seeking for a better understanding of the chemical and physical structure–activity relationship on surfaces.[26] During the last two decades, SECM has evolved as a valuable tool for the spatial characterization of surface reactivity and mass fluxes at solid–liquid, liquid–liquid and liquid–gas interfaces.[22, 23, 27, 28] The applications extend from imaging patterned sensor surfaces,[29-31] measuring substance uptake and release from biological cells,[32, 33]

investigating very fast electrochemical reactions,[34, 35] studying local corrosion,[36, 37] screening electrocatalysts,[38] forensic sciences[39] and modifying surfaces.[40]

The most often used probes are amperometric microelectrodes produced by sealing a Pt wire of 10 μm and 25 μm diameters in a glass capillary and exposing the cross–section by grinding and polishing. The microelectrode is attached to a positioning system that provides translation of the probe in horizontal (x, y) and vertical (z) direction. During scanning, a steady–state faradaic current is measured with the help of a (bi)potentiostat. The faradaic reaction results from the electrolysis of diffusing redox–active species undergoing electrochemical reactions at both the microelectrode and the local reaction sites on the specimen surface. The measured currents reflect the interplay between mass transport by diffusion and heterogeneous reactions at the sample. For many situations they can be calculated by continuum simulation.[25, 41-47] Comparison of experimental data with such simulation allows extracting quantitative kinetic information.

The present thesis is based on the use of SECM, thus a more detailed description on some aspects about microelectrodes, instrumental aspects of SECM, SECM feedback operation mode and laser ablation as a microfabrication tool will be given.

2.1. Microelectrodes

Microelectrodes or ultramicroelectrodes (UMEs) are commonly disk electrodes fabricated by encapsulating a microwire such as a platinum wire or a carbon fiber either in a glass pipette or in a resin such as epoxy.[48] Additionally, chemical vapour deposition has been employed for coating metal wires with a thin film of silica.[49] Photolithography techniques have been applied as well to prepare microelectrodes for combined AFM–SECM applications[50] and in a chip–like overall shape.[51] The latter procedures are

cumbersome, provide fragile tips (*e.g.* easily destroyed by probe–substrate crashes) and in some cases are one–experiment probes since mechanical polishing is not possible. Microfabrication of new SECM probes is one of the most important outcomes from the present work and a more detailed revision on this topic will be given in the following chapters. Despite disk electrodes are the most widely used microelectrodes, different electrode shapes such sphere,[52] hemisphere,[53] band,[54] ring[55, 56] and quarter–moon[57] have been employed as well.

Microelectrodes are defined as electrodes with at least one dimension, so–called critical or characteristic dimension, smaller than the thickness of the diffusion layer (δ) in the time of the experiment.[58, 59] δ is defined as two times the square root of the experimental time (t) and the diffusion coefficient (D) of a redox couple ($\delta = 2(Dt)^{1/2}$). For instance, if an electrode is placed at the bulk of a solution containing electroactive species *"R"* and with a biased potential (E_T) sufficient to oxidize *R* (see eq. 2.1), a flux of current will be recorded as a consequence of the electron transfer between the electrode and the neighboring species *R*.

$$\boldsymbol{R} \longrightarrow \boldsymbol{O} + \boldsymbol{ne^-} \tag{2.1}$$

Furthermore, the depletion of *R* at the vicinity of the electrode will produce the diffusion of more *R* species from the bulk of the solution to the electrode surface. If the potential is biased to more extreme values the concentration of *R* at the tip surface becomes null and the global electrochemical process starts to be controlled by mass transport. When such situation is established at a microelectrode, an electrode edge effect appears making the diffusion layer grow rapidly parallel to the electrode but compressing

it perpendicular to the electrode (*i.e.* hemispherical diffusion).[48, 58, 59] As a consequence, a much faster mass transport than electrodes with planar diffusion is achieved, since more redox–active species reach the electrode surface by unit of time. The mass transport at microdisk electrodes is defined by the second law of Fick, which in cylindrical coordinates read:

$$\frac{\partial c}{\partial t} = D\left(\frac{\partial^2 c}{\partial z^2} + \frac{\partial^2 c}{\partial r^2} + \frac{1}{r}\frac{\partial c}{\partial r}\right) \tag{2.1}$$

Where D is the diffusion coefficient of the redox–active species, z represents the distance normal to the disk surface and r is the radial distance measured from the center of the disk. Steady–state is attained in a short period of time with microelectrodes, since diffusion layer stops growing as a result of the fast dynamic equilibrium attained between the species diffusing from the bulk of the solution to the electrode surface and vice versa.[59] Indeed, the time that takes to reach such steady–state depends drastically on the critical dimension of the electrode, for disk microelectrodes this time is approximately r_T^2/D, where r_T is the radius of the tip.[59] The latter situation makes equation 2.2 equal to zero,

$$0 = D\left(\frac{\partial^2 c}{\partial z^2} + \frac{\partial^2 c}{\partial r^2} + \frac{1}{r}\frac{\partial c}{\partial r}\right) \tag{2.3}$$

By expressing equation 2.3 in spherical coordinates, an approximated analytical solution could be found providing that the steady–state diffusion current ($i_{T,\infty}$) recorded at such disk microelectrode is:[60, 61]

$$i_{T,\infty} = gnFDc^{*}r_{T} \tag{2.4}$$

where n is the number of transfer electrons, F the Faraday constant and D the diffusion coefficient of the redox–active species. g is a factor that represents the influence of the insulating geometry on the $i_{T,\infty}$ recorded at inlaid disk microelectrodes. It was first shown by Shoup and Szabo[62] that microelectrodes with insulating sheath thickness similar to the microelectrode radius would present a positive deviation from the theoretical value (*i.e.* infinite insulating plane, g = 4). The latter deviation is produced by the diffusion of species coming from behind the electrode plane.[62, 63] In SECM, the ratio between the radius of the insulating sheath (r_{glass}) to the radius of the active electrode area (r_T) has been defined as *RG* and it is an important parameter employed for characterizing the microelectrodes (*vide infra*) (see Figure 2.1). The insulating sheath thickness is defined by the polishing process, which is normally performed manually. As a result, electrodes that are not centered perfectly are often obtained and the *RG* has to be expressed as an interval (see Figure 2.1). When setting up a SECM experiment the *RG*, the smoothness and flatness of the microelectrode have to be verified as a first step for characterizing the physical properties of the probe.

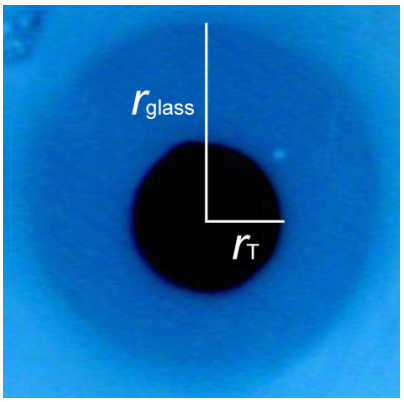

Figure 2.1. Optical inverted picture of a Pt microelectrode showing the radius of the insulating sheath r_{glass} and the radius of the active electrode area r_T (r_T = 12.2 µm, *RG* = 2.4 – 3.2).

Microelectrodes hold more interesting properties such as low capacitive current (i_c) and low ohmic drop ($i \cdot R_u$) that positioned microelectrodes as powerful tools for several electroanalytical applications.[35, 48, 64-66] By taking R_u and C_d as the uncompensated resistance of the solution and the double layer capacitance of the electrode, respectively, the latter could be explained on one hand since i_c decays exponentially with the inverse of $R_u C_d$, which is equal to $r_T C_d^0 \kappa^{-1}$, where C_d^0 is the specific interfacial capacitance and κ is the conductivity.[67] On the other hand, currents in the order of the nanoamps are recorded with microelectrodes producing small $i \cdot R_u$ values. The electrochemical properties of microelectrodes (*e.g.* steady–state current and low capacitive current) can be verified experimentally by cyclic voltammetry in presence of a redox mediator as shown in Figure 2.2. The steady–state is depicted in Figure 2.2 by the flat region in which the current is constant, no matter if the potential is further increased. This result provides the potential value (E_T) that should be used for SECM experiments in order to attain steady–state conditions. Additionally, a small current difference between forward and backward scans indicates a low capacitive current. Normally, cyclic voltammetries are taken at low scan rates (*e.g.* 20 mV s^{-1}) in order to give more time to the system to reach the steady–state. However, thanks to the low ohmic drop and low capacitive currents, scan rates up to 1000 V s^{-1} can be afforded with microelectrodes and experiments can be performed even in low conductivity systems.[59]

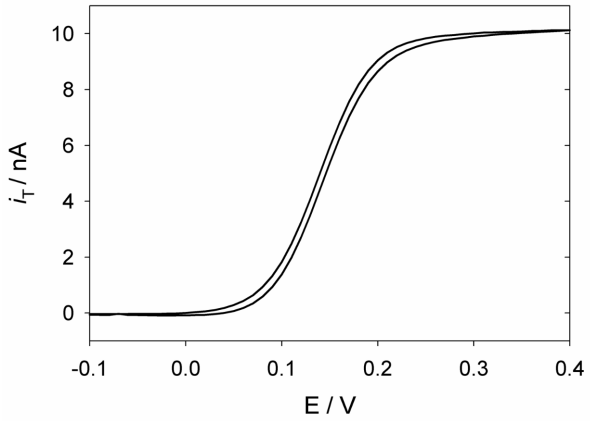

Figure 2.2. Cyclic voltammetry at a Pt microelectrode (r_T = 12.5 μm, RG = 9.6 – 10.4) in ferrocene methanol ($FcCH_2OH$) 2 mM with KNO_3 0.1 M. Scan rate 10 mV s^{-1}. Counter electrode Pt, quasi–reference electrode Ag.

SECM takes advantage of the special properties of microelectrodes to extract localized surface reactivity information from the steady–state current changes, which are a consequence of the interaction between the probe and the substrate upon scanning.

2.2. Instrumental aspects of SECM

Instrumentally, SECM is composed by three main parts. First, a bipotentiostat that controls a three (*i.e.* working probe (WE1), reference (RE) and counter electrode (CE)) or four electrodes (*i.e.* working probe (WE1), working substrate (WE2), reference (RE) and counter electrode (CE)) cell and simultaneously measures the faradaic current produced at the substrate and/or the probe (see Figure 2.3). Secondly, a fine positioning system that allow the probe displacement in horizontal (*x,y*) or vertical (*z*) directions with a high resolution (in the nm range). Finally, a computer that controls the positioning system, as well as, the proper storage and treatment of experimental data. In the present thesis, all the experiments were performed with an IVIUM compactstat (IVIUM Technologies, The Netherlands) operating in a three–electrode or four–electrode mode. The compactstat is a portable instrument (< 600 gram) that can be operated via USB port from a personal

computer without additional power supply. Currents from 1 pA to 10 mA can be detected and up to 32 individually addressable working electrodes (WE32) can be followed simultaneous by using a WE32 unit (IVIUM Technologies, The Netherlands). Additionally a Märzhäuser (Märzhäuser Wetzlar GmbH & Co KG, Wetzlar, Germany) positioning system combined with a piezoelectric system (PI, GmbH & Co KG, Karlsruhe, Germany) were employed for controlling the probe position. The PI system is a piezo actuator with a travel range of 500 μm and a resolution lower than 1 nm mounted on the Märzhäuser *z* axis for performing more precisely movements in this direction. In spite of the high resolution of the PI positioning system, the length that can be scanned is limited. In contrast, the Märzhäuser positioning system presents a travel range equal to 10 cm in *x* and *y* directions and 5 cm in *z* direction with a resolution of 15 nm. The latter device comprises a 2–phases hybrid stepper motor that takes advantage of the variable reluctance and permanent magnet motors (*i.e.* multi–toothed stator poles and toothed permanent magnet rotor, respectively). In most of the experiments performed in this thesis, the Märzhäuser system was employed for the positioning and scanning of the probe. In order to decrease sample tilt, a tilt table was employed allowing the sample leveling with a micrometrical precision. This table was employed all the times when soft stylus probes were not used as working electrodes (*vide infra*), since topographic artifacts are commonly present when the sample tilt produces a considerable probe–substrate distance change during scanning. All the system was isolated from external electric fields with a grounded Faraday cage that remained closed during all the experiments. In addition, by placing the setup over a vibration–isolation table used for laser purposes mechanical stabilities such as vibrations were reduced.

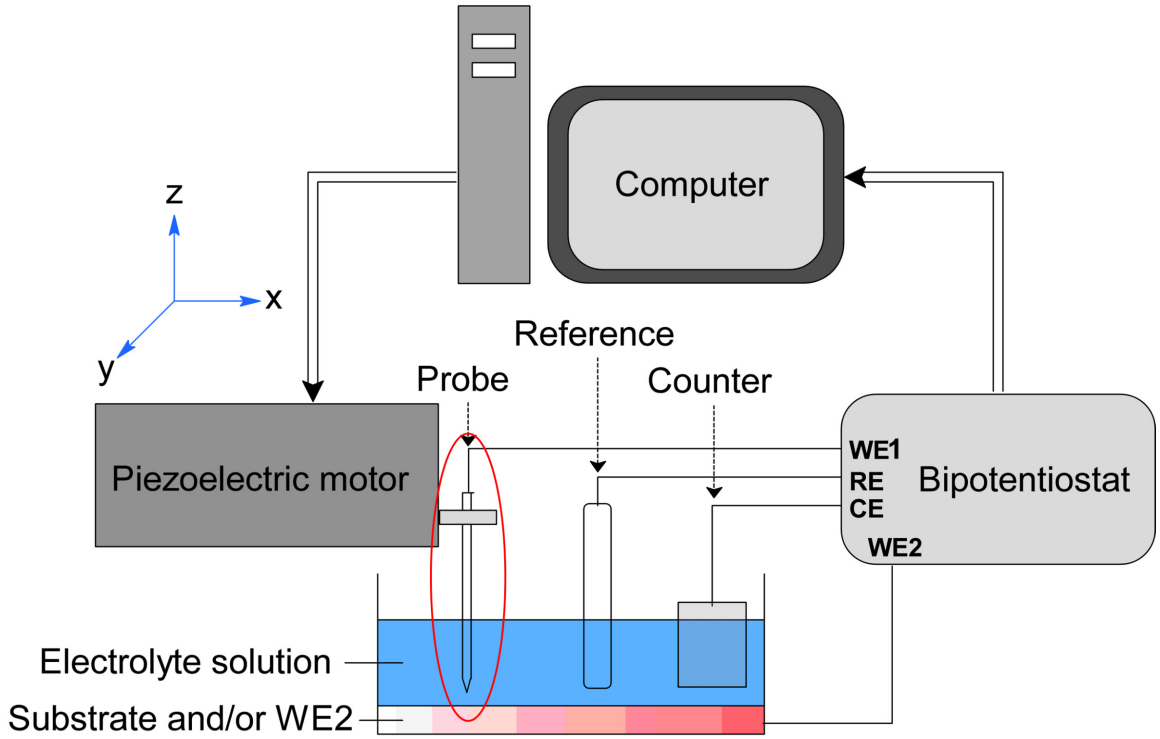

Figure 2.3. Schematic representation of a basic SECM setup.

The SECM setup employed in the present thesis is controlled automatically by the SECMx software,[68] which has been developed in the group of Professor Wittstock at the Carl von Ossietzky University of Oldenburg. For treating the collected data during experiments, the software microscopic image rapid analysis (MIRA), also developed at Oldenburg University, was employed.[69]

2.3. SECM feedback operation mode

Several SECM operation modes have been developed, however the most widely used for chemical imaging of surfaces is the so–called *feedback mode*.[25, 70, 71] The principle of the feedback operation mode is based on the special properties of microelectrodes and the different behavior that the steady–state current could follow when the electrode is brought into the vicinities of a substrate.

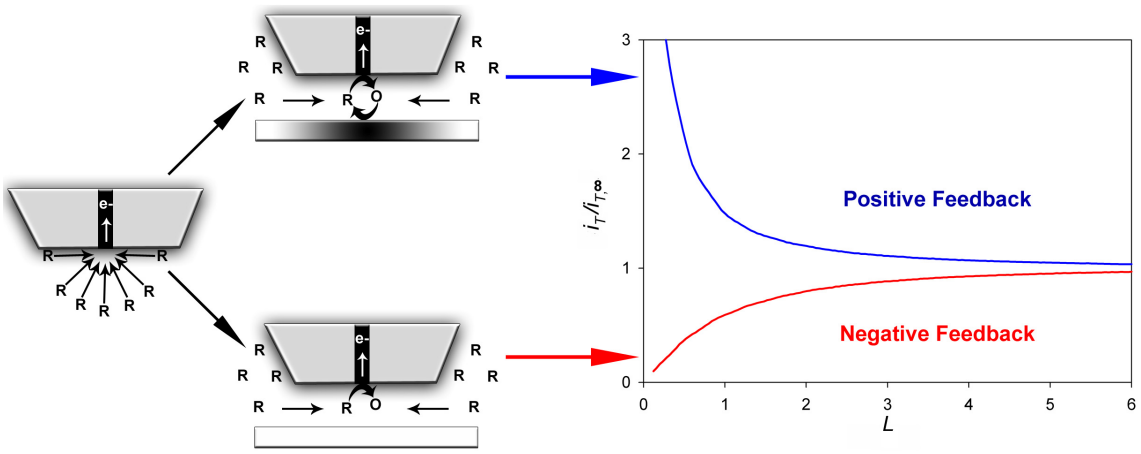

Figure 2.4. Schematic representation of the feedback operation mode and probe approach curves obtained in positive and negative feedback. L is normalized distance defined as the ratio between the probe–substrate distance d and the radius of the electrode r_T. The normalized current (I_T) is defined by current value measured at each point (i_T) divided by the steady–state current recorded at the solution bulk ($i_{T,\infty}$).

In the feedback mode, the tip is placed at the bulk of the solution with a biased potential to electrolyse a redox mediator under diffusion–limited conditions. When the tip is moved slowly from the bulk of the solution toward a substrate with continuous monitoring of the steady–state current at the microelectrode, two different behaviors can be obtained depending on the reactivity of the substrate. If the surface under study is able to reverse the process occurring at the tip by (electro)chemical mean or if it is a conductive substrate (*vide infra*), a current increase will be observed as the electrode is brought at the boundaries of the substrate. This behavior is called *positive feedback* and it is produced by the increased speed of redox mediator recycling as the probe gets closer to the substrate (blue curve in Figure 2.4). In contrast, when the substrate presents no (electro)chemical activity and if it is an insulator, the current decreases as the tip gets closer to the substrate. This behavior is called *negative feedback* and it is a consequence of the hindering of the redox mediator diffusion between the substrate and the microelectrode (red curve in Figure 2.4).

The above two behaviors can be clearly identified by plotting the tip current as a function of tip displacement, or what is commonly called *approach curve* (see Figure 2.4, right part). Approach curves are another tool for characterizing the quality of microelectrodes, since $i_T - d$ curves are drastically affected by specific probe properties, such as microelectrode size, probe flatness and position of the active electrode area inside the insulating sheath (*i.e.* protrude, inlaid or recessed). In addition, it makes difficult the comparison of extracted data with two different probes. However, by normalizing both current and distance coordinates, such comparison could be done. Usually, the current value measured at each point (i_T) is normalized by the steady–state current recorded at the solution bulk ($i_{T,\infty}$), while the probe substrate distance (d) is normalized by the radius of the active electrode area (r_T). I_T and L commonly denotes the normalized current and probe–substrate distance, respectively (see Figure 2.4, right part).

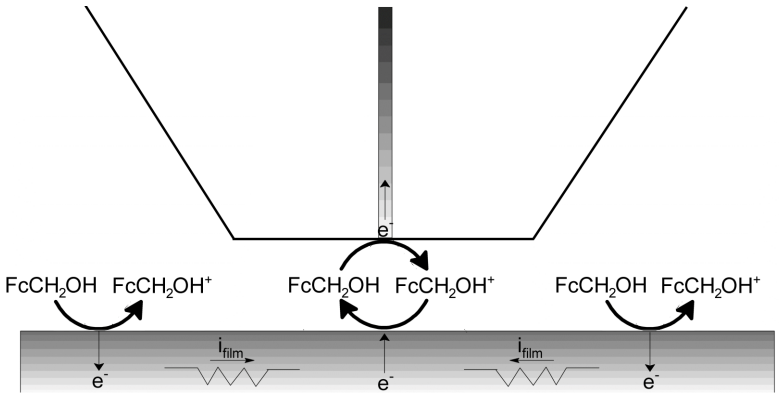

Figure 2.5. Schematic diagram showing the recycling of the redox mediator and the charge transfer processes across an unbiased conductive substrate.

It is important to notice that positive feedback can also be encountered when the probe is approached toward an unbiased conductive substrate submerged in a solution of redox–active species, for instance $FcCH_2OH$ (see Figure 2.5). In such situation, the substrate potential (E_S) is given by the concentration ratio between $[FcCH_2OH]/[FcCH_2OH^+]$ at the

vicinities of the solution/substrate interface. Therefore, different potential regions can be observed over the conductive sample as a result of the local perturbation introduced by the microelectrode placed close to the sample surface (see Figure 2.5).[72] The recycling of the redox mediator will depend mainly on the lateral charge transport in the substrate, concentration of the redox mediator, tip–substrate distance, size of the sampled area (*i.e.* the sampled area has to be higher than the active electrode area to have positive feedback) and rate of the electron transfer. Indeed, by controlling these variables, it is possible to quantify the conductivity of thin films by SECM.[73] In addition, when approaching toward a conductive substrate that is completely parallel to the microelectrode plane, tunneling currents could be achieved at very small separation distances (*i.e.* few angstroms) increasing drastically the positive feedback response.

The possible differentiation between active and non–active surfaces by SECM in feedback operation mode, is thanks to the fact that the tip is scanned across the *x,y*–plane at a fixed distance from the substrate. For example, by scanning horizontally (*e.g. x* or *y* direction) over an insulating substrate at a normalized probe–substrate distance equal to 1 (see Figure 2.4, right part), a normalized current around 0.6 should be recorded. If during scanning the probe reaches an active region where the redox mediator recycling takes place under mass–controlled conditions, the current profile will register a current jump of 0.9 current units. As a result, scanning line by line a specimen and displaying the current values measured at all the couple of coordinates (*x,y*), a 3D image is built showing active and non–active regions as zones with high and low current values, respectively. The quality of the SECM image is defined mainly by the current contrast obtained. Constant

height imaging was the name given to this methodology and it is one of the most widely used approaches for SECM imaging.

Some of the most important parameters that play a relevant role on the resolution and sensitivity of SECM imaging in feedback mode are the probe–substrate distance, the electrode size, the *RG* and the rate of reaction at the substrate. In the following text, a short description of the influence of each one of these parameters will be given.

The probe–substrate distance plays a relevant role in SECM imaging since the electrode has to be close enough to the substrate to be able to detect surface activity (*e.g.* $d < 2r_T$). As it can be seen in the right part of Figure 2.4, as the probe gets closer to the substrate, the monitored current contrast between an active and a non–active zone will increase. However, when the probe is closer to the sample the possibilities of probe–substrate crashes are increased. The latter introduce a constraint, since a compromise between current contrast and probe–substrate distance has to be determined. Additionally, topographic artifacts can be introduced during the scanning of rough or tilted samples, which could change the probe–substrate distance and at the same time the probe response. For the reliability of the extracted information with SECM, flat samples that are parallel oriented to the electrode surface are preferred. The latter is one of the highest limitations of SECM that has been trying to be addressed in the present work. Chapter 5 shows a short revision of the different strategies employed for controlling the probe–substrate distance and our approach based on soft plastic microelectrodes for SECM in contact mode (*vide infra*).[57]

The lateral resolution in SECM imaging is drastically influenced by the size of the electrode since the resolution is normally in the same order of magnitude of the electrode

size. Therefore, nanoelectrodes have been prepared and employed for nanometric resolution SECM imaging[74] and for studying fast electrochemical reactions rates.[35] Although, nanoelectrodes are able to resolve nanometrical regions with strong differences in electrochemical reactivity, substrate regions where the kinetics are not especially fast are not resolved. The above is due to the enhanced mass transport at nanoelectrodes that masks the influence of redox–active species coming from the substrate. As a conclusion, higher resolution can be obtained with smaller probes, but with a lower sensitivity for surface reactivity detection. Additionally, when working with nanoelectrodes, special care has to be paid to the preparation, polishing, manipulation and operation of such probes. Many efforts have been dedicated to increase the lateral resolution so as to match that of atomic force microscopy. In chapter 5 and chapter 7, is shown how SECM can also be used as a scanner of chemical reactivity on large, corrugated and tilted substrates in a short time scale with a high resolution.

The influence that the probe *RG* has on SECM imaging in feedback mode is depicted in Figure 2.6. According Figure 2.6, if two probes of different *RG* are employed for scanning at the same probe–substrate distance the surface activity of a sample, the one that presents the bigger *RG* value will develop a higher current contrast. This observation is most likely because the bigger insulating sheath will make a more efficient hindering of the redox mediator diffusion and as a result, when scanning over an insulating region a lower current will be recorded. As it can be seen in Figure 2.6, positive feedback is not drastically affected by the *RG* parameter of the probe, since in this case the blocking of the redox mediator diffusion is not the most important phenomena, but its recycling.

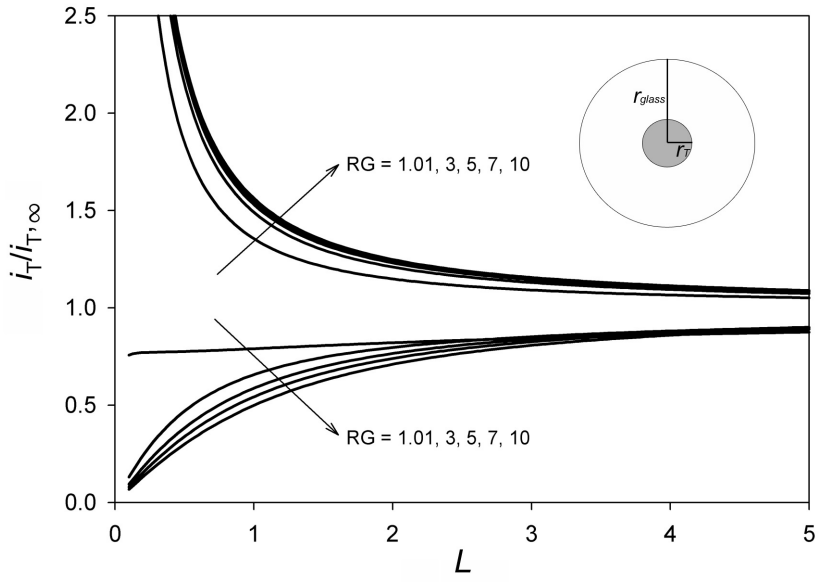

Figure 2.6. Effect of the *RG* parameter on SECM approach curves for positive and negative feedback mode. The approach curves were calculated from equation 2.5.[42]

Despite the fact that the probes with big *RG* values provide the best current contrast, experimentally it is more difficult to parallel the probe and substrate planes, increasing the possibilities of probe–substrate crashes when scanning close to the sample. Using a bigger probe–substrate distance could mitigate the latter drawback; however, this will generate a lower current contrast. It is important to notice that probes with small *RG* could be employed for scanning surfaces at closer probe–substrate distances. In spite of that, a limitation is introduced when using microelectrodes with *RG* lower than 10, since diffusion of species coming from behind the microelectrode plane is not anymore negligible. Indeed, when the radius of the insulting sheath is similar to the active electrode area of the probe, the negative feedback response is completely loose and the imaging resolution is drastically affected (see Figure 2.6). As a conclusion, a compromise has to be found in between the *RG* and the probe–substrate distance allowing a good SECM imaging resolution without probe–substrate crashes.

The kinetics of the reaction that takes place at the substrate is also an important parameter, since it will determine in some extent the magnitude of the response recorded when the probe is close to the active zone. Thus, if the electrochemical reaction rate is slow, the redox mediator recycling will be slow as well and low current contrast will be monitored. Figure 2.7 shows the influence that the reaction rate taken place at the substrate has on the SECM approach curves.

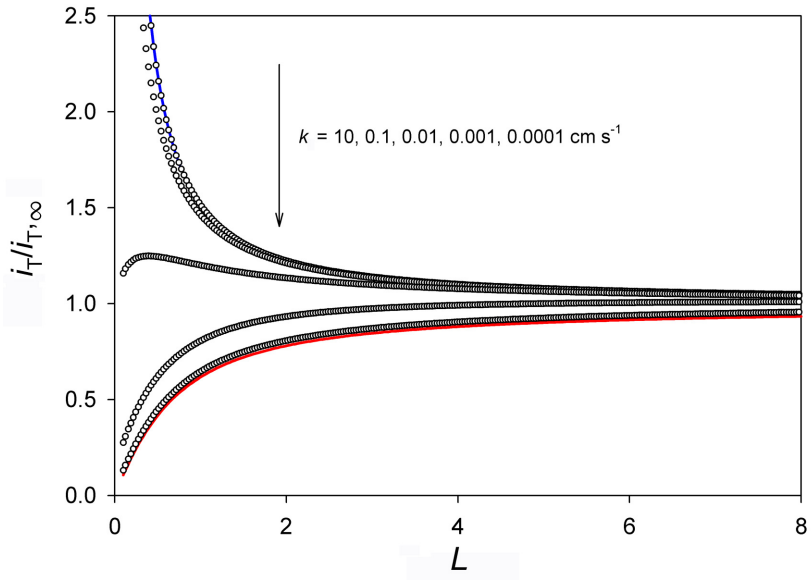

Figure 2.7. Influence of the electrochemical reaction rate that takes place at the substrate on the SECM approach curves. The arrow illustrates the direction in which the value of the heterogeneous kinetic constant (k) is decreasing. The approach curves were calculated from equation 2.5.[42]

Purely positive and negative feedback approach curves calculated from Cornut *et al.*[42] are illustrated by blue and red lines in Figure 2.7, respectively. Depending on the studied reaction rate, the $i_T - d$ curve will be found between these two extreme cases. As faster is the kinetics of the process at the substrate, higher will be the current contrast and vice versa. Similarly to nanoelectrodes, heterogeneous surface activity with slow kinetics will be difficult to resolve from a purely negative feedback behavior; however microelectrodes provide a higher sensitivity.

As it can be seen in Figure 2.7, SECM approach curves provide insights into the kinetics of the sample under study, since the monitored currents reflect the interplay between mass transport by diffusion and heterogeneous reactions at the sample. For many situations, they can be calculated by continuum simulation.[25, 41-47] Comparison of experimental data with such simulation allows extracting quantitative kinetic information. Different analytical approximations have been derived with the aim of correlating parameters such as the heterogeneous kinetic constant (k) with the experimental $i_T - d$ profile avoiding the use of numerical simulations. However, such approaches have been mainly devoted to disc shaped microelectrodes with an RG around 10.[44] For more complex geometries or systems, numerical simulations based on finite element method (FEM) or boundary element method (BEM) are normally required.

Cornut *et al*.[42] reported recently an approximated analytical expression for quantitative SECM measurements, where the RG of the probe is taken into account (see eq. 2.5).

$$I_T(L,\ \Lambda,\ RG) = I_T^{cond}\left(L+\frac{1}{\Lambda},RG\right) + \frac{I_T^{ins}(L,\ RG)-1}{\left(1+2.47RG^{0.31}L\Lambda\right)\left(1+L^{0.006RG+0.113}\Lambda^{-0.0236RG+0.91}\right)} \quad (2.5)$$

Where the recorded normalized current for conductive (I_T^{cond}) and insulating (I_T^{ins}) substrates are equal to

$$I_T^{cond}(L+\frac{1}{\Lambda},\ RG) = \alpha(RG) + \frac{\pi}{4\beta(RG)\mathrm{ArcTan}\left(L+\frac{1}{\Lambda}\right)} + \left(1-\alpha(RG)-\frac{1}{2\beta(RG)}\right)\frac{2}{\pi}\mathrm{ArcTan}\left(L+\frac{1}{\Lambda}\right) \quad (2.6)$$

$$I_T^{ins}(L,\ RG) = \frac{\frac{2.08}{RG^{0.358}}\left(L-\frac{0.145}{RG}\right)+1.585}{\frac{2.08}{RG^{0.358}}(L+0.0023RG)+1.57+\frac{\ln RG}{L}+\frac{2}{\pi RG}\ln\left(1+\frac{\pi RG}{2L}\right)} \quad (2.7)$$

and with

$$\alpha(RG) = \ln 2 + \ln 2\left(1 - \frac{2}{\pi}\mathrm{ArcCos}\left(\frac{1}{RG}\right)\right) - \ln 2\left(1 - \left(\frac{2}{\pi}\mathrm{ArcCos}\left(\frac{1}{RG}\right)\right)^2\right) \quad (2.8)$$

$$\beta(RG) = 1 + 0.639\left(1 - \frac{2}{\pi}\mathrm{ArcCos}\left(\frac{1}{RG}\right)\right) - 0.186\left(1 - \left(\frac{2}{\pi}\mathrm{ArcCos}\left(\frac{1}{RG}\right)\right)^2\right) \quad (2.9)$$

$$\Lambda = \frac{kr_T}{D} \quad (2.10)$$

By knowing precisely $i_{T,\infty}$, L, r_T, D and the RG, k can be extracted from equation 2.5 and 2.10, after fitting the theoretical curve to the experimental data. As a result, probes with RG different to 10 can be employed for kinetic characterization purposes. This new expression is valid for $RG \leq 20$, $L \geq 0.1$ and any Λ value.[42] The Figures 2.6 and 2.7 of the present chapter were calculated by using equation 2.5.

Numerical simulations have shown to be highly useful for a better understanding and interpretation of experimental results obtained with complex geometries.[25, 46, 75-77] Additionally, the current computer facilities have overcome old limitations making possible the routinely use of such tools. Finite element and boundary element methods are numerical methods employed for solving partial differential equations (PDEs) that represent exactly a phenomenon under study (*i.e.* mass transport in a microelectrode) and cannot be solved analytically. The difference between finite element and boundary element methods arises from the approach used for finding an equation that is mathematically equivalent to the original PDE and which numerical resolution provides an approximated solution to the studied problem. In general terms, FEM is based on the numerical resolution of a polynomial representation of the PDE,[78] while BEM consists on the reformulation of the PDE as an integral equation defined in the boundaries and solved

by numerical matrix routines.[77] BEM presents the advantage of being less time and computational resources consuming, since the problem dimensionality is reduced as a consequence of the mathematical treatment.[46, 77] In contrast, FEM has the advantage that commercially packages are already available, which includes several routines concerning electrochemical systems and avoiding the demanding task of programming them (*e.g.* COMSOL Multiphysics).

In chapter 4, the approximated analytical expression reported by Cornut *et al.*[42] was employed for extracting the kinetics of the reduction of adsorbed benzoquinone molecules, while in chapter 5 and chapter 6 BEM and FEM simulations were employed respectively for simulating approach curves performed at quarter–moon shape microelectrodes.

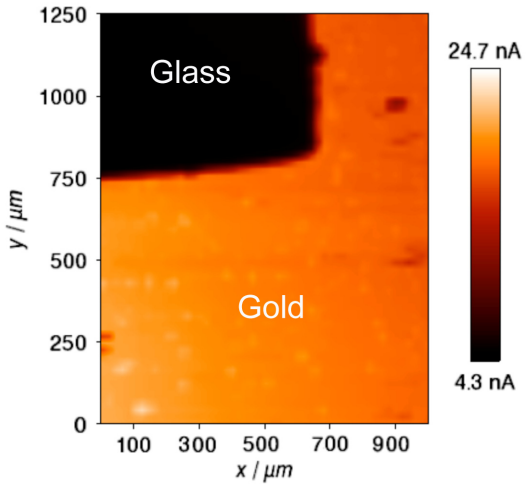

Figure 2.8. Constant height SECM image of a glass partially covered by gold in 2.0 mM $FcCH_2OH$, 0.1 M KNO_3. Working electrode Pt (r_T = 10 µm, RG = 3 – 4), step size = 20 µm and translation rate v_T = 20 µm/s.

Figure 2.8 shows a SECM image obtained in feedback operation mode, where a gold on glass sample was scanned with a Pt microelectrode showing high current values for gold areas and low current values for insulating glass areas. The high resolution that is

achieved with SECM imaging allows to detect clearly not only the morphology of the sample, but also micrometer imperfections on the gold film.

2.4. Micromachining by laser ablation.

Microfabrication techniques based on UV–photoablation of polymeric materials were used in the present work for preparing a new type of microelectrodes for SECM. This procedure was performed with an excimer (*abbr.* of excited dimer) laser, in which an excited state complex is formed by the interaction of two monomers or misnomers. Normally, one of the species that participates in this process is excited, for instance, by applying an electrical discharge. The excited complexes present a short lifetime (*e.g.* nanoseconds), and as a consequence decay to its ground state emitting laser light, along with the complex dissociation.[79] Typically, this light emission is characterized by a longer wavelength of the monomer transition. The laser wavelength can be tuned depending on the complex employed, typically between a noble gas and a halogen species (*e.g.* ArF or KrF).

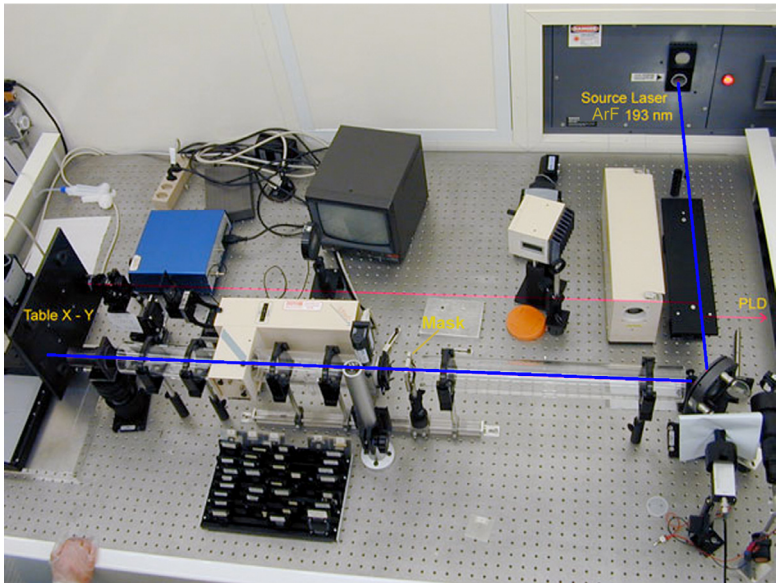

Figure 2.9. Digital photograph of the excimer laser employed in the present thesis.

Excimer lasers take advantage of this phenomenon to machine a substrate by irradiation of laser pulses characterized by a fluence (ϕ, energy given to a substrate with a specific area) and a frequency. As it can be seen in Figure 2.9, the setup devoted to microfabrication purposes consists mainly on a pulsed laser source of ArF (λ = 193 nm), an optical pathway (depicted in blue in Figure 2.9), a metallic mask and a *x,y*–table (perpendicular to the laser beam). In addition to the optical system itself, the optical pathway has a relevant role in the photoablation process, since lose of light intensity takes place by absorption of O_2, for instance.[79] For this reason it is advisable to isolate the optical pathway with an inert gas atmosphere (*e.g.* N_2) or to reduce the optical pathway length. Due to the fact that the area of the produced laser beam is around 1 cm^2, a mask consisting of a metallic sheet (*e.g.* molybdenum) with an overture is needed to project the shape and the size of the ablated area. Typically, the size of the ablated area corresponds approximately to one tenth of the overture in the mask. Structures in the low micrometer range can be fabricated by following this methodology. In the present microfabrication process a molybdenum mask was employed with a rectangular overture of 1 cm length and 200 μm width. Thus, microchannels with an average width around 30 μm are possible to ablate, while the total movement of the translation stage defines the microchannel length. The microstructure depth is determined by the translation rate of the sample, the laser fluence, the pulses frequency and the mask size and shape. Normally, the translation rate of the *x,y*–table was 400 μm s^{-1}, while the laser was applied with a nominal fluence of 250 mJ cm^{-2} and a frequency of 50 Hz. As a result microchannel depths between 20 μm and 30 μm were prepared on polyethylene terephthalate (PET)

films. For two–dimensional designs where perpendicular structures have to be fabricated, continuous or sequential ablation in *x* and *y* direction can be afforded by the *x,y*–table shown in Figure 2.9. However, when fabricating more complex designs, the simpler approach is to create a mask with the wanted pattern that projects the shape of the mask overture over the substrate. Despite it is a fast way of building complicate structures in a static mode, it is limited to structures smaller than the size of the mask. Recently, portable laser ablation machines comprise laser beams with smaller areas, which afford submicrometers structures fabrications in a dynamic mode without using any masks.[79] Before to any ablation process, the position of the sample has to be calibrated in such way that the sample is placed at the image plane, in order to obtain a sharper ablation zone.

The principle of material removal by laser ablation has been explained by two different phenomena, namely thermal ablation and photochemical ablation. There is still controversy in which model could explain completely the photoablation process, but it seems that a combined photophysical mechanism will be the most likely. The difference between the appearance of thermal or photochemical ablation mechanism is mainly given by the magnitude of the absorbed energy and the time scale of the different process that can take place inside the material (see Figure 2.10). In Figure 2.10, E_g stands for the energy gap between the ground and the first excited state. Electronical transitions can be generated between the ground state and the first excited state by the absorption of photons with $h\nu \geq E_g$, or lower energetic transitions ($h\nu < E_g$) by the presence of defects or impurities in the material. Additionally, relaxations processes could take place as electronic and vibrational transitions among the different electronic states. Ablation of the

material could take place by desorption of molecules in the ground state and especially in the excited state (photochemical ablation). In contrast, non-radiative transitions will lead to the local increment of temperature, generating the ejection of melted or vaporized sample (photothermal ablation, see Figure 2.11b). The global process will be driven then by the relationship between the thermal relaxation time (τ_T) and the times (τ_A, τ_A^*) that represent the time for initiating a process such as photochemical desorption or chemical reactions.

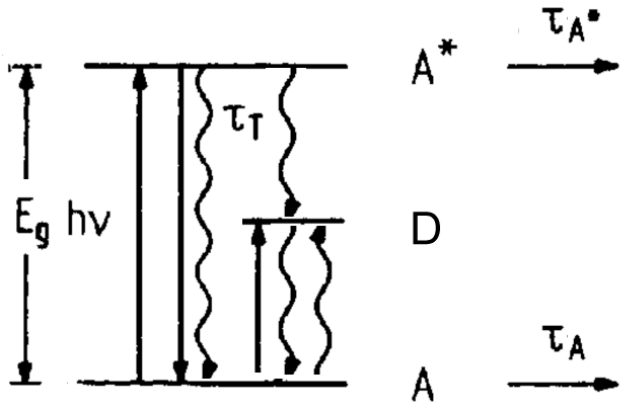

Figure 2.10. Schematic representation of the different types of electronic excitation and relaxation in a material with two states A, A*. Absorption or emission of photons and non-radiative transitions are represented by straight and oscillating lines, respectively. Modified from Bäuerle.[80]

The total ablation rate (Δh) expressed as the ablated depth per pulse (μm pulse^{-1}) can be approximated as:

$$\Delta h \approx v_A N_A^*(0) + v_{A^*} N_{A^*}^*(0) + v_D N_D^*(0) \tag{2.11}$$

Where v_i represents the rate constants for thermally activated desorption and N_i^* are the normalized number densities of states i. Purely thermal effects will be observed then if $\tau_T \ll \tau_A^*$ and $\tau_A \ll \tau_A^*$ (suppressing the second term on the right hand of equation 2.11), while purely photochemical effects will be observed if $\tau_T > \tau_A^*$ and $\tau_A^* \ll \tau_A$

(suppressing the first term on the right hand of equation 2.11). A mixed mechanism is expected for $\tau_T << \tau_A^* << \tau_A$. The defects states generated during the ablation process play an important role since they can contribute as well to desorption of material or to its local heating.

For both, photothermal and photochemical ablation processes, the ablation rate can be defined by the logarithmic law:

$$\Delta h(\phi) = l_\alpha \ln\left(\frac{\phi}{\phi_{th}}\right) \tag{2.12}$$

with l_α as the optical penetration depth and ϕ_{th} the threshold fluence that is the minimum energy required for photoablation of a specific material. From equation 2.12 it can be conclude that materials with low ϕ_{th}, and big l_α are the most affected to laser ablation. Another intrinsic property from the material that influences the ablation process is the thermal penetration depth (l_{th}). Thus materials such PET that presents small values of l_{th} (*i.e.* 90 nm), in comparison with Al for example (l_{th} = 2.80 μm), will more easily concentrate the heat given by the laser and as result be more easily photoablated.[80]

The photoablation process can also introduce mechanical stress, since the absorbed light can induce material defects. In polymeric materials chemical modifications by laser ablation are an important issue, since surface properties such as hydrophobicity are changed during the ablation process. Ablated PET films present a lower hydrophobicity, probably due to the presence of oxygen–contained compounds as a result of the polymer surface oxidation.

When the number of pulses is increased, the ablation rate is normally increased since more energy is given to the ablated area (see Figure 2.11a). Indeed, plasma formation

could take place at the vicinities of the ablated area favoring the ablation process, as absorbed energy of the laser light by the plasma could be additionally transferred to the material, as shown in Figure 2.11b.[80]

However, it might happen that the ablation rate decreases with a higher number of applied pulses. This phenomenon is most likely because energy loss due to heat conduction through the produced deeper cavity and re–condensation processes, re–absorption or scattering of the incident laser light could take place as a result of the longer distance that the material has to cross to get off from the cavity. The above is specially critic with nanosecond pulses (as in the case of excimer lasers, ~ 20 ns) where the removed particles can travel only between 20 μm and 200 μm.[80] For this reason, it is advisable to cleaning strictly the microstructures after ablation to remove all the residues of the ablation process.

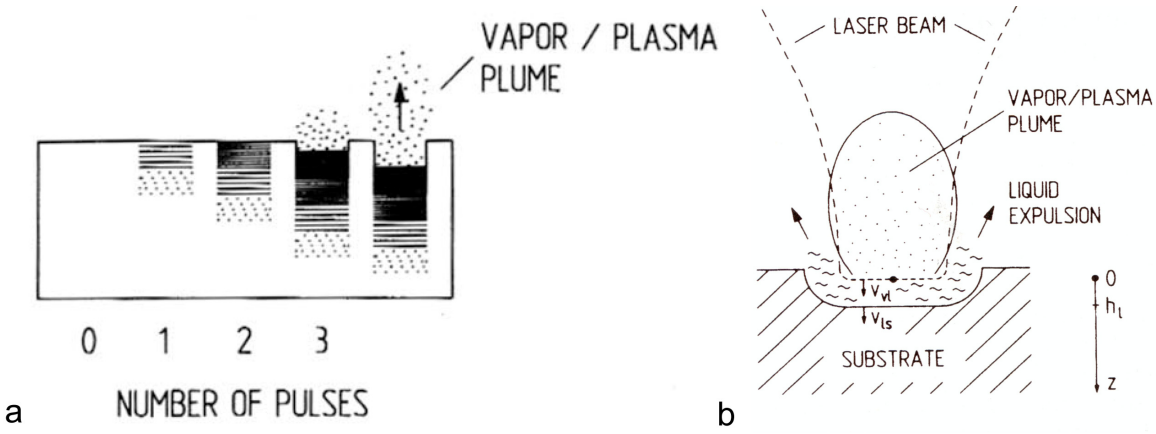

Figure 2.11. a) Schematic showing the increase in absorption with successive laser pulses. b) Laser–induced surface melting, vaporization, and liquid–phase expulsion. Taken from Bäuerle.[80]

Microfabrication by UV–laser ablation is a process that has to be optimized for each specific application and although it is not a technique for batch–level production, allows a fast prototype production of microstructures (*e.g.* microchips) that can be easily tested.

More details concerning the preparation of such plastic microelectrodes are given in chapters 5, 6 and 7.

3. MINIATURIZED ISOELECTRIC FOCUSING SEPARATION IMAGED BY SCANNING ELECTROCHEMICAL MICROSCOPY

3.1. Introduction

Isoelectric focusing (IEF) electrophoresis is a protein separation technique based on the different charge that ampholytes (*i.e.* chemical compounds that can act either as an acid or a base, like aminoacids) develop inside a pH gradient media under the application of an electric field.[8] Thus, ampholytes are concentrated inside the pH region where their net charge is equal to zero (p*I*) and consequently not affected by the electric field. Stable pH gradients are generated by the use of carrier ampholytes (*i.e.* amphoteric species that present both good electrical conducting (carrier) and pH buffering (ampholyte) properties), a concept introduced in 1961 by Svensson.[81] Subsequently, Vesterbeg synthesized the ampholytes described theoretically by Svensson, marking the beginning of the development of the current IEF separations used nowadays.[82]

It has been shown additionally, that in order to obtain a steady–state of isoelectric equilibrium in an IEF experiment some problems linked to convection, local overheating, and electrochemical reactions at the electrodes have to be solved. Porous matrix with low sieving characteristics that reduce convective mixing, carrier ampholytes with similar

conductivities that produce a uniform conductivity through the whole system and strong acids (anolyte) and bases (catholyte) that repels the ampholytes from the electrodes have been implemented.[8] Recently, Cheng–Xi Cao has pointed out more possible causes of instabilities of the pH gradient like electroosmotic flow (EOF), diffusion of ampholyte into or out of the gel, interactions between ampholytes and isoelectric focusing of water.[83] The latter problem has been solved by using immobilized pH gradients (IPG), where carrier ampholytes are bonded to the polyacrylamide gel. Preparative protein separations have been developed based on IPG gels, where flow chambers are placed on top of an IPG strip allowing the concentration of a high amount of proteins with a p*I* close to the pH of the gel localized under the flow chamber.[84]

In an ideal IEF separation in which all of these instabilities are controlled, the focusing of ampholyte bands can be obtained as a result of the equilibrium between the natural diffusion process and the imposed electrophoretic movement. At a focusing equilibrium condition, the one–dimensional flux of an ampholyte inside an electric field can be expressed like:[8]

$$cuE = D\frac{\mathrm{d}c}{\mathrm{d}x} \tag{3.1}$$

where c, u, E and D are the concentration of the ampholyte, its electric mobility, the electric field strength and the diffusion coefficient, respectively. The left side of equation 3.1, represents the ampholyte flux due to migration, while the right side describes the diffusion of the ampholyte. The latter differential equation defines the final steady–state obtained in IEF separations, in which the ampholytes are mostly concentrated in the

corresponding zone to their p*I*. If it is assumed that the variation of the pH and the electric mobility with the distance is constant at the vicinity of its p*I*:

$$p = -\frac{\mathrm{d}u}{\mathrm{d}x} = -\frac{\mathrm{d}u}{\mathrm{dpH}}\frac{\mathrm{dpH}}{\mathrm{d}x} \tag{3.2}$$

where p is a positive value that represents the variation of the electric mobility as a function of the distance x. As at x equal to 0, u will be 0 also, thus p can take the linear form:

$$p = -u/x \tag{3.3}$$

If the equation 3.3 is introduced into the equation 3.1, then one can obtain:

$$-\frac{pE}{D}x\mathrm{d}x = \frac{\mathrm{d}c}{c} \tag{3.4}$$

The integration of the latter equation provides a Gaussian distribution of the ampholyte in the region nearby of the isoelectric point of the ampholyte, in which a maximum concentration c_0 can be reached (see equation 3.5).

$$c = c_0 \exp\left(-\frac{Epx^2}{2D}\right) \tag{3.5}$$

According to equation 3.5, the quality of the isoelectric focusing of an ampholyte will depend on the strength of the electric field, the diffusion coefficient of the species and the parameter p. The deviation (σ) of this Gaussian distribution can be defined by:

$$\sigma = \frac{D}{Ep} \tag{3.6}$$

Therefore, the resolution R between two ampholytes can be defined as:[85]

$$R = \frac{\Delta pI}{\overline{\Delta\sigma}} = \frac{2\Delta pI}{\sigma_1 + \sigma_2} \tag{3.7}$$

Taking into account equations 3.2, 3.6 and 3.7, one can pointed out that the separation resolution in IEF can be improved by the use of a strong electric field and a steep pH gradient. In addition, the separation of ampholytes with small diffusion coefficients and sharp variation of d*u*/dpH at their p*I* can also raise the separation resolution. Proteins with differences of 0.02 pH units in their p*I* have been separated by IEF electrophoresis. Furthermore it is possible to regard that the resolution does not depend on the gel length, as it has been showed experimentally by several authors.[11, 86-88] In spite of this, when the electric field is suspended, for instance after protein separation is finished, protein bands broadening become a serious limitation for miniaturized electrophoresis. The latter could be clearer observed by defining σ in absence of any electrical field as the distance that one molecule could diffuse in a given time (t):

$$\sigma = \sqrt{Dt} \tag{3.8}$$

Taking the diffusion coefficient of the lisozyme protein in agarose gels as 12 x 10^{-11} m^2 s^{-1},[89] one previously focused lisozyme band could diffuse in both directions by a distance equal to 0.11 cm, after 3 hour of finished the separation. For a normal gel size (*i.e.* 10 cm x 10 cm) such band size increment correspond only to 1% of the total size of the gel, but in miniaturized gels (*i.e.* 1 cm x 1 cm), it is the 10 %. As described below, special care has to be paid to resolution lost by protein band broadening after IEF microelectrophoresis or further passive blotting procedure that last for several hours (*vide infra*).

Microelectrophoresis was first developed by Matiola in the mid of 1960s for the analysis of hemoglobin in erythrocytes.[86] Although it was clear that microelectrophoresis offers the obvious advantage of faster operation in addition to much lower sample

demands, it was not before the last 10 years that more attention has been paid to this topic. Yeung *et al.* have demonstrated that several hundreds of proteins can be efficiently separated with miniaturized 2D–PAGE (1 cm x 1 cm) within less than 2 hours.[9-11] Thus, microelectrophoresis can present similar resolution power of normal electrophoresis but in less time. The major drawback of 2D-PAGE is the stability of the polyacrylamide gel that is employed as the matrix for this separation. Due to this fact, separated proteins are usually blotted to a more stable matrix, which additionally is more compatible with detection techniques. Polyvinyl difluoride (PVDF) membrane is a common hydrophobic porous solid-phase support for protein blotting with a high binding capacity and high mechanically and chemically stability. Typically, IEF protein separations are blotted to PVDF membranes by protein diffusion from the gel to the PVDF membrane (*i.e.* passive blotting). Electrophoretic protein transfer is normally not possible, since the plastic support that holds the gel blocks any electrical field applied normal to the gel.

One critical issue in microelectrophoresis is the protein detection due to the smaller amounts of sample and the smaller probed areas.[11] As a consequence, high sensitive techniques for the protein detection should be chosen. Commonly, proteins are detected by using a dye (*i.e.* organic, metallic or fluorescent) to color the proteins making them visible optically.[90-94] Other types of protein labeling such radioactive isotope markers have also been reported with striking attomole detection limits, but due to its expensive and cumbersome operation their use have been limited.[94] Protein detection limits close to 5 pg per band have been reported by using fluorescence methodologies, however not all the molecules present native fluorescence and analyte derivatization with expensive fluorescent dyes is required.[9, 92, 93, 95] Organic dyes, like coomassie blue, have

also been extensively used in proteomics for their simplicity and low cost. Nevertheless, given the low sensitivity of the method, its use is often restricted to the fast screening of highly concentrated samples.[91, 96] Silver staining of proteins is also a relatively cheap methodology for protein visualization providing a higher sensitivity (~ 1 ng).[90] As a result, silver staining is often the preferred detection technique of proteins after gel electrophoresis. Recently it has been shown, that by hyphenation of silver staining techniques with scanning electrochemical microscopy (SECM), a sensitivity that competes with fluorescent detection methods (0.5 ng/mm^2) is achieved.[15]

Herein, it is described the miniaturized IEF separation of three proteins, namely β–lactoglobulin, myoglobulin and lactoferrin on a 1 cm long polyacrylamide gel. After blotting on a polymer membrane, protein detection was carried out by silver staining and SECM imaging in the feedback mode. Protein detection is made possible through re–oxidation of the silver stains by a redox mediator during the passage of the scanning microelectrode over the membrane. The high quality of the obtained image (high resolution and low background noise) demonstrates that scanning electrochemical microscopy has the required specifications to image blots from miniaturized gels.

3.2. Experimental section

3.2.1. ***Chemicals***

All the chemicals were used without further purification. Potassium hexachloroiridiate (III) $K_3[IrCl_6]$, formaldehyde (37 wt/vol % solution in water) and 3-Cyclohexylamino-1-propane sulfonic acid (CAPS, $C_9H_{19}NO_3S$, >98 %) were purchased from Sigma-Aldrich (Schnelldorf, Switzerland). Potassium nitrate (KNO_3, ≥99 %), acetic acid (>99.8 %), sodium acetate anhydrous (>99 %), sodium thiosulfate pentahydrate ($Na_2S_2O_3 \cdot 5H_2O$,

>99.5 %), sodium carbonate anhydrous (Na_2CO_3, >99.5 %), silver nitrate ($AgNO_3$, >99.5 %) and ethanol (>96 %) were purchased from Fluka (Buchs, Switzerland). Methanol was purchased from Merck (Dietikon, Switzerland). Immuno-Blot PVDF membranes for protein blotting and IEF standards (pI 4.45 - 9.6) were purchased from Bio-Rad (Hercules, CA, USA). Ampholytes for IEF electrophoresis (3 – 10 pH range, Pharmalytes^{TM}) and polyacrylamide gels for IEF (Clean gel, T=5 %, C=3%) were purchased from GE Healthcare (Zurich, Switzerland). Bovine β-lactoglobulin (≥98 %) and lactoferrin (≥ 95%) as well as horse heart myoglobulin (≥90 %) were purchased from Aldrich (Schnelldorf, Switzerland). Deionized water produced by a Milli Q plus 185 model from Millipore (Zug, Switzerland) has been used. Alumina 1 µm (and 0.05 µm) and mastertex polishing cloths from Buehler (Schlieren, Switzerland) were employed to polish the microelectrode tip.

3.2.2. ***IEF Electrophoresis***

A small piece of polyacrylamide gel (0.5 cm x 1 cm) was soaked in wide pH range mixture (pH 3–10) of carrier ampholytes (5% v/v) during 2 hours for rehydration. Then, one spot (3 mm^2) of the protein mixture (0.5 µL) was applied with a micropipette on the middle of the gel resulting in one running channel. Once the protein samples were completely adsorbed by the gel, two platinum wires of 0.5 cm length were placed over the gel as cathode and anode electrodes. IEF was run in the conditions of table 3.1 with voltage as the limiting factor. The calibration of the pH gradient has been obtained with a mixture of p*I* markers.

Table 3.1. Conditions used for the IEF electrophoresis in 1 cm^2 gel.

Step	*Voltage (V)*	*Current (mA)*	*Power (W/cm²)*	*Time (min)*	*Temp. (°C)*
1	100	2.0	1.0	5	15
2	900	2.0	1.0	30	15

The passive blotting procedure that has been performed was the one presented by Ogorzalek *et al.*[97] to limit the band spreading when switching off the focusing electric field. Briefly, one PVDF piece and four pieces of transfer papers presenting a bigger size than the gel for easier handling (1.2 cm x 1.2 cm) have been prepared. The PVDF membrane was wetted in ethanol (95 %) for 5 minutes while the transfer papers were soaked in a solution of CAPS (10 mM) in ethanol (10%). After the IEF electrophoresis, the gel was placed on a flat glass plate and the wetted PVDF membrane was put on the gel. The pieces of papers were then put over the PVDF membrane and the sandwich was completed by another glass plate and a load of 366 g. After 3 hours, the PVDF membrane was removed and dried at room temperature. The procedure used for staining the PVDF membrane was introduced elsewhere.[15, 98] In brief, the PVDF membrane was submerged during 1 s in methanol and washed for 30 s in deionized water. The membrane was then washed 3 times for 5 min in 1 % sodium acetate. It was then rinsed twice with deionized water for 1 min. The membrane was sensitized 3 times for 5 min in 0.1 % sodium thiosulphate before being rinsed two times with deionized water for 1 min. After, the membrane was soaked in chilled 6 mM silver nitrate and incubated for 20 min at 4 °C. After discarding the silver nitrate, the membrane was rinsed twice with deionized water for 1 min and developed in a mixture of 1 % formaldehyde and 2.5 % sodium carbonate with intensive shaking for 10 min. The procedure was simply repeated

for double staining. The development was stopped in 10 % acetic acid for 5 min. Finally, the membrane was dried at room temperature.

3.2.3. ***SECM measurements***

SECM measurements were carried out using a home–made SECM and a typical three electrodes setup. The electrochemical cell uses silver as quasi–reference electrode (QRE), a platinum wire as counter electrode and a platinum microelectrode disk (20 µm diameter) as working electrode. The platinum microelectrode was polished with a series of alpha alumina from 1 µm down to 0.05 µm particle sizes and the quality of the electrode was checked with a Laborlux D optical microscope (Leitz, Germany). The ratio between the radius of the insulating glass and the radius of the electrode (*RG*) was between 3 and 4. The PVDF membrane was fixed over a microscope glass plate and placed over a platform. All the experiments were performed with a 1.5 mM $K_3[IrCl_6]$ + 0.1 M KNO_3 solution at a working potential (E_T) of 0.8 V vs. Ag QRE and at room temperature (20 ± 2 °C).

3.3. Results and discussion

From a theoretical point of view, miniaturizing IEF electrophoresis should not result in a loss of resolution. Indeed, if parameters such as loading capacity and sensitivity of protein detection are taken into account, microelectrophoresis can theoretically be performed with a resolution similar to that classically obtained with gels of common size but in less time.[10] Then, resolution is a function of some parameters that are protein dependent such as the variation of the protein charge as a function of the pH (*e.g.* p*I*) and others that rely on the experimental set–up (*e.g.* electric field and temperature).

If SECM is considered for imaging gel electrophoresis, the major limitation is the rough surface of the gel. Additionally, as SECM images the upper layers of the gel, it does not allow the complete detection of the total protein amount contained inside the gel. As a result, signals with a low sensitivity and a low resolution are obtained when stained gels are scanned directly by SECM (results not shown). As compared to a gel, the flatness and thickness of a PVDF blotting membrane make easier and more quantitative the SECM imaging process.

The protein transfer efficiency in the blotting process is expected to be between 25 and 55 %.[99] In the present case, it corresponds to a protein amount between 85 ng to 175 ng over the PVDF membrane. However, after silver staining the PVDF membrane, only two weak signals corresponding to myoglobin and β–lactoglobulin were optically observed (see figure 3.1a). The low intensity of these two protein bands and the incapacity of visualizing the lactoferrin band might reveal an even lower blotting efficiency. Concerning the non–detection of lactoferrin, this could be explained by its higher molecular weight as compared to the two other proteins, this inducing a very low transference from the gel to the PVDF membrane. The resulting amount of lactoferrin in the PVDF membrane should thus be lower than the detection limit of the normal silver staining protocol (~ 1 ng). Figure 3.1b shows the SECM image of the PVDF membrane shown in Figure 3.1a.

SECM imaging was performed in a solution of $IrCl_6^{3-}$ (1.5 mM) with a working potential of 0.8 V (E_T). At this potential, steady–state currents are recorded for $IrCl_6^{3-}$ oxidation at the microelectrode surface. When the microelectrode is placed in the

boundaries of the silver stained proteins, recycling of the redox mediator is produced by the silver etching.

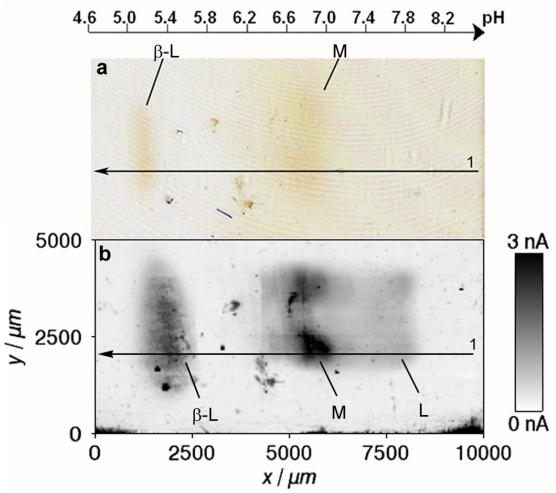

Figure 3.1. a) Optical image of the PVDF membrane after blotting and silver staining from an IEF electrophoresis in 0.5 cm × 1 cm gel. The running channel presents a mixture of lactoferrin (0.7 mg/mL), myoglobin (0.9 mg/mL) and β–lactoglobulin (0.8 mg/mL). The images were recorded with a hewlett packard scanner (resolution of 1200 dpi). b) A constant probe height SECM image (contour plot) of the PVDF membrane (showed in figure 3.1a) in a solution containing $K_3[IrCl_6]$ 1.5 mM and KNO_3 0.1 M. For this image, a 20 µm diameter Pt disk served as the tip. The imaging tip current was 0.0 – 3.0 nA and $i_{T,\infty}$ = 14.52 nA. d = 1 µm. "L", "M" and "β–L" correspond to the proteins bands of the lactoferrin, myoglobin and β–lactoglobulin, respectively. The incrementing step in "x" and "y" direction was 50 µm, while the translation rate was 50 µm/s. The quasi–reference electrode (QRE) used was silver while the counter electrode was a platinum wire.

As a result, an increase of the current is measured. In contrast, when the microelectrode is positioned in the vicinities of the PVDF membrane and in absence of silver stained proteins, the diffusion of the redox mediator to the electrode surface is blocked and lower currents are measured (negative feedback). The high quality of the image is due to a good leveling of the surface and the possible slide of the tip over the PVDF membrane thanks to the low friction properties of PVDF.[15] SECM imaging presents two main advantages over the one attained with the commercial optical scanner presented in figure 3.1a. The first advantage is the higher sensitivity that can be achieved as illustrated by the detection of all three proteins (Figure 3.1b) when only two protein bands are revealed by the commercial optical scanner.

The second advantage that SECM presents is its capability to reveal smaller details than conventional techniques. Indeed, while only one band is observed for myoglobin in Figure 3.1a, the two expected isoforms can be distinguished by SECM (Figure 3.1b). The difference of definition could be explained by the different acquisition principles of the two detection techniques. For example, with optical scanners, spreading problems have already been pointed out as a major drawback, which could bring to a loss of resolution.[100] With SECM, as the imaging is based on current measurements in very specific locations and at different times, the SECM image is built point by point. Thus, it is expected that spreading problems are dramatically reduced and that more accurate information from the image could be extracted. Also, as it has recently been shown by Pietrogrande *et al.,*[101, 102] spot overlapping in 2–DE is likely due to a problem of strip dimension, detector system performance and/or p*I* range. Consequently, according to the present work, as the resolution of the imaging method becomes higher, it can be predicted that the use of SECM would help in reducing the required interdistance for differentiating two adjacent spots.[103]

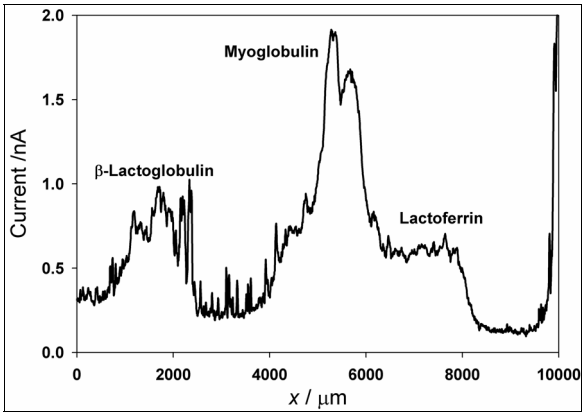

Figure 3.2. Probe scan curve in *x*–direction over the PVDF membrane showed in figures 3.1a and 3.1b (position 1) with a UME of Pt (diameter = 20 μm) in the presence of $K_3[IrCl_6]$ 1.5 mM and KNO_3 0.1 M. The distance between the electrode and the PVDF was equal to cero (*d* = 0 μm). The incrementing step was 5 μm, the translation speed was 50 μm/s. The quasi–reference electrode (QRE) used was silver while the counter electrode was a platinum wire.

Figure 3.2 shows a line scan in *x*–direction as illustrated in figure 3.1a and 3.1b (the arrows indicate the scanning direction) showing the current measured and the resulting resolution. Indeed, if the two myoglobin isoforms are examined, it appears that there is a distance of 0.4 mm between the maximum current values. Thus, it appears that SECM is able to provide a resolution that competes with high resolution scanners that are used for imaging gel electrophoresis (*i.e.* 0.5 mm).[101, 102] Moreover, it has to be pointed out that the SECM imaging resolution can further be improved by using smaller UME diameter and reducing the size steps in *x* and/or *y* direction. This could be advantageous in proteomics for example, where 2D map comparison is the first step toward the discovery of biomarkers.[104, 105]

The major drawback of the present technique for imaging large size areas is the required time, which in our case was approximately 15 hours, but Figure 3.2 clearly shows that line scans obtained in 200 s are suitable for imaging 1D separations. The present results unambiguously show that miniaturized 1D IEF separation can be analyzed with a high resolution in a few minutes, and open the way to high throughput miniaturized IEF.

3.4. Conclusions

Three proteins were separated by miniaturized IEF electrophoresis. After passive blotting to PVDF membrane, the silver stained protein bands were imaged by SECM. In this work, it has been demonstrated that the use of SECM methodology should be positively considered for the detection of proteins after gel electrophoresis. Indeed, as compared to normal optical scanners, SECM provides higher sensitivity and resolution.

Moreover, the high versatility of SECM could be used to tune the imaging resolution depending on the application and the throughput's needs. For example, while full imaging has to be used for 2D separation, line scans requiring only few minutes can be performed for fast screening of 1D separations.

Imaging of 1 cm length electrophoresis represents a big challenge for SECM, since excessive long experimental times, topographic artifacts coming from tilt surfaces and probe-substrate crashes have to be addressed for such a large samples area. Indeed, it is not a problem related uniquely to protein microseparations, but is also present in other interesting samples such as human fingerprint imaging or libraries samples (e.g. protein or catalyst arrays). For this reason, our further efforts were focus on solving these SECM limitations in order to provide a high throughput tool for chemical imaging of rough and tilted large sample areas.

4. ADSORBED PROTEIN DETECTION BY SCANNING ELECTROCHEMICAL MICROSCOPY*

4.1. Introduction

The development of sensitive and selective techniques for protein detection has been extensively pursued since low abundance proteins have been shown to play relevant roles at all the levels of biological processes.[106, 107] In systems such as yeast, these proteins furthermore represent 80 % of the predicted proteome.[5, 108] In gels or in human fingerprints, proteins are usually visualized by optical techniques based on protein staining with either metal ions such as silver,[90] organic substances[91] or fluorescent dyes.[92, 93, 109] Radioactive isotope labels have also been used,[110] but despite of the very high sensitivity with reported attomole detection limits, the handling of radioactive materials and their cost makes the routine use of this technique rather cumbersome.[109] From a sensitivity point of view, fluorescence methodologies are also very powerful. Indeed, detection of proteins, after derivatization[92, 93] or by native fluorescence,[9] has been

* Based on Cortés–Salazar, F., Busnel, J–M., Li, F., Girault, H.H., Adsorbed protein detection by scanning electrochemical microscopy. Journal of Electroanalytical Chemistry, 2009, 635**,** 69–74.

reported with detection limits close to 5 pg per band on polyacrylamide gels and between 0.25 to 1 ng mm^{-2} on polyvinylidene fluoride (PVDF) membranes.[111] Still, this approach is somehow costly as expensive fluorescent dyes and/or fluorescence scanners are required.[95] Electrochemical detection of proteins by scanning electrochemical microscopy (SECM) has been developed in conjunction with techniques like immunodetection[112, 113] or metal staining.[13-15, 114] Recently, it has been reported that the sensitivity of the silver staining technique can be enhanced to 0.5 ng mm^{-2} by the use of SECM as a readout tool.[15]

As a preliminary step to protein quantification, protein structure elucidation is generally carried out in proteomic studies. In this context, as it may provide important information, selective tagging of proteins has been extensively studied by several techniques such as mass spectrometry.[115, 116] One interesting approach is the tagging of free cysteines containing proteins and peptides by benzoquinone.[117] This reaction follows a classical 1,4–Michael addition mechanism with a high selectivity for cysteine groups in acidic pHs (pH < 4) and an extended reactivity for other nucleophilic groups (*e.g.* lysine and histidine) at a higher pH (pH > 4).[118-120] Herein, a new SECM protein detection approach based on the tagging of proteins with benzoquinone and the further electrochemical detection of the quinone–protein adducts by the recycling of a redox mediator is presented. The present methodology is simpler than metal staining and presents the advantage of being suitable for both general (*i.e.* tagging of cysteine, histidine and lysine) and selective (*i.e.* tagging of cysteine) protein detections. Additionally to provide relevant information for protein identification, a sensitivity in the low ng mm^{-2} range is afforded.

Typically, direct detection techniques are sensitive and selective to the analyte of interest, while indirect detection techniques have not such selectivity. However the lack of specificity for one analyte can be an advantage if there is a strong selectivity and sensitivity for another analyte that can be blocked by the analyte of interest. When working with adsorbed proteins on PVDF membranes, an indirect protein detection technique based on the oxygen reduction at PVDF membrane pores can be employed. According to our results the indirect detection technique developed, is sensitive to the presence of protein concentrations close to 50 ng, with the advantage that could be performed faster since no protein labeling step is required.

4.2. Experimental section

4.2.1. ***Chemicals***

KNO_3 (≥ 99 %), KCl (≥ 99.5%), CH_3COOH (> 99.8 %), CH_3COONa (> 99 %), $Na_2S_2O_3 \cdot 5H_2O$ (> 99.5 %), Na_2CO_3 (> 99.5 %), $AgNO_3$ (> 99.5 %) and ethanol (> 96 %) were purchased from Fluka (Buchs, Switzerland). Methanol and $K_3[Fe(CN)_6]$ (≥ 99 %) were purchased from Merck (Dietikon, Switzerland). $K_3[IrCl_6]$ (≥ 99.5 %), bovine serum albumin (BSA) (≥ 90 %) and horse heart myoglobin (MYO) (≥ 90 %) were purchased from Sigma–Aldrich (Schnelldorf, Switzerland). All the chemicals were used as received. Deionized water was produced by a Milli–Q plus 185 model from Millipore (Zug, Switzerland). PVDF membranes for protein blotting were purchased from Bio–Rad (Hercules, CA, USA).

4.2.2. ***Protein tagging and silver staining on PVDF membranes***

1 µL of BSA or MYO solution were deposited over a PVDF membrane with a microsyringe. Previously to the protein spotting, the PVDF membrane was wetted in methanol and water. To avoid the formation of any significant topographical differences, the needle of the microsyringe was not in physical contact with the PVDF membrane during the deposition process. After sample application, PVDF membranes were dried under a gentle nitrogen flux. For subsequent tagging, the whole membrane was then submerged in an aqueous solution of acetic acid (0 – 44 g/L AcOH) with benzoquinone (0.2 mM – 200 mM) for various durations (1 – 12 hours) with constant shaking. For the detection of the hydroquinone protein adducts, a reduction step with a solution of Sn(II) (130 mM $SnCl_2$, 0.5 M HCl, 1.0 M NaCl) was performed overnight. The procedure used for silver staining proteins on PVDF membranes has been introduced elsewhere.[15, 98] The PVDF membrane was then washed extensively with water, dried, taped over a microscopic glass and finally scanned by SECM. Protein inked human fingerprints were prepared by microcontact printing (µCP) as described elsewhere using the fingerprint of one volunteer.[12]

4.2.3. ***SECM measurements***

SECM measurements were carried out using a custom–built SECM setup running under SECMx software[68] and comprising an IVIUM compactstat (IVIUM Technologies, The Netherlands) operating in a classical three–electrode mode or under bipotentiostatic conditions. Data analyses were carried out using MIRA software.[69] The electrochemical cell comprises a silver wire as the quasi–reference electrode (Ag–QRE), a platinum wire as the counter electrode. As the working electrode, a Pt microelectrode (UME) with a

radius equal to 11 µm and a *RG* (radius of the insulating glass sheath over electrode radius (a)) between 3 and 4 if not specified in the figure captions. All potentials are reported with respect to the Ag–QRE. Pt microelectrodes were polished by a succession of diamond lapping discs (Ultra–prep, Buehler, Schlieren, Switzerland) with different particle sizes of 30 µm, 6 µm, and 0.1 µm. After polishing, the quality and the *RG* of the electrodes was checked with a Laborlux D optical microscope (Leitz, Germany). All the samples were mounted on the bottom of a flat table used as sample holder for SECM experiments and SECM images were performed by placing the electrode at a constant height from the surface of the sample (constant height mode). All the measurements were performed at room temperature (20 ± 2 °C).

4.3. Results and discussion

4.3.1. ***Protein tagging reaction and SECM detection principle***

The tagging of proteins with benzoquinone is based on a 1,4–Michael reaction mechanism. The general reaction is depicted as reaction 1 in Scheme 4.1, where "R" is the protein that contains free thiol groups "SH", which can react with benzoquinone to produce a mixture of benzoquinone and hydroquinone protein adducts. The composition of the obtained products can be tuned by the amount of benzoquinone added at the beginning of the reaction (reaction 2 in Scheme 4.1). The protocol for the tagging reaction is simpler than other protein labeling techniques, since it is a one–step procedure where it is only required to wet the PVDF membrane with an acidic or neutral solution of benzoquinone for a given duration (1 – 3 hours). In addition, since this is an endpoint protocol, the membrane can be left in the benzoquinone solution for prolonged periods of time without over staining. This is an important advantage over previous silver staining

techniques in which the staining intensity may significantly vary from experiment to experiment and high background signals can be easily obtained.

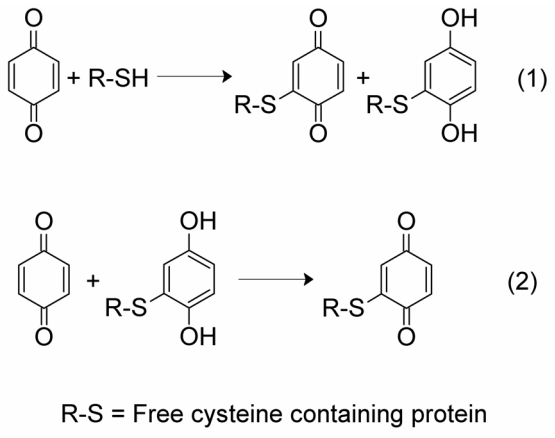

Scheme 4.1. General reactions for the tagging of proteins with benzoquinone.

Depending on the type of protein adduct produced in the tagging reaction, a different strategy for the electrochemical protein detection is proposed. Indeed, either the hydroquinone–protein adducts (Figure 4.1a) or the quinone–protein adducts (Figure 4.1b) can be targeted. The first strategy requires a prior reduction of the quinone–protein adducts before the SECM scanning, to reach a maximum detected quantity of hydroquinone–protein adducts. With this aim, the tagged protein spots were first reduced overnight with a Sn(II) solution (130 mM $SnCl_2$, 0.5 M HCl, 1.0 M NaCl). Then, the PVDF membrane was washed extensively with water and imaged by SECM.

The tagged and further reduced protein spots were then detected by using $IrCl_6^{3-}$ as the redox mediator (see Figure 4.2). Although a protein spot of 50 ng mm^{-2} of BSA was observed, this option was not further selected since hydroquinone species can be easily re–oxidized in the presence of oxygen. As a consequence, the current intensity over the protein spots decreases drastically after the first scan. Before to analyze or re–analyze

these samples, an additional reduction step would have to be performed in order to keep the signal intensity.

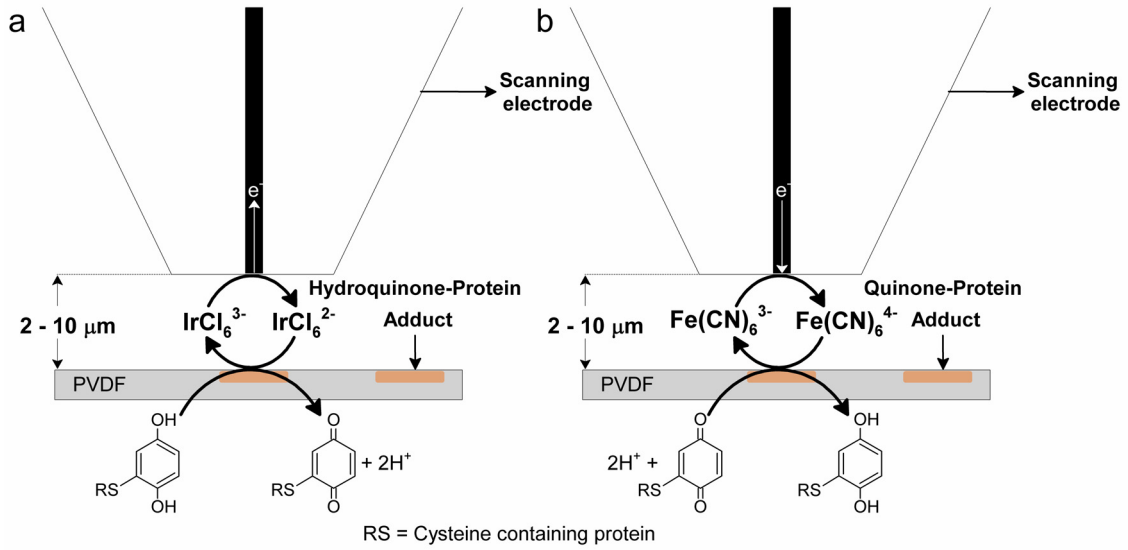

Figure 4.1. Schematic representation of the protein detection principle by the mediated a) oxidation of protein–hydroquinone adducts or b) reduction of protein–quinone adducts.

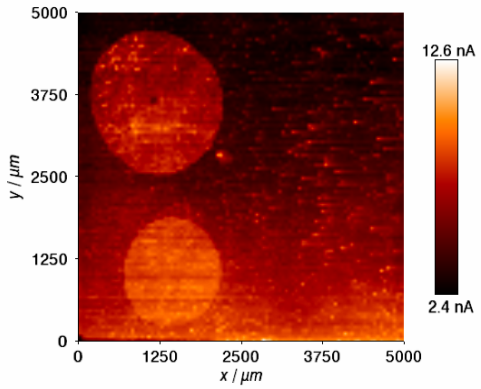

Figure 4.2. Constant height image of four protein spots (bovine serum albumin upper part of the image, myoglobin lower part of the image; protein concentration left 500 ng, right 5 ng) over a PVDF membrane in an aqueous solution of 2.22 mM $K_3[IrCl_6]$ in 0.1 M KNO_3. After tagging with benzoquinone of the adsorbed proteins a reduction with Sn(II) was performed. Experimental conditions: E_T = 0.8 V, Pt UME (r_T = 11 µm, RG = 3 – 4), d = 5 µm, step size = 50 µm, translation rate v_T = 50 µm/s.

This problem has been recently solved for the detection of DNA hybridization, where DNA strands were deposited over a quinone polymer matrix supported on a carbon fiber electrode and the hydroquinone species were *in situ* produced at the negatively biased electrode.[121] A high amount of hydroquinone groups were thus available to undergo a

reaction with the redox species generated at the SECM tip. Herein, as the supporting PVDF membrane is an insulating material, this previously reported approach cannot be applied.

To circumvent these problems, a second strategy (Figure 4.1b) was explored where the recycling of the redox species ($Fe(CN)_6^{4-}$) is associated to the reduction of benzoquinone–protein adducts, which can be the main product if an excess of benzoquinone is employed during the tagging reaction (reaction 2 in Scheme 4.1). In comparison with the first approach, the current intensity over the protein spots remains stable after several scans (see Figure 4.3).

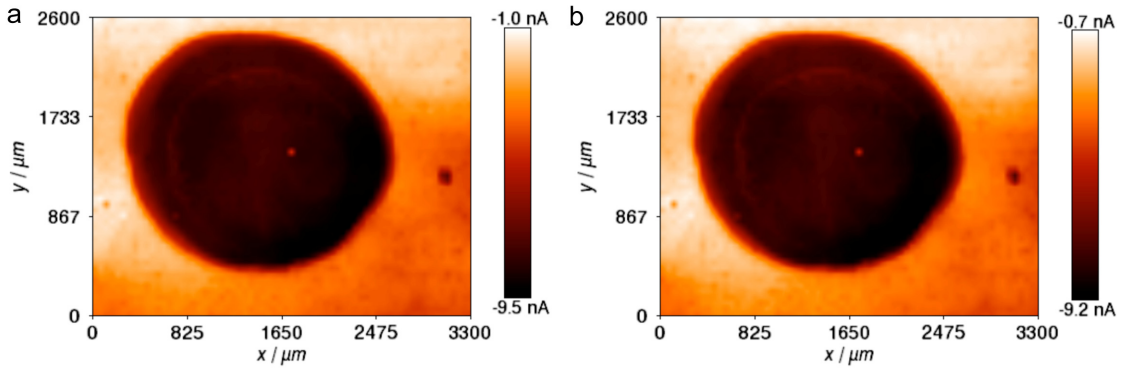

Figure 4.3. Constant height SECM images of a tagged protein spot (over PVDF) with benzoquinone in an aqueous solution of 2.9 mM $K_3[Fe(CN)_6]$ in 0.1 M KNO_3. a) First and b) second SECM images taken consecutively one after the other. Experimental conditions: E_T = –0.2 V, Pt UME (r_T = 11 µm, RG = 3 – 4), d = 4 µm, step size = 50 µm, translation rate v_T = 50 µm/s.

4.3.2. ***Optimization of the tagging reaction***

Two parameters have firstly been considered for optimizing the tagging reaction. With this aim, several protein spots of similar concentration (500 ng mm^{-2} of BSA) were tagged during different durations (1 – 12 hours) and with various benzoquinone concentrations (0.2 – 200 mM) in water without acetic acid. To be able to determine the best conditions, all the protein spots were scanned by SECM under similar experimental conditions (*e.g.* probe–substrate distance, redox mediator concentration, microelectrode,

microelectrode *RG*, translation speed and translation step). The current value was then monitored over each protein spot and the results compared as a function of the varying parameters. For being able to determine the best conditions, the current difference (Δi_T) obtained by subtracting the averaged background current from the averaged current recorded over the protein spot (Figure 4.4a) was taken into account. This current difference was plotted as a function of the different tested conditions (Figure 4.4b and 4.4c).

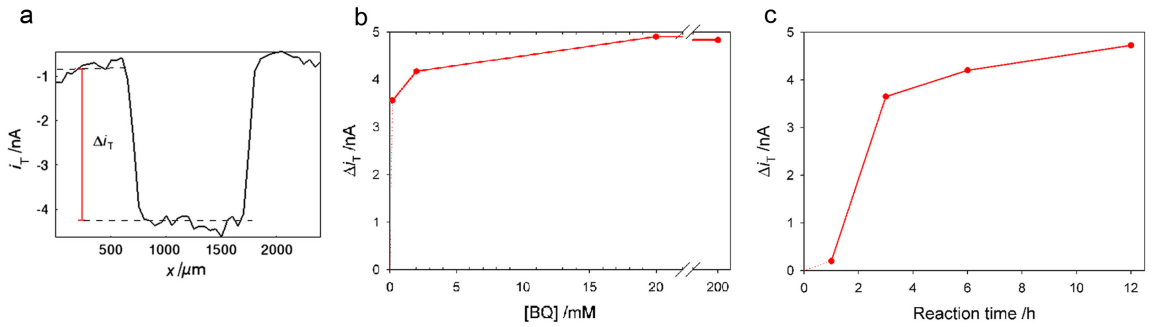

Figure 4.4. a) SECM line scan of a Pt UME (a = 11 μm, *RG* = 2–3) over a protein spot tagged with Benzoquinone. b) Benzoquinone concentration [BQ] and c) reaction time optimization. Δi_T represents the current difference between the protein region and the background (noise). For all the experiments a 500 ng protein spot of BSA over PVDF was prepared. Imaging conditions: 2.0 mM $K_3[Fe(CN)_6]$ in 0.1 M KNO_3, translation rate v_T = 50 μm s^{-1}, step = 50 μm, d = 4 μm and E_T = –0.2 V.

For the benzoquinone concentration, it can be seen that 20 mM benzoquinone concentration is appropriate for the tagging reaction, since no further increment on the current difference is observed at higher concentrations (Figure 4.4b). Additionally, higher concentrations of benzoquinone are hardly obtained due to the limited benzoquinone solubility in water. A benzoquinone excess was employed for the tagging reaction as it not only tags the cysteine groups but also other nucleophilic aminoacids (*vide infra*). Also, benzoquinone acts as an oxidative agent for hydroquinone protein adducts (reaction 2 in Scheme 4.1). Then considering Figure 4.4c, three hours was subsequently chosen as the optimum reaction time as it provides a good compromise between signal intensity and

experiment duration. Previous studies performed in solution showed that a tagging reaction yield of almost 100% was achieved in 1 hour.[120] The longer experimental time required in the present methodology is certainly a consequence of the heterogeneous nature of the reaction occurring between benzoquinone and adsorbed proteins. As the reactive species in this Michael type reaction is mainly the thiolate ($-S^-$), the reaction rate can also be affected by the pH of the solution. Other experimental parameters such as the charge of the neighboring groups and the steric hindrance induced by the protein structure may also lower the availability of free cysteine groups. [119, 122, 123] In this work, the solution pH was 6.4, which provides an appreciable amount of thiolate groups without affecting the benzoquinone stability. As reported in other studies, if further required, the rate of the tagging reaction may also be enhanced by using benzoquinone derivates with electron withdrawing groups, like the carboxymethyl.[124]

4.3.3. ***Sensitivity and selectivity***

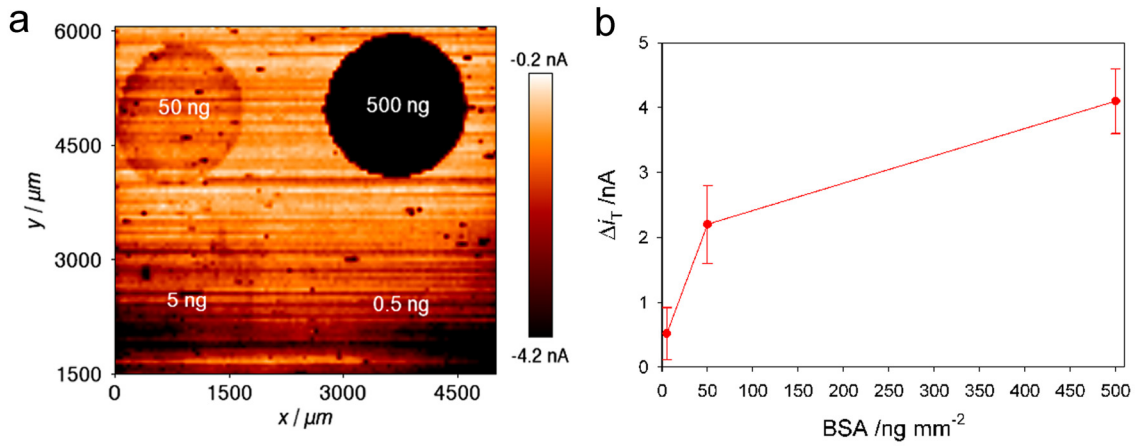

Figure 4.5. a) Constant height image of tagged BSA protein spots over a PVDF membrane in an aqueous solution of 2.1 mM $K_3[Fe(CN)_6]$ in 0.1 M KNO_3. Tagging reaction conditions: Benzoquinone = 20 mM, reaction time = 3 hour and pH = 6.15. Imaging conditions: translation speed v_T = 50 µm s^{-1}, step = 50 µm, d = 4 µm and E_T = –0.2 V. b) Current difference between the protein region and the background (Δi_T) as a function of the BSA concentration.

The sensitivity of the present technique was assessed by spotting different protein quantities with concentrations ranging from 0.5 to 500 ng mm^{-2} on a PVDF membrane. The protein tagging was then performed under the previously optimized conditions. As demonstrated by the Figure 4.5a, the protein spots corresponding to protein amounts of 500 ng, 50 ng and even 5 ng can be detected by using the proposed detection technique. The spot containing 0.5 ng of BSA could not be observed. From Figure 4.5 and the SECM imaging of a similar sample (result not shown), 8 line scans were extracted by using MIRA software (4 line scans from each image) in order to establish for each protein spot the current difference (Δi_T). Average values of these differences were then plotted against the BSA surface concentration. The results are showed in Figure 4.5b, where the error bars correspond to the standard deviation of the calculated current differences. Despite the minimum protein surface concentration observable with this method is 5 ng mm^{-2}, the statistical value of the limit of detection is undoubtedly higher as the observed background noise is rather strong (signal to noise ratio of 1.6 for 5 ng mm^{-2}). Still, in addition to the proof of concept of the methodology, it can be assessed that the developed method allows for a limit of detection in the low ng·mm^{-2} range, which is of the same magnitude as those provided by the state of the art protein detection over PVDF membranes.[95, 125, 126]

However the current difference increases with the protein concentration, further experiments will have to be performed to thoroughly characterize the proposed method by for example determining its limit of quantification and linear dynamic range. Therefore more protein concentration points will have to be considered and a special attention to the generated background noise will have to be given.

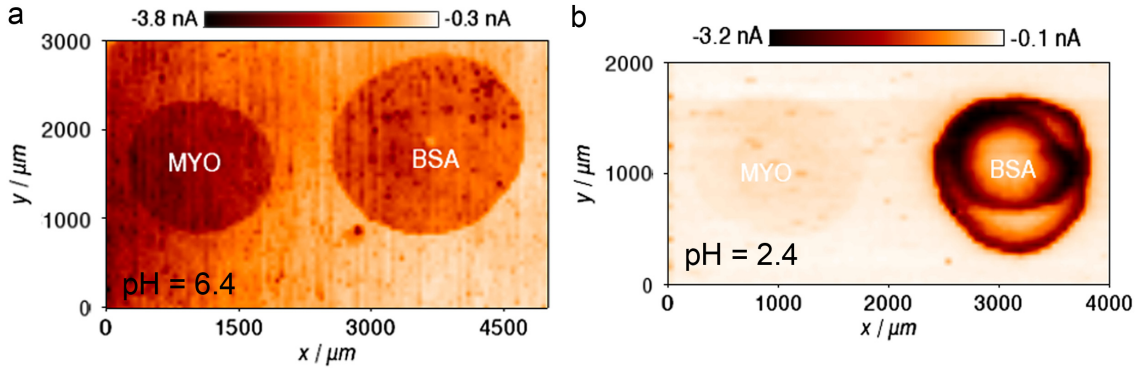

Figure 4.6. Constant height images of tagged BSA (500 ng) and MYO (500 ng) protein spots over PVDF membrane in an aqueous solution of 2.2 mM $K_3[Fe(CN)_6]$ in KNO_3 0.1 M. Tagging reaction conditions: a) pH = 2.44 and b) pH = 6.4 (the pH was adjusted with acetic acid), benzoquinone = 20 mM and reaction time = 3 hours. Imaging conditions: translation speed = 50 µm s^{-1}, step = 50 µm, d = 4 µm and E_T = –0.2 V.

As compared to other techniques, the developed approach presents the advantage of being suitable for both general or cysteine selective protein detections, since the selectivity of the tagging reaction can be tuned simply by changing the pH of the reaction. Under rather strong acidic conditions (pH < 4), only free cysteine groups are tagged while a more universal detection is provided when the tagging reaction is carried out under weakly acidic conditions, where benzoquinone also reacts with other nucleophiles (*e.g.* lysine and histidine). To demonstrate this capability, BSA and MYO were employed as test proteins. BSA contains 35 cysteine groups, but only one free cysteine is available for the tagging reaction and MYO does not contain any cysteine amino–acid residues inside its structure. The results shown in Figure 4.6 confirm this capability. Thereby, relevant information for protein identification and sensitive protein quantification may be obtained in parallel. The low background current observed over the protein spot of MYO at pH 2.44 is more likely originating from the electrochemical activity of the iron contained in the protein rather than from a partial tagging. These results are in good agreement with the results obtained by performing the same reaction

at different pH's and studying the reaction products by mass spectrometry.[120] This is probably, the first protein SECM detection method that can be employed for both general and cysteine selective protein detections.

4.3.4. ***SECM imaging of human fingerprint***

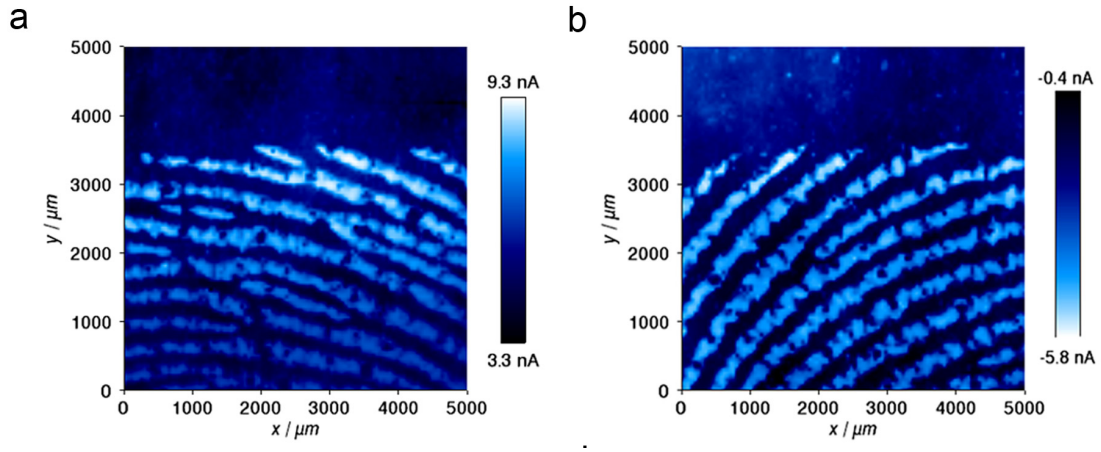

Figure 4.7. Constant height images of a fingerprint developed by a) silver staining (E_T = 0.8 V) or b) benzoquinone tagging (E_T = –0.2 V). Imaging conditions: d = 5 µm, step size = 50 µm, translational rate v_T = 50 µm s^{-1}, Pt UME (r_T = 11 µm, RG = 3–4), counter electrode Pt, reference electrode Ag–QRE. 2 mM $K_3[Ir(Cl)_6]$ in 0.1 M KCl and 2 mM $K_3[Fe(CN)_6]$ in 0.1 M KNO_3 were used as redox mediators for figure 4.7a and 4.7b, respectively.

Just as silver staining,[12] this new protein detection method can be employed in conjunction with SECM for various applications. As an example, its application to the imaging of human fingerprints is reported herein. After having obtained a human fingerprint by a previously described protocol,[12] the sample was cut into two pieces, one being submitted to silver staining and the other one to benzoquinone tagging. Afterwards, a portion of each piece was imaged by SECM using either hexachloroiridiate or ferrocyanide as redox mediator (Figure 4.7). From the two images, it is possible to identify several factors relevant for the verification of a human identity (*i.e.* the position of the ridges and their deviations as well as the shape and relative position of the pores of each part of a ridge). Considering the Figure 4.7, it appears that the new methodology

reveals the same level of information than the actual SECM state–of–the–art for fingerprint imaging. According to a previous report,[15] silver staining provides a higher sensitivity due to both a higher number of active species per protein molecule and a higher apparent heterogeneous kinetic constant. This is confirmed by comparing approach curves performed either over a benzoquinone tagged or silver stained protein spot (2 µg of BSA) with the model proposed by Cornut *et al.*[42] (Figure 4.8). The values of the apparent heterogeneous kinetic constant (k) for the reduction of the benzoquinone–protein adducts and the dissolution of silver nanoparticles were determined to be equal to $8.0 \cdot 10^{-4}$ cm s^{-1} and $2.5 \cdot 10^{-3}$ cm s^{-1}, respectively.

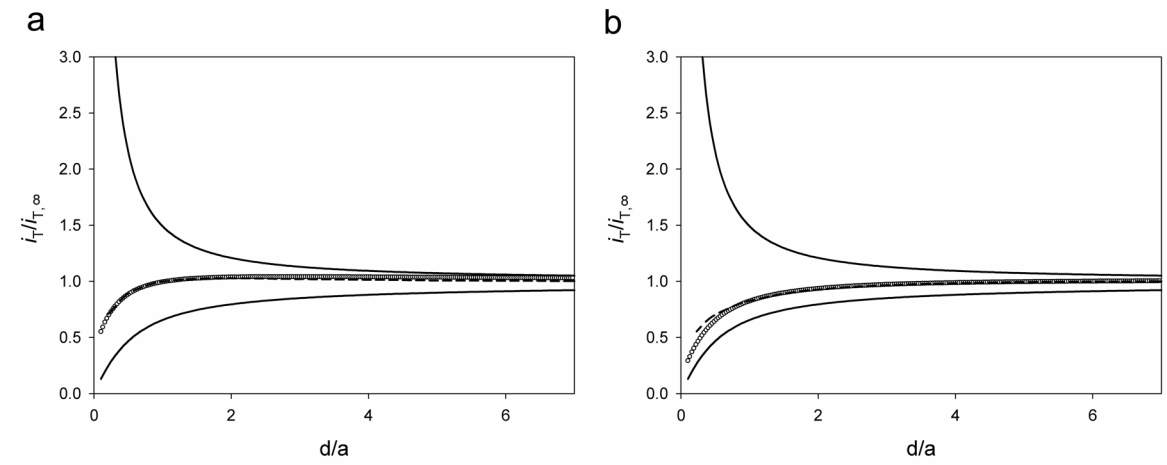

Figure 4.8. Normalized approach curves (dashed lines) on a) silver stained (E_T = 0.8 V) and b) benzoquinone (E_T = –0.2 V) tagged protein spots deposited over a PVDF membrane. The dashed lines correspond to experimental curves and the open circles to the theoretical fittings. The continuous lines represent the theoretical approach curves over an insulating and a conductive substrate from reference 23. Experimental conditions: Pt UME (r_T = 11 µm, RG = 3), translation rate v_T = 0.5 µm s^{-1}, counter electrode Pt, reference electrode Ag–QRE. 2.4 mM $K_3[Ir(Cl)_6]$ in 0.1 M KCl and 2.2 mM $K_3[Fe(CN)_6]$ in 0.1 M KNO_3 were used as redox mediators for figure 4.8a and 4.8b, respectively.

4.3.5. ***Indirect protein detection technique***

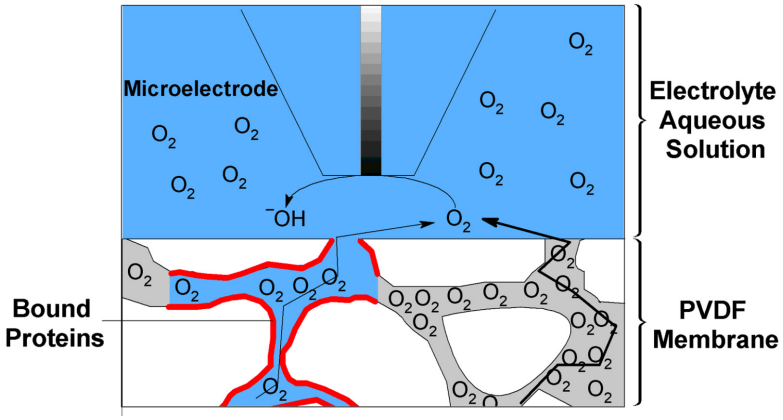

Figure 4.9. Schematic representation of the indirect protein detection principle by the reduction of oxygen.

A schematic representation of the indirect protein detection principle is shown in Figure 4.9. The PVDF membrane is a common hydrophobic porous solid-phase support for proteins with a high binding capacity. Normally, due to its hydrophobicity water is not allow to fill the empty pores and therefore they are filled with air. The oxygen concentration in water at 25 °C and 1 atm is equal to 8.6 mg L^{-1},[127] while at the same conditions in air is around 288 mg L^{-1}. The detection principle is then based on the local decrease of the membrane pore hydrophobicity when proteins are bound to the wall of the membrane pores. This change in hydrophobicity is most likely due to the orientation of the polar groups of the protein toward the inner part of the membrane pore, while the non-polar groups are oriented to the pore wall.[128, 129] As a consequence, water pore-permeation is allowed, producing a decrease on the oxygen concentration inside the pores (see Figure 4.9).

The electrochemical reduction of oxygen proceeds in absence of protons as follows,

$$2H_2O + O_2 + 4e^- \longrightarrow 4OH^-$$

and it has been extensively employed for oxygen detection in Clark type electrodes, for instance, for SECM mapping of oxygen flux trough a porous surface at the gas–phase.[127]

Additionally, the scheme shown in Figure 4.9 has been applied in a redox competition SECM mode for screening the catalytic activity of several catalysts for oxygen reduction[130-132] and for studying the oxygen permeability of gas diffusion electrodes by SECM.[133] By biasing the microelectrode at –0.8 V (*vs* Ag-QRE), the controlled mass-transport reduction of oxygen can be achieved at the Pt microelectrode in a solution of KCl 0.1 M as it can be seen in the cyclic voltammetry shown in Figure 4.10.

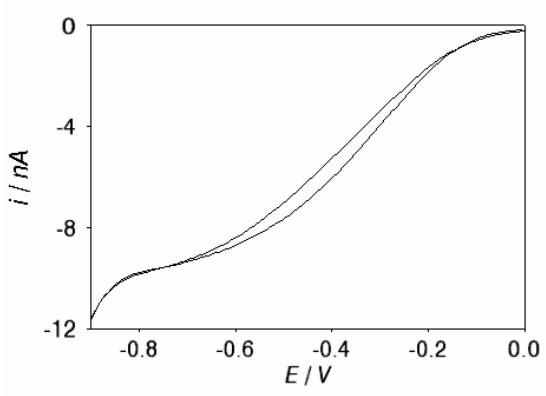

Figure 4.10. Cyclic voltammetry at a Pt microdisc (diameter = 25 μm, RG = 3 – 4) in a solution of KCl 0.1 M. Counter electrode Pt, quasi reference electrode Ag. Scan rate 10 mV/s.

A clear steady–state current is not observed in Figure 4.10, since oxygen reduction produces a local increase on the pH close to the microelectrode shifting this electrochemical process to more negative values.[127] By approaching toward a PVDF membrane a biased Pt microelectrode (E_T = –0.8 V) in a KCl solution, two different behaviors are observed depending whether or not there is protein adsorbed on the PVDF membrane. Figure 4.11, shows that an increase on the current at the microelectrode is observed when the probe gets closer to a PVDF membrane region free of protein, as a higher oxygen concentration is detected. In this case, the depletion of the oxygen concentration produced by the approaching electrode promotes the diffusion of oxygen from the pores to the electrode surface. In contrast, when the electrode is approached to a

protein–containing region, a decrease on the current is recorded as the diffusion of oxygen is blocked and the oxygen concentration inside the pores with adsorbed proteins is similar to the one in solution.

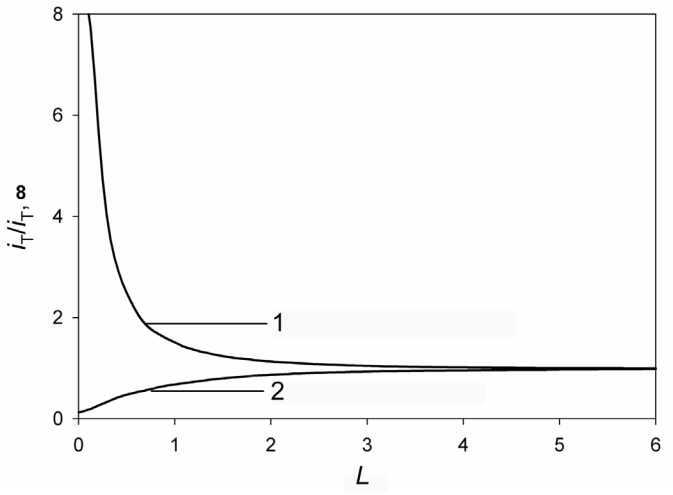

Figure 4.11. Normalized approach curves over a PVDF membrane without (1) and with (2) protein in a solution of KCl 0.1 M. Working electrode Pt disc (diameter = 25 μm, RG = 3 – 4), Counter electrode Pt, QRE Ag. Step size 0.5 μm and translation rate v_T 1 μm/s.

Therefore, by imaging a PVDF membrane with a microelectrode under diffusion-controlled conditions for oxygen reduction, protein-containing regions appear as low density current zones and free-protein regions as high density current zones (see Figure 4.12). As a proof of concept, this new indirect detection technique was applied to the SECM imaging of human fingerprints. Figure 4.12 shows the same human fingerprint imaged by the direct detection method based on the mediated reduction of quinone-protein adducts (Figure 4.12a) and the present indirect detection method (Figure 4.12b). The sample was prepared as outlined above, with the difference that before benzoquinone tagging, the sample was first submerged in a KCl solution and imaged by the principle depicted in Figure 4.9. Afterwards, the electrolyte was replaced by the tagging solution (20 mM benzoquinone) and imaged after tagging in a solution of $K_3[Fe(CN)_6]$ (2 mM) in

0.1 M KNO_3. In between experiments, mechanical polishing renewed the microelectrode surface. SECM images of tagged or silver stained proteins have been obtained as well by the present indirect method, showing no effect on the current contrast (results not shown).

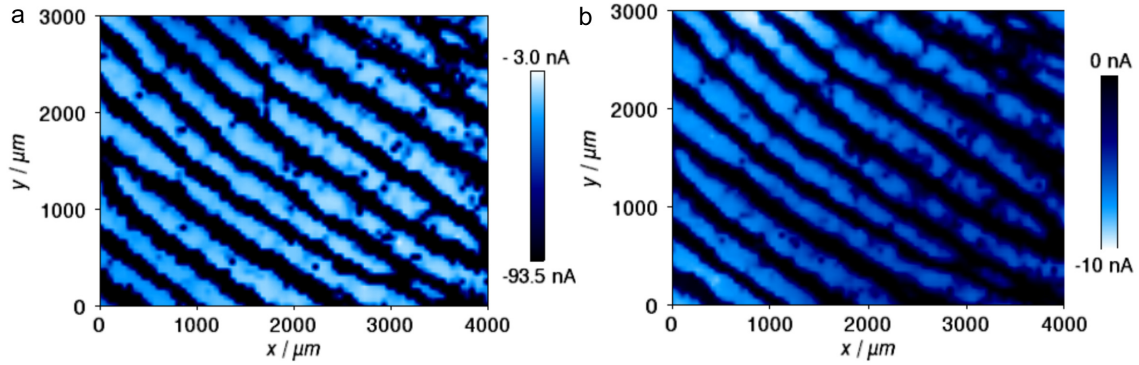

Figure 4.12. Constant height images of a fingerprint obtained by a) the indirect detection method (E_T = –0.8 V) or b) benzoquinone tagging (E_T = –0.2 V). Imaging conditions: d = 3 µm, step size = 50 µm, translational rate v_T = 50 µm s^{-1}, Pt UME (r_T = 11 µm, RG = 3 – 4), counter electrode Pt, reference electrode Ag–QRE. A solution of 0.1 M of KCl was used for Figure 4.12a, while 2 mM $K_3[Fe(CN)_6]$ in 0.1 M KNO_3 was used as redox mediator for Figure 4.12b.

The two SECM images shown in Figure 4.12 reveals important information concerning the features of the imaged fingerprint area, however the image obtained by the indirect detection method presents a higher current contrast. As a consequence, a higher resolution thanks to the big difference in oxygen concentration over the containing-protein and free-protein regions. It is important to notice that the indirect detection method is not based in a feedback effect, but in a forward imaging of oxygen concentration.

The major drawback of the indirect detection method is the lost of current contrast resolution, when employing lower amounts of adsorbed proteins (see Figure 4.13). The fingerprint shown in Figure 4.12 was prepared with a BSA protein solution equal to 5 g m L^{-1}, providing a high amount of protein adsorbed on the PVDF membrane, however when detecting protein spots of different concentrations, the lower detectable amount was 50 ng mm^{-2} of BSA. In spite this is not as sensible as benzoquinone tagging or silver

stained, still can be classified in between the state-of-the-art for protein detection techniques on PVDF membranes. Moreover by using this method, no protein labeling or redox mediator is needed for the detection of adsorbed proteins on PVDF membranes.

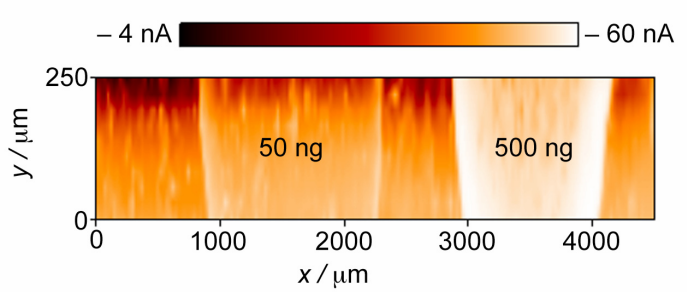

Figure 4.13. Constant height image of tagged BSA protein spots over a PVDF membrane in an aqueous solution of KCl 0.1 M. Imaging conditions: translation speed v_T = 50 µm s^{-1}, step = 50 µm, d = 3 µm and E_T = –0.8 V.

4.4. Conclusions

A new approach for protein detection on PVDF membranes has been developed taking advantage of the reaction occurring between benzoquinone, proteins and peptides. By using a scanning microelectrode and the recycling of a redox mediator ($Fe(CN)_6^{3-}$), the spatial localization of tagged protein spots can be determined. Depending on the requirements, cysteine selective or universal protein detections can be achieved by simply tuning the pH during the tagging reaction. Under rather strong acidic conditions, only free cysteines are available for tagging while other amino acids such as lysine and histidine react at a higher pH. These results demonstrate the feasibility of using SECM to detect benzoquinone tagged proteins when immobilized on a porous membrane surface. Besides being potentially suitable for protein quantification, the proposed detection method should also be suitable for studying the transduction of an oxidant signal into a biological response and the elucidation of available cysteines groups within natural or engineered proteins. It has also to be noticed that the reported detection technique is fully

compatible with mass spectroscopy. As such, it might be considered as an interesting preliminary step to improve the confidence of the identification process.

The present results demonstrated additionally the feasibility of using SECM to detect immobilized proteins on a porous hydrophobic membrane surface, taking advantage of the oxygen concentration differences between the aqueous solution (*i.e.* lower concentration) and at the PVDF membrane pores (*i.e.* higher concentration). As a proof of concept, this new indirect detection technique was applied to the SECM imaging of human fingerprints, revealing the same level of information than the actual state-of-the-art. One major advantage of this technique is that no protein labeling is needed, which not only reduce the experimental time, but also the running costs of the experiment.

5. SOFT STYLUS PROBES FOR SCANNING ELECTROCHEMICAL MICROSCOPY*

5.1. Introduction

The response of a SECM probe depends on the surface reactivity of the sample and the distance *d* between the surface and the active area of the probe electrode. In order to obtain a reactivity image that is not influenced by topography, *d* must be kept constant. In conventional SECM operations, this is achieved by working on samples with a roughness that is considerably smaller than the radius r_T of the UME and by leveling the plane of the sample surface with respect to the *x,y*–scanning plane of the positioning system. However, this approach becomes inappropriate on rough surfaces of large aspect ratios or when large scan areas (in the mm^2 range) have to be investigated so that levelling becomes a major obstacle. Similar limitations apply when imaging curved samples.

This drawback has been recognized for a long time. In case of small r_T, a constant *d* can be maintained by coupling of SECM with scanning ion conductance microscopy

* Based on Cortés–Salazar, F., Traeuble, M., Li, F., Busnel, J–M., Gassner, A., Hojeij, M., Wittstock, G., Girault, H.H.,. Soft Stylus Probes for Scanning Electrochemical Microscopy. Analytical Chemistry, 2009, 81**,** 6889–6896.

(SICM),[134] by working in a tip-position modulation SECM (TPM-SECM) mode with a supplementary system that allows close feedback loop positioning of the probe,[135, 136] by combining atomic force microscopy (AFM) with SECM (AFM–SECM)[50, 137-143] or by combination of SECM with electrochemical tunneling microscopy (ESTM).[144] The integrated AFM–SECM probes proposed by Kranz *et al.* contain an insulating thorn that is used for AFM imaging and at the same time defines a constant *d* for the frame electrode exposed by a focused ion beam.[138, 145] This process has then been extended to wafer–level batch fabrication for reproducible production of standard AFM–SECM tips.[146] AFM–SECM probes have also been produced by attaching single–walled carbon nanotubes (SWNT) at the top of an AFM tip.[147] Furthermore, metal–nanowires AFM–SECM probes have been built from SWNT by metal coating followed by insulation with a polymer film and final electrode exposition by focused ion beam (FIB).[148, 149] By tilting the obtained disc–shaped probe by 11°, a physical contact can be established between one side of the insulating probe apex and the substrate while the active electrode area remains at a given distance from the sample. These nanowire AFM–SECM probes have been used in intermittent contact mode for high resolution imaging of both topographical and electrochemical surface information.[149, 150] The combined experiments are typically carried out with designated AFM or ESTM instruments that rely on piezo positioners limiting their horizontal, and in particular, vertical scan ranges.

For rough surfaces and for sample areas larger than the typical large AFM scans (commonly maximum of 100 μm × 100 μm × 10 μm), a distance control has been achieved by shear–force detection in combination with a positional feedback system.[145, 151-156] Since the shear forces have to be measured in a viscous liquid, the signal change

upon approach is rather small. Because long integration times have to be used, lateral translation rates are restricted. This becomes limiting when imaging large areas. The use of alternating current scanning electrochemical microscopy (AC–SECM) has also been proposed to circumvent these difficulties. However, the distance measurement is difficult to interpret quantitatively, since it depends on the cell setup, the nature of the sample, frequency and electrolyte conductivity.[157-161]

Despite these efforts, challenges remain both for achieving higher lateral resolution and for inspection of larger sample regions. This chapter addresses the latter issue encountered, for example when imaging silver–stained proteins after gel electrophoresis,[15] human fingerprints[12, 162] and negative photographic films.[163]

Here, a new type of amperometric probe for SECM produced by sealing with a polymer film a carbon track microfabricated on a polyethylene terephthalate sheet is proposed. These soft stylus probes are designed to bend when pressed against a substrate such that the polyethylene terephthalate layer is always in contact upon bending. The thickness of this layer defines a constant working distance between the substrate and the active electrode area. When scanning over a rough surface, the bending of the probe can accommodate the topographic features thereby keeping a quasi–constant working distance without the need of an external electronic feedback system like in AFM measurements and can even provide images of surfaces too rough to be imaged by AFM. In contrast to shear–force approaches, no accumulation of the shear force signal is necessary and larger lateral scan rates become possible. Numerical simulations by the boundary element method (BEM) were performed in order to understand the distance–dependent signals of the soft stylus probes.

5.2. Experimental section

5.2.1. ***Chemicals***

$K_3[IrCl_6]$ (≥ 99.5 %, Sigma–Aldrich, Schnelldorf, Switzerland), ferrocene methanol ($FcCH_2OH$, ≥ 97 %, Sigma–Aldrich), KNO_3 (≥ 99 %, Buchs, Switzerland), KCl (≥ 99.5%, Fluka), $K_3[Fe(CN)_6]$ (≥ 99 %, Merck, Dietikon, Switzerland) were used as received. Deionized water was produced by a Milli–Q plus 185 model from Millipore (Zug, Switzerland).

5.2.2. ***Soft stylus probe fabrication***

Microchannels were prepared into 100 µm thick polyethylene terephthalate (Melinex®, PET, Dupont, Wilmington, DE, USA) by UV–photoablation through a metallic mask using a 193 nm ArF excimer laser beam (Lambda Physik, Göttingen, Germany, fluence = 0.25 J, frequency = 50 Hz) as reported before for lab on a chip applications (see Figure 5.1a).[164, 165] The width, depth and length of the prepared microchannels were usually 40 µm, 20 µm and 5 cm, respectively. Carbon ink (Electrador carbon ink, Electra Polymer & Chemicals Ltd., Roughway Mill, Dunk Green, England) was manually applied into the microchannels to create a carbon ink track and subsequently cured at 80 °C for 1 h (see Figure 5.1b). Then, two polyethylene/polyethylene terephthalate (PE/PET, Payne, Wildmere Road, Banbury, England) lamination foils were applied over the electrode, not only to cover and seal it, but also to adjust the mechanical rigidity (see Figure 5.1c).

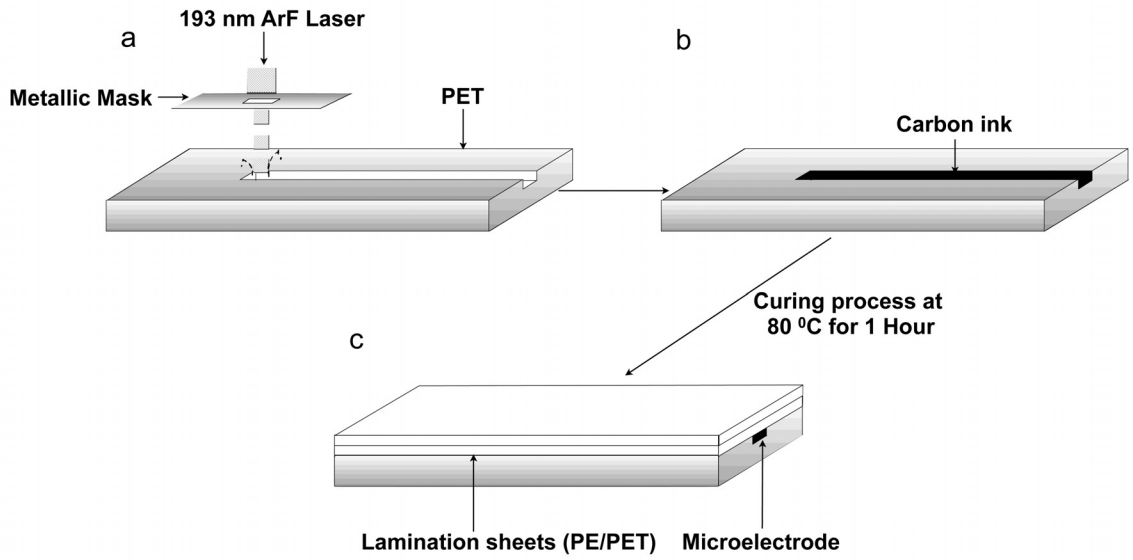

Figure 5.1. Schematic representation of the soft stylus probe microfabrication by laser ablation. a) Microchannel ablation on a PET film, b) microchannel filling with carbon ink and c) carbon track isolation by two PE/PET laminations films.

The soft stylus probe was then cut manually in a V shape such that the width of the probe at the end was about 0.5 – 1 mm (Figure 5.2a). The rigidity of the stylus depends on the tapering used during the cutting process. A cross section of the carbon track was then exposed either by laser ablation or by mechanical cutting and polishing by a succession of diamond lapping discs (Ultra–prep, Buehler, Schlieren, Switzerland) with different particle sizes (30 μm, 6 μm, and 0.1 μm). Sheet resistance measurements were performed using a collinear four–point probe with a 1 mm separation between points (Jandel Engineering Ltd, U.K.).

5.2.3. ***Preparation of gold films***

Glass slides were treated with Piranha solution and cleaned by sequential sonication in ethanol, acetone and purified water followed by drying under a stream of Argon. **Caution:** *This mixture reacts violently with all organic material. Piranha solution has to be handled with extreme care to avoid personnel injury and property damage.* Gold

films, 100 nm thick, were prepared in an Edwards Auto 306 evaporator operating at a pressure less than 5×10^{-6} mbar. The film growth was initiated by thermal evaporation of a 1 nm thick chromium (99.99 %, Balzers) layer at < 0.1 nm/s in order to enhance the adhesion of the Au layer. Gold (99.99 %, Balzers) was subsequently evaporated at < 0.1 nm/s up to 5 nm, before increasing the deposition rate to 0.2 – 0.3 nm/s for the deposition of a 100 nm layer.

5.2.4. ***Preparation of carbon band electrode patterns***

Two different sets of carbon bands were prepared. The first one was composed by two screen printed carbon bands over a polyester film. These two bands separated by 100 μm presented an average thickness and band width equal to 7.1 μm and 900 μm, respectively. Another two carbon bands were screen printed over a glass slide with an approximately band separation of ~1500 μm. The average thickness and band width obtained in this case was 118 μm and 1900 μm, respectively. Topography profiles of the prepared samples were taken with a contact profilometer (Tencor Alpha–step 500).

5.2.5. ***SECM measurements and simulation***

SECM measurements were carried out using a custom–built SECM setup running under SECMx software[68] and comprising an IVIUM compactstat (IVIUM Technologies, NL) operating in a classical three–electrode setup. Data analyses were carried out using MIRA software.[69] The electrochemical cell comprises a silver wire as quasi–reference electrode (Ag–QRE), a platinum wire as counter electrode, and a soft stylus probe as working electrode. All potentials reported herein are with respect to the Ag–QRE. Pt microelectrode was polished using alumina 1 μm and 0.05 μm on Mastertex polishing

cloths (Buehler). After polishing, the quality of the electrodes was checked with a Laborlux D optical microscope (Leitz, Germany). All the samples were mounted on the bottom of a flat cell and investigated at room temperature (20 ± 2 °C). The BEM simulations were performed on a Linux openSUSE 10.3 platform with a 2 GHz Core(TM)2 Duo CPU and 4 GB of RAM. The simulation of individual geometric configurations took 4 min for conducting substrates (4966 boundary elements) and 38 min for insulating samples (11493 boundary elements)

5.3. Results and discussion

A schematic representation of the soft stylus probe obtained by the method described above is shown in Figure 5.2a. Figure 5.2b shows an example of a carbon electrode exposed by laser ablation machining (thickness = 6 μm, width = 32 μm) and Figure 5.2c displays an example of a carbon electrode exposed by blade cutting and mechanical polishing (thickness = 10 μm, width = 30 μm). These images show clearly that the carbon track shrinks during the curing process and the thickness of the electrode is smaller than the depth (*i.e.* 20 μm) of the microchannel used to define the track. The thickness of the carbon electrode depends on the microchannel filling process, which is carried out manually and therefore poorly controlled. In order to fabricate more reproducible electrodes, automated screen–printing techniques should be used. However, it is important to realize that the lamination method can accommodate the recess created over the cured ink track.

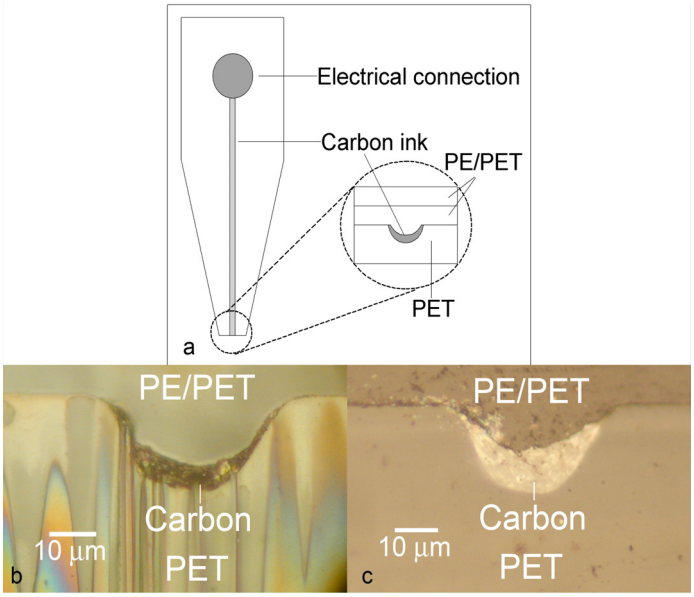

Figure 5.2. a) Schematic representation of the soft stylus probe used as working electrode for SECM; b) optical image of the carbon electrode exposed by laser ablation (thickness 6 µm, width 32 µm) and c) optical image of the carbon electrode exposed by mechanical polishing (thickness 10 µm, width 30 µm).

The soft stylus probes have been firstly characterized in an unbent state and immersed in the solution bulk, by approaching substrates with the active probe area parallel to the sample surfaces, and finally, in a contact mode, *i.e.* with a bent probe pressing as a flexible stylus on the substrate (Figure 5.3a–c).

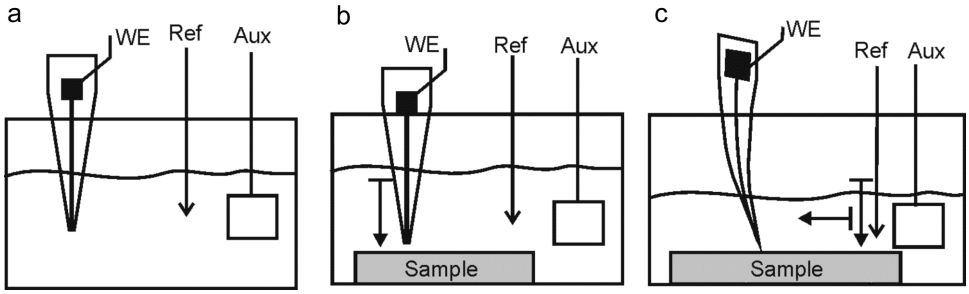

Figure 5.3. Operation mode of the soft stylus probes: a) characterization in the solution bulk, b) approach curves of unbent probes and c) approach curves and horizontal scans of bent probes.

5.3.1. ***Voltammetric characterisation***

Cyclic voltammetry in 2.0 mM $FcCH_2OH$ was used to characterize the electrochemical behavior in bulk solutions as depicted in Figure 5.3a. A sigmoidal response is obtained; indicative of hemispherical diffusion together with low charging current as a consequence

of good sealing between the carbon track and the covering polymer layer (Figure 5.4). The difference of the steady–state currents of individual probes in Figure 5.4 reflects the different geometric areas of individual probes that can vary by ~40 %. In order to compare the quality of the exposed electrode area, a wave–slope analysis of the cyclic voltammograms (CV) in Figure 5.4 was performed by plotting the applied electrode potential E_T as a function of $\log[(i_{T,\infty}-i_T)/i_T]$, where $i_{T,\infty}$ represents the diffusion–limited current in the solution bulk and i_T is the current at given potential in the bulk solution. This analysis gave slope values of 61.4 mV and 62.0 mV for the laser ablated and mechanically polished electrodes, respectively. The slightly better electrochemical behavior shown by the soft stylus probes exposed by laser ablation is a likely consequence of the laser activation of the carbon flakes of the cured ink, similar to findings of previous studies.[166-169]

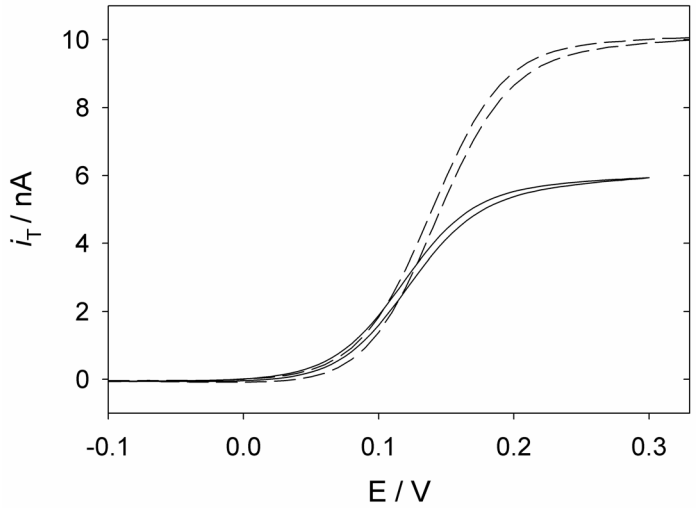

Figure 5.4. Cyclic voltammetry at a soft stylus probes exposed by laser ablation (continuous line) and mechanical polishing (dashed line) in 2.0 mM $FcCH_2OH$ and 0.1 M KNO_3. Scan rate 10 mV/s.

The difference existing between the experimental slope values and the theoretical value (59.1 mV)[48] for a reversible system comes in part from the internal resistance along the carbon track. The sheet resistance of cured screen printed carbon ink, which

represents the ratio between the electrical resistivity and the thickness of a film, was measured using a four point probe to be equal to 7.7 Ω. The resistance (*R)* of the carbon track of width *w* and length *l* is then given by:

$$R = R_s \frac{l}{w} \tag{5.1}$$

With a length of 5 cm and a width of 30 μm, the resistance of the carbon track can be estimated to be around 12.8 kΩ, which results in a small *iR* drop of a few millivolts.

As expected, cyclic voltammetry at high scan rates (500 mV/s, not shown) gave a peak–shaped response, typical of planar diffusion. The latter result confirms that a good seal is obtained between the carbon track and the PE–PET films after either, laser ablation or mechanical polishing. Despite the UV–photoablation exposure approach yielded probes with a slightly better electrochemical response, polished probes were mainly used in the following experiments, as they are easier to fabricate.

5.3.2. ***Approach curve characterisation***

Approach curves obtained as depicted in Figure 5.3b–c were performed in 2.0 mM $FcCH_2OH$ either over an insulating (glass) or a conductive (gold film) sample. Figure 5.5a shows representative experimental curves. In all the experiments, the soft stylus probe was held at E_T = 0.3 V to oxidize $FcCH_2OH$ under diffusion–controlled conditions. An unbiased gold film was used to drive the diffusion–controlled reduction of $FcCH_2OH^+$. Positive and negative feedback curves were observed when the soft stylus probe was approached to the gold film and the insulating glass, respectively (Figure 5.5a). The substrate position was determined as the inflection point of the probe approach

curves. At this point, the insulating part of the probe mechanically touches the surface, but the substrate–electrode distance d still has a finite value. If the probe is pressed against the substrate, it bends. In this way after contact, d does not vary linearly with the movement of the mechanical positioning system. For this reason, it is defined h_A as the height of the attachment point of the soft stylus probe with respect to the sample surface (Figure 5.5c), which varies linearly with the z position of the positioning system. If l_T is the length of the probe in the unbent state, the substrate–electrode distance d that is always positive differs from the quantity $h_P = h_A - l_T$ that can assume negative values when the probe is pressed against the substrate.

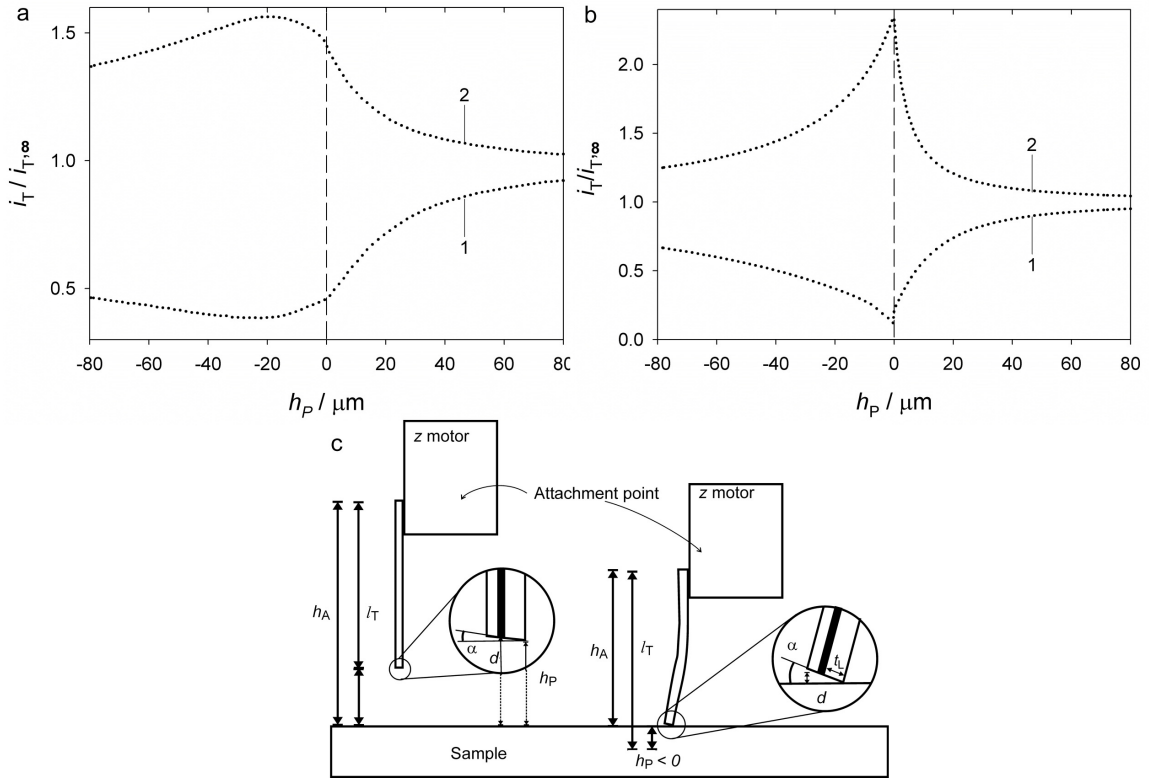

Figure 5.5. a) Experimental approach curves with a polished soft stylus probe over insulating glass (1) and unbiased gold electrode (2). E_T = 0.30 V, translation rate 0.5 μm/s. b) Simulated approach curve for a soft stylus probe, details in the supporting information, c) schematic representation of the SECM contact mode and the working distance for unbent and bent soft stylus probes.

The situation is shown in Figure 5.5c. After contact, the polished front end of the probe forms an angle α to the sample surface that increases upon further bending of the probe. Since the polymeric film thickness (t_L) that is between the active electrode area and the outer edge of the probe is equal to 85 µm, the difference $d - h_P$ is 85 µm sin(α). d always remains positive if the soft stylus probes cannot penetrate the sample. At the inflection point of the curve shown in Figure 5.5a, the current (i_T) over gold is about 1.45 $i_{T,\infty}$ and over glass 0.47 $i_{T,\infty}$ with $i_{T,\infty}$ = 10.1 nA. A photographic sequence (results not shown) was taken in order to determine the probe tilt and contact angles α before and after the electrode contacted the substrate (due to the bending). According to this photographic sequence, the soft stylus probe was tilted of about 3° before touching the substrate. Therefore, at the probe–surface contact point corresponding to the inflexion point in the approach curve, the distance d is equal to 4.5 µm. For small negative values of h_p the current continues slightly to increase in positive feedback and decrease in negative feedback as the probe is squashed against the substrate before a clear bending mode is established.

The electrode geometry produced by the present methodology is close to a crescent moon shape. As a consequence, quantitative analyses are difficult since no analytical approximations are available for the description of the i_T–d–relationship of such probes in SECM feedback experiments. BEM simulations that are particular useful to carry out three–dimensional simulation of unsymmetric, steady–state problems were used.[46, 139, 170-172] The electrode geometry for the simulation was taken from microphotographs and slightly idealized. The angle of the polished end of the soft stylus probe (480 µm × 200 µm) and the surface of the sample was assumed as 3°. A sample surface of 1600 µm ×

1600 µm was used. Together this geometry is represented by 4966 triangles for simulations with conducting samples and 11493 triangles for simulations with insulating samples. Detailed representations of the meshes used are shown in Figure 5.6. The simulated approach curves are shown in Figure 5.5b. The extends of hindered diffusion is well described by the simulation. However, it shows that in the contact mode, the current does not change too much if protruding insulating areas are encountered on the sample. For the positive feedback, the agreement for the unbent probe is also very high.

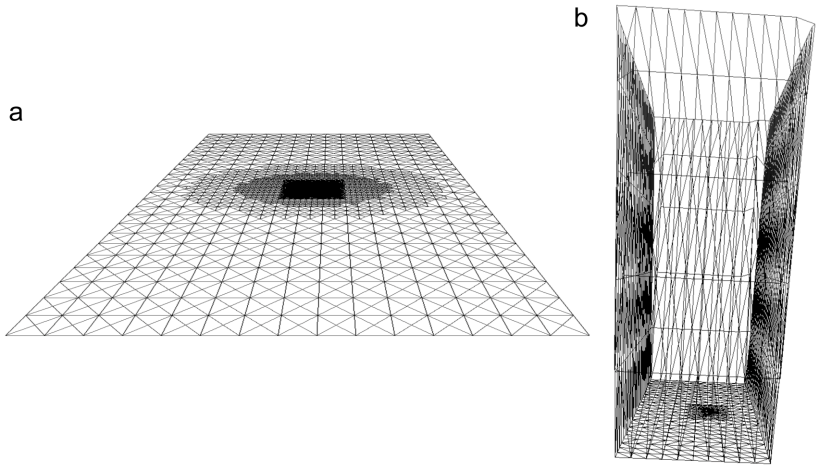

Figure 5.6. a) Used grid for the substrates corresponding to 1600 µm × 1600 µm. The size of the elements is reduced under the active electrode area. The total number of elements is 3484 (conducting sample) and 7725 (insulating sample). b) Grid of the lower part of the soft stylus probe with a height equal to 520 µm. The polished cross section corresponds to 480 µm × 200 µm. The electrode body and the active area is represented by 1482 triangles (conducting sample) or 3768 triangles (insulating sample).

However, for slightly bended probes, the theory predicts normalized feedback currents $I_T = i_T/i_{T\infty} = 2.2$, whereas currents of $I_T = 1.5$ were found experimentally. It could be expected that this current difference originated from a decrease of the local potential at the sharp crescent ends of the electrode, due to a higher ohmic drop produce by the higher current density at this zone. However, no current changes were observed when different supporting electrolyte concentrations (*i.e.* in the range from 0.05 M to 0.2 M) were used in the different experiments. Additionally, in the experimental curves the positive

feedback increases after the touching point and hindered diffusion becomes more effective. This is most likely due to an elastic deformation at the end of the soft probes that decreases *d*. No deformation of the probe has been considered in the BEM simulation.

5.3.3. ***Contact mode scanning over flat surfaces***

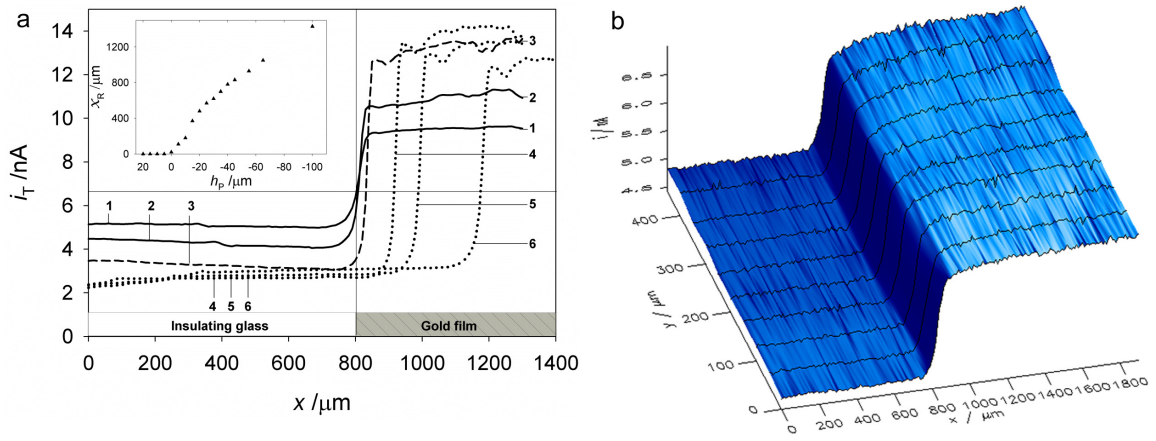

Figure 5.7. a) Lateral SECM line scans in feedback mode with a soft stylus probe prepared by laser ablation over a glass partially covered by gold in 2.0 mM $FcCH_2OH$, 0.1 M KNO_3. $i_{T,\infty}$ = 6.65 nA and the gold film position (x = 820 µm) are shown by thin solid lines; E_T = 0.25 V, step size = 20 µm and translation rate v_T = 20 µm/s. Designation of the lines: 1) contactless h_P = 20 µm; 2) contactless h_P = 5 µm; 3) to 6) contact mode with the following probe positions h_P 3) 0 µm; 4) –5 µm; 5) –10 µm and 6) –15 µm. Inset: registration shift x_R as a function of h_P. b) SECM image in contact mode of a partially gold–covered glass obtained by using a soft stylus probe prepared by mechanical polishing. Imaging conditions: working solution 2.1 mM $FcCH_2OH$, 0.1 M KNO_3, h_P = –75 µm, E_T = 0.3 V, step size in x and y direction was 10 µm and 50 µm, respectively. Translation rate v_T = 10 µm/s. The substrate was tilted about 10 µm along the x–axis.

Figure 5.7 shows a series of line scans in a solution of 2.0 mM $FcCH_2OH$ as mediator over a glass–gold boundary with the probe either moving freely above the substrate as in a classical SECM measurement (lines 1&2, $h_p > 0$) or pressed against the substrate in a bent contact mode (lines 3–6, $h_p \leq 0$). The scans were performed at scanning speeds of 10 or 20 µm/s. A classical behaviour is observed in the contactless mode with a negative feedback effect over the glass and a positive feedback over the unbiased gold (lines 1&2, $h_p > 0$). As soon as the probe touches the substrate (line 3, h_p=0), both the current over the

glass and over the metal reach their minimum and maximum values respectively. As can be seen, as the value h_p becomes more negative, the bending of the probe causes a shift of the horizontal registration x_R that is plotted as an inset.

Figure 5.7b shows a series of line scans performed in the bent contact mode and the corresponding SECM image of a partially gold–covered glass slide. Between each scan, the probe was lifted off the sample and returned to the original horizontal position where it was pressed against the substrate to the same bending degree (h_P = –75 µm). This procedure was repeated several times to cover an area of 450 µm × 1900 µm. The sharp boundary line obtained shows that the registration shift remains constant for the different scans. Although the sample was tilted with a difference of height of 10 µm over the scan length of 1900 µm, the current recorded is constant over the different areas. This clearly illustrates the advantages of a soft stylus probe approach to image the reactivity of surfaces with topographic artifacts. Indeed, samples with a tilt height up to 90 µm along a distance of 1500 µm can be scanned without any problem (see Figure 5.8).

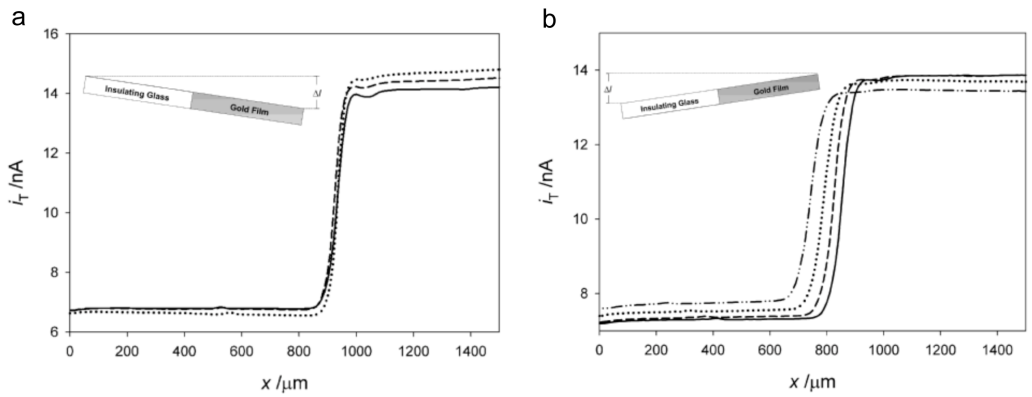

Figure 5.8. Lateral SECM line scans in feedback mode with a polished soft stylus probe over a glass partially covered by gold in 2.4 mM $FcCH_2OH$, 0.1 M KNO_3. The sample was tilted from the glass towards the gold region a) downhill b) uphill. The height difference (Δl) between the starting (over glass) and final (over gold) points was varied; 20 µm (continuous line), 30 µm (dashed line), 50 µm (dotted line) and 90 µm (dashed–dotted line). E_T = 0.3 V, step size = 10 µm and v_T = 10 µm/s, h_P = –75 µm.

Under the conditions tested (*i.e.* $\Delta l \leq 90$ µm for a scan length ≥ 1500 µm), the probe can tolerate height differences $\Delta l \leq h_P$ (Figure 5.8). If the probe scans uphill, the increased bending of the probe increased the distance between the active electrode and the sample. This causes a decrease of the contrast between signals over insulating region and conducting regions (Figure 5.8).

In order to determine the influence of the probe bending on the image resolution, the parameter given by equation 5.2 was calculated, as reported previously:[173]

$$\Delta x = \frac{\Delta i_T}{\left(\frac{\partial i_T}{\partial x}\right)_{x=x_{inflection}}} \tag{5.2}$$

Δx represents the required lateral distance to fully differentiate a conducting from an insulating area, while Δi_T is the difference between the probe currents above pure conducting and insulating materials. The gradient $\partial i_T/\partial x$ is obtained by numerical differentiation of a line scan, and it reaches a maximum over the boundary line. The Δx values obtained for an average of eight line scans at $h_P = -5$ µm (not shown) and $h_P = -75$ µm (shown in Figure 5.7b) were 49 µm and 64 µm, respectively. A similar analysis performed in contactless mode (d = 10 µm) under otherwise identical conditions produced a value of Δx = 32 µm. This difference may result from an increase of the electrode–substrate distance d (the longer this distance, the poorer the resolution) and also from the asymmetry of the diffusion field in the contact mode compared to the contactless measurements. Indeed, simulations made for inclined AFM–SECM probes have shown similar results, where the tilted surface creates a shielding effect on the redox mediator diffusion.[174] Nevertheless, Davoodi *et al.* showed that there are several

advantages for SECM imaging with inclined probes, especially for the mapping of neighboring active sites.[174]

A long–term goal of this work is to image large areas (~ cm^2) as for example complete human fingerprints. Within this scope, a minimum distance in the range of ~50 µm for fully differentiating one active region from a non–active one is acceptable. However, there is room for improving the resolution of the images by producing probes with smaller track cross–sections and thinner PET covers to decrease the working distance. For that not only the active area but also the *RG* value is important, since the latter does not only determine the diffusional shielding but also the working distance between the active electrode area of the probe and the sample. Both features have an impact on the resolution and can also be controlled by variation of the polishing process.

5.3.4. ***Contact mode scanning over 3D patterns***

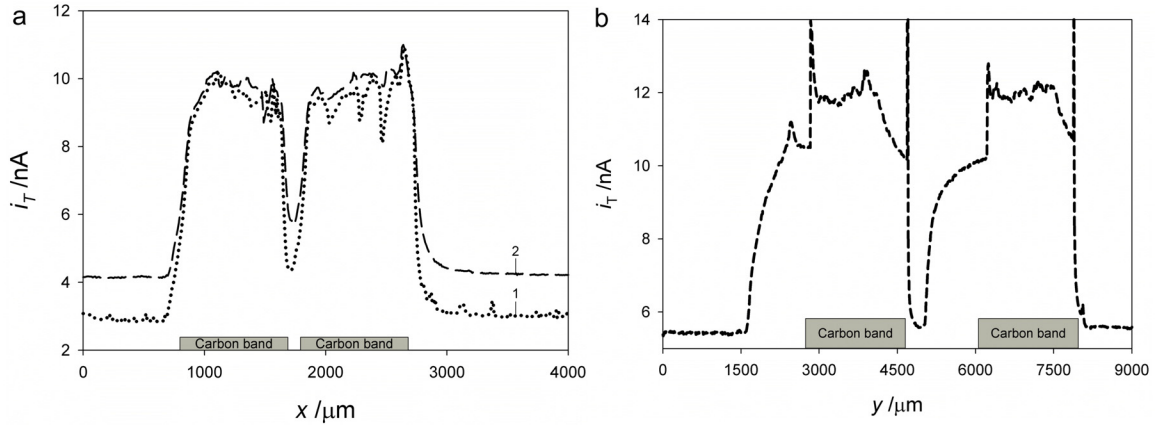

Figure 5.9. Lateral SECM line scans in feedback mode above a pair of unbiased carbon bands separated by a gap of 100 µm (a) or 1500 µm (b) and with a height above the surrounding matrix of 7.1 µm (a) or 118 µm (b) with a polished soft stylus probe in contactless (dotted line (a)) and contact mode (dashed lines (a) and (b)). A scheme of the topography profile obtained with a contact profilometer in air is presented at the bottom of each figure. SECM conditions: h_P = –75 µm (a) or –60 µm (b), E_T = 0.3 V, step size = 10 µm, translation rate v_T = 10 µm/s, working solution 0.1 M KNO_3 and 2.1 mM $FcCH_2OH$ (a) or 2.4 mM $FcCH_2OH$ (b).

The imaging of rough surfaces by SECM in the contact mode was also studied. This is important since other scanning probe techniques, like AFM and AFM–SECM, cannot

scan surfaces with topographical differences higher than ~10 μm and are also limited in the lateral range. To assess the ability of the soft stylus probe for this kind of application, several line scans over screen–printed carbon bands separated by 100 μm or 1500 μm and presenting thicknesses of 7 μm (Figure 5.9a) or 118 μm (Figure 5.9b) were respectively performed. Figure 5.8a shows the line scans in contactless (line 1) and contact mode (line 2) after compensation of the registration shift. Both modes yield the same band width, which is larger than that obtained with a profilometer (see scheme at the bottom of Figure 5.9a). In addition, when working in contact mode a decrease on the current contrast is produced due to the higher *d* achieved.

Figure 5.9b shows line scans in contact mode over the thick carbon electrodes (118 μm–thick, see scheme at the bottom of Figure 5.9b). It has to be realized that the contactless mode cannot be used over patterns with such a large aspect ratio without a feedback distance regulation system. Before starting the SECM line scans in contact mode, the probe was approached to the insulating glass until the desired value of h_P was reached. Once the scan was initiated, low current values were observed due to the blocking effect of the redox mediator diffusion over the glass substrate. Afterwards, a current increase was observed, as the probe gets closer to (but not over) the first carbon band. This is a consequence of the physical contact that is established between the carbon band edge and the probe, lifting it off from the insulating substrate and leading to a current increase associated both to a lowering of the negative feedback process and perhaps to positive feedback with the edge of the carbon track. At the edge of the carbon electrode, it is interesting that a current peak can be observed as the probe passes over the boundary. Indeed at that point both the top surface and the edge contribute to the positive

feedback. As the probe approaches the end of the substrate, the positive feedback current decreases slowly and then another sharp transition occurs when the probe jumps to the substrate level. It is likely that electrical contacts between the carbon bands on the sample and the carbon track of the probe are established at y = 4600 μm and y = 8000 μm. This is concluded from the very sharp decrease of the current upon minimal lateral offset of the sample (compare the decay of the peaks at y = 4600 μm with that at y = 2700 μm). Nevertheless, Figure 5.9b illustrates the major advantage of soft stylus probe over classical SECM probe that cannot provide any information for surfaces with such aspect ratios.

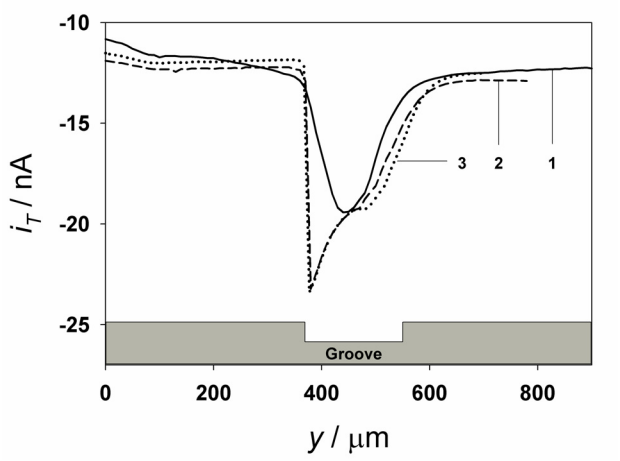

Figure 5.10. Horizontal SECM line scans in feedback mode over a PET film with an open microchannel (150 μm width) in 1.9 mM $K_3[Fe(CN)_6]$ and 0.2 M KCl. The microchannel position is shown by the scheme at the bottom of the Figure. Scanning conditions: 1) h_P = 5 μm (continuous line); 2) h_P = –1 μm (dashed line) and 3) h_P = –10 μm (dotted line). E_T = –0.1 V. Step size = 50 μm, translation rate v_T = 50 μm/s.

Finally, a groove (150 μm width, 40 μm depth) fabricated into a PET substrate was topographically characterized using a soft stylus probe exposed by mechanical polishing and $[Fe(CN)_6]^{3-}$ as mediator. Figure 5.10 shows horizontal line scans at different h_P values after correction of the registration shift. Line scans performed in contactless (line 1, h_P = 5 μm) and contact modes (lines 2&3, h_P = –1 μm and –10 μm) show higher

cathodic currents when the soft stylus probe was over the microchannel due to the less effective shielding of the mediator diffusion. In contact mode, the first groove edge causes an abrupt change of current as the probe snaps into the channel with undepleted mediator concentration. At the other side of the channel, the stylus probe is gradually more bended and only after some distance from the groove rim the same hindered diffusion is observed as just before entering the channel. The slowly rising current before the high carbon band, and the slowly decreasing current after the groove should produce images with a shadow as in photography with an object illumination coming at an angle.

5.4. Conclusions

The results presented above show that the proposed microfabrication methods can be used to produce soft stylus probes for SECM that can operate in contactless and more especially in contact mode over large tilted substrates with patterns of high aspect ratios. This contact mode has been developed to scan large areas such as electrophoresis gels, fingerprints or libraries for material testing avoiding problems with sample tilt and limited translation rates in constant distance mode with an electronic distance regulation. Soft stylus probes are very stable and can be used many times, since the electrode surface can be regenerated by gentle polishing. In addition, probe stiffness can be tuned (*e.g.* by adjusting the overall width and tapering of the probe) to prevent that the probe penetrates the sample. By extension of the imaging software routines, it is planned to image automatically surfaces of high roughness such as the samples used in Figure 5.9.

6. FOUNTAIN PEN FOR SCANNING ELECTROCHEMICAL MICROSCOPY*

6.1. Introduction

In order to extract with SECM reliable information from low volume systems, different constraints have to be considered. On the one hand, the electrochemical cell has to be contained within a microscopic volume, which requires not only the use of small electrodes (*i.e.* working, reference and counter electrodes), but also a special arrangement of a miniaturized electrochemical cell in such a way that electrode collision does not occur upon scanning. On the other hand, considering that solute concentrations in low volume systems can vary drastically upon solvent evaporation, experimental artifacts may arise and surface modifications have to be minimized (*e.g.* to avoid precipitation processes).

Integrated three[175] or two[176, 177] electrode cells have been introduced to simplify the electrochemical cell design, to impede collisions between electrodes and to allow an

* Based on Cortés–Salazar, F., Lesch, A., Momotenko, D., Busnel, J–M., Wittstock, G., Girault, H.H., Fountain Pen for SECM. Analytical Methods, 2010. DOI: 10.1039/C1030AY00096E.

easier positioning of the electrochemical cell. The scanning droplet cell introduced by Lohrengel *et al.* is based on a three–electrode cell setup, where a capillary containing the reference and counter electrode delivers an electrolyte droplet on a conductive surface. The working electrode is thus defined by the wetted area.[175] Despite common potentiostatic techniques can be employed with this setup for surface activity studies, it is restricted to the study of conductive substrates. Spaine *et al.* reported a positionable microcell supported in a theta glass capillary.[176] The working electrode located at one of the channels was composed of a carbon fiber sealed with epoxy, while a Ag/AgCl wire was positioned as the reference electrode at the other compartment within a concentrated solution of NaCl. This device was completed by a salt bridge at the bottom of the pulled glass capillary, which allows the electrical connection and a physical separation between the reference electrode and the analyte solution. Both voltammetric and SECM measurements were performed successfully at subnanolitre volumes. In spite of that, the preparation of this dual probe is cumbersome and a high expertise is required. Additionally, the mechanical stability of the probe is easily compromised by any probe–substrate crash. Another procedure for preparing integrated two electrode microcells was recently introduced by Turcu *et al.* where a common glass–encapsulated microelectrode was chemically coated with an Ag film and used as reference electrode.[177] The main advantage of this dual system is the simplicity of the device and its preparation method. Steady–state voltammetry and SECM images of Pt bands in a nanolitre droplet were obtained as a proof–of–concept of the functionality of the proposed dual system. In order to decrease the influence of solution evaporation on the SECM imaging, Turcu *et al.* covered a nanolitre droplet of the redox mediator solution with a layer of paraffin oil, but

with adsorption of this oil onto the microelectrode only between 3 to 4 % of the initial current changes were observed after 50 minutes of continuous scanning on a Pt band microarray. With the purpose of avoiding any contamination, special attention has to be paid to the positioning of the redox mediator droplet, the microelectrode and then the covering mineral oil layer. The latter obliges the use of a physical barrier that precludes the paraffin leakage, limiting at the same time the scanned area. The use of a humidity chamber to provide a controlled water–saturated atmosphere or the addition of glycerin to the supporting electrolyte have been also employed with the purpose of decreasing the effect of evaporation on microsystems.[176, 178-181] Recently, Juncker *et al.* introduces a multipurpose microfluidic probe (MFP) which result from the coupling of microfluidics and scanning probes.[182] The MFP is based on two apertures placed at the bottom of the device from where solution is injected and aspirated, creating a locally microfluidic flow that covers the sample surface. Taking advantage of microfluidic probes, evaporation problems could be overcome by flowing constantly solution to the gap in between the probe and the sample surface. A similar concept has been already applied in atomic force microscopy (AFM) for surface patterning, where a fluidic channel is introduced into the AFM cantilever, allowing the fluid transport from a reservoir to the end of the cantilever.[183-186]

The present work introduces a fountain pen probe for SECM, fabricated by ablating two parallel and aligned microchannels on opposite sides of a polyethylene terephthalate (PET) sheet. One of the microchannels is filled with carbon ink before coating and the carbon track tip is used as working electrode, while the other is covered by lamination and is used for flowing solution to the tip. An integrated two–electrode cell is completed

by a third microchannel filled with Ag/AgCl ink and that is in physical contact with the solution flowing through the microchannel. This new probe is based on the same preparation method of the recently developed soft stylus probe,[57] but introduces a fluidic microchannel and a counter/reference electrode (CE/RE) that may extend the scope of SECM to the scanning of dry surfaces in a contact regime. As a proof–of–concept a gold on glass EPFL logo was imaged by using the fountain pen probe in scanning contact regime.

6.2. Experimental section

6.2.1. ***Chemicals***

Ferrocene methanol ($FcCH_2OH$, ≥ 97 %, Sigma–Aldrich) and KNO_3 (≥ 99 %, Buchs, Switzerland) were used as received. Deionized water was produced by a Milli–Q plus 185 model from Millipore (Zug, Switzerland). Fountain pen probes were produced using 100 μm thick polyethylene terephthalate films, Melinex (PET, Dupont, Wilmington, DE, USA) and 50 μm polyethylene/polyethylene terephthalate (PE/PET, Payne, Wildmere Road, Banbury, England) lamination foils. Laser–machined tracks in PET were filled by Electrador carbon ink (Electra Polymer & Chemicals Ltd., Roughway Mill, Dunk Green, England) for the working electrode and by Ag/AgCl ink (ERCON, Wareham, MA, USA) for the CE/RE electrode.

6.2.2. ***Preparation of a gold micro EPFL logo on glass***

Glass slides were treated with piranha solution and cleaned by sequential sonication in ethanol, acetone and purified water followed by drying under a stream of Argon. A gold EPFL logo, 100 nm thick, was prepared in an Edwards Auto 306 evaporator operating at

a pressure less than $5 \cdot 10^{-6}$ mbar. A metallic mask defined the EPFL logo pattern (1000 x 1400 μm). The film growth was initiated by the thermal evaporation of a 1 nm thick chromium (99.99 %, Balzers) layer at < 0.1 nm/s in order to enhance the adhesion of the Au layer. Gold (99.99 %, Balzers) was subsequently evaporated at < 0.1 nm/s up to 5 nm, before increasing the deposition rate to 0.2 – 0.3 nm/s for the deposition of a 100 nm layer. An optical picture of the EPFL logo pattern was obtained by using a scanning laser microscope (VK 8700, Keyence).

6.2.3. ***SECM measurements***

SECM measurements were carried out using a custom–built SECM setup running under SECMx software[68] and comprising an IVIUM compactstat (IVIUM Technologies, The Netherlands) operating in a classical three–electrode mode or under bipotentiostatic conditions. Data analyses were carried out using MIRA software.[69] The electrochemical cell comprises Ag/AgCl as CE/RE and a carbon track as working electrode. All potentials are reported with respect to the Ag/AgCl electrode. After polishing, the quality of the electrode was checked with a Laborlux D optical microscope (Leitz, Germany). All the samples were mounted on the bottom of a flat cell construction and investigated at room temperature (20 ± 2 °C).

For using the new probe in the contact regime, the probe was mounted with a slight tilt with respect to the sample surface thanks to the tapering and the stiffness of the probe. When the probe was pressed against the sample the polymeric probe bends in a way that the cross–section of the carbon track is closer to the sample than the opening of the microfluidic channel (inset of Figure 6.4a). In order to enable imaging, a new routine was included in the SECMx software that allows examining a surface in contact and contact–

less regime during the forward and the backward scanning, respectively. During the forward scan the probe is pressed against the sample, bent, and dragged over it. This is possible without damaging the studied surface, if the sample material is harder than the PET sheet from which the probe was made. After completion of the forward scan, the probe is lift off the sample surface by a preset stroke height so that the probe is freely suspended. It is then moved horizontally back to the start position of the line scan followed by an incremental step in the low frequency scan direction. The probe is brought again into mechanical contact with the sample by a vertical translation equal to the negative value of the stroke height and the next line scan in the contact mode commences. Images are constructed from the data acquisition of forward line scans in contact mode. By doing this, the probe bending degree and bending direction are always the same within one image frame when scanning in contact regime.

6.2.4. ***Fountain pen probe preparation***

Three microchannels were prepared into a polyethylene terephthalate (PET) film by laser ablation through a metallic mask using a 193 nm ArF excimer laser beam (Lambda Physik, Göttingen, Germany, fluence = 0.2 J, frequency = 50 Hz) as reported in previous works.[57, 187, 188] The width, depth and length of the prepared microchannels were 35 µm, 40 µm and 6.5 cm for the open microchannel, 15 µm, 20 µm and 4 cm for the working electrode (WE) and 35 µm, 40 µm and 2 cm for the CE/RE. The open microchannel and the one dedicated as WE were aligned at each side of the PET film, while the open microchannel and the one used as CE/RE were perpendicularly connected over the same PET face (Figure 6.1). Carbon and Ag/AgCl inks were applied (manually with a spatula) to create conductive tracks for the WE and CE/RE, respectively. After curing the

conductive tracks at 80 °C for 1 h, one PE/PET film lamination was applied over the electrode and one underneath. A reservoir was glued at one of the extremities of the open microchannel to allow the connection with an external pumping syringe system (KD Scientific). A cross section of the microchannel was then exposed by mechanical cutting and polishing by successively finer diamond lapping discs (Ultra–prep, Buehler, Schlieren, Switzerland) with different particle sizes of 30 μm, 6 μm, and 0.1 μm using a custom–built polishing machine. In order to avoid the blocking of the fluidic microchannel during the polishing process, it was first filled by capillarity with a saturated KCl solution that was left to crystallize. Then, the electrode was polished and finally submerged in water for 4 hours until the KCl was totally dissolved and the electrode was ready to use.

6.3. Results and discussion

Figure 6.1a shows a schematic representation of the fountain pen probe prepared by the method presented above. As it can be seen the fountain pen probe integrates a two electrode system, where the electrical connection between the WE and the CE/RE is made by the solution that is flowing through the open microchannel. From Figure 6.1b it is possible to see the good parallel alignment between the open microchannel (thickness = 35 μm, width = 40 μm) and the microelectrode (thickness = 20 μm, width = 15 μm). The microchannel prepared for the working electrode is almost completely filled with carbon ink. The working electrode has a trapezoid–like shape defined by the cross–section of the prepared microchannel, which can be easily reproduced.

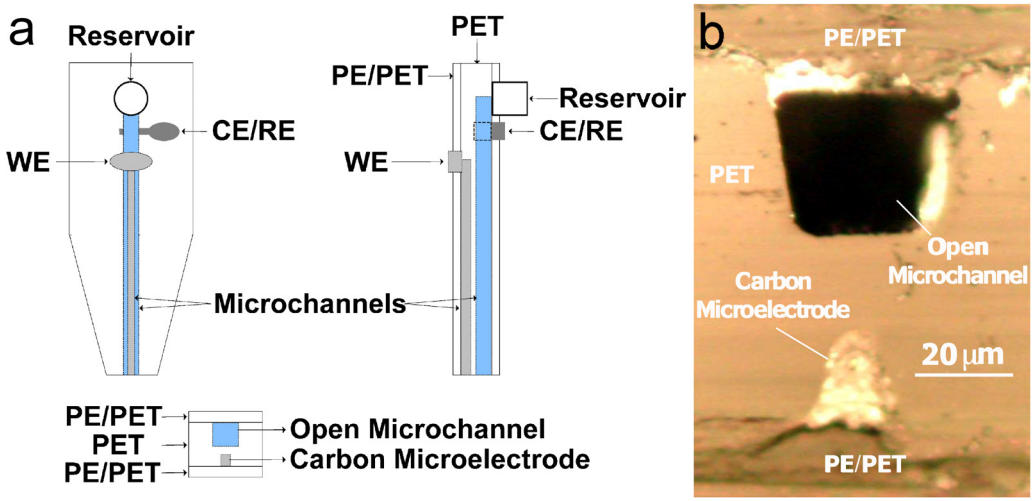

Figure 6.1. a) Schematic representation of the fountain pen probe used as working electrode for SECM; b) optical image of the carbon electrode exposed by mechanical polishing.

The electrochemical characterization of the fountain pen probes was performed by cyclic voltammetry, approach curves and horizontal line scans over conductive and insulating substrates. Before each experiment, an aqueous solution of $FcCH_2OH$ in KNO_3 was allowed to flow out until a drop of the solution covered completely the tip of the electrode and made a physical contact with the substrate (see Figure 6.2a and inset in Figure 6.3a).

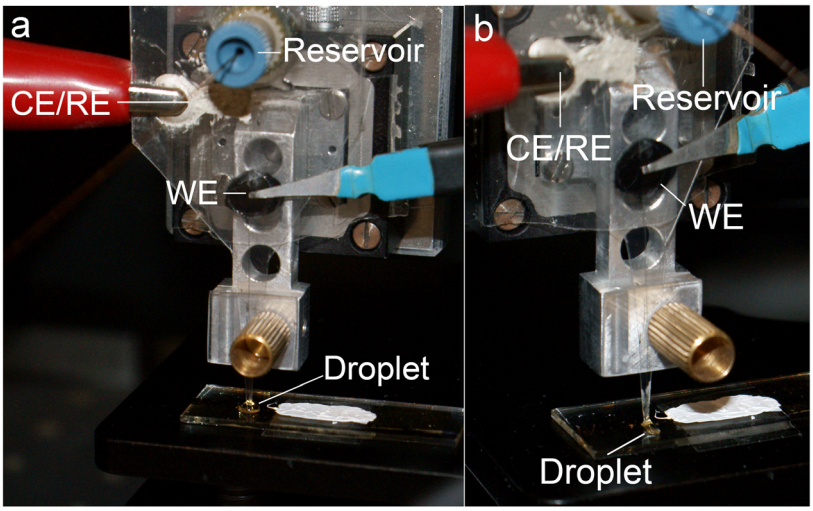

Figure 6.2. Photographs of the fountain pen probe working in a) pointillist and b) scanning mode.

Figure 6.3a presents the cyclic voltammogram of $FcCH_2OH$ at a fountain pen probe at a flow rate of 25 µL/h and 0 µL/h. Since the electrode was placed around 500 µm above the sample, a steady–state bulk situation can be assumed. The steady–state currents obtained for both cases results from the pseudo–hemispherical diffusion present at the microelectrode. Despite the very low charging current observed, the slope of the rising part of the curve is lower than expected for a reversible redox couple due to a high ohmic drop between the CE/RE and the WE. This can be overcome by increasing the concentration of the supporting electrolyte, increasing the area of the CE/RE electrode and by reducing the actual separation distance between these two electrodes (*i.e.* 4 cm). According to Figure 6.3a, the flow rate has little influence on the cyclic voltammetry when the electrode is located far away from the substrate, the small increase observed at 25 µL/h being most likely due to an enhanced mass transport.

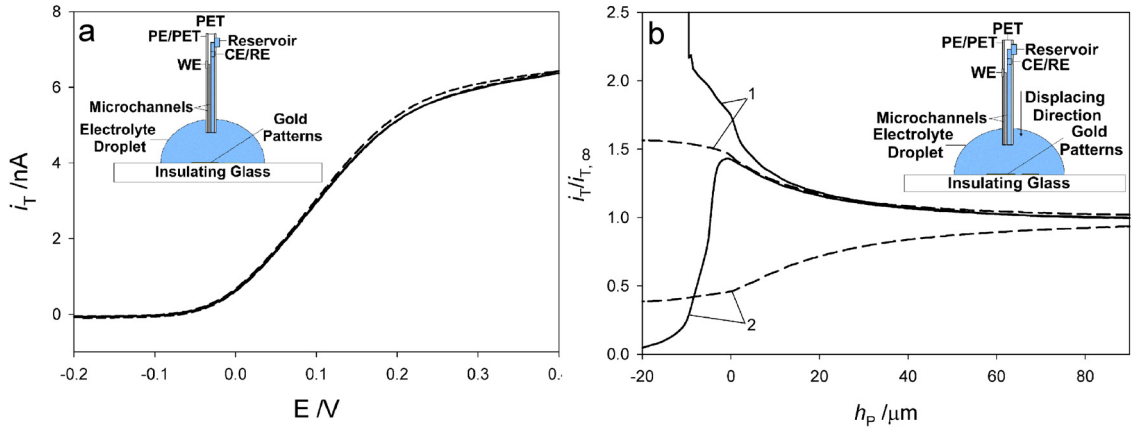

Figure 6.3. a) Cyclic voltammetry at a fountain pen probe in 3.14 mM $FcCH_2OH$ and 0.1 M KNO_3 at a flow rate of 25 µL/h (dashed lines) and 0 µL/h (continuous line). Scan rate 10 mV/s. b) Experimental approach curve of a fountain pen probe (continuous line) and a soft stylus probe (dashed line) over unbiased gold electrode (1) and insulating glass (2). E_T = 0.40 V, translation rate = 0.5 µm/s and flow rate = 25 µL/h. The insets in Figure 6.3a and 6.3b show the conditions in which the experiments were performed.

Approach curves at a flow rate equal to 25 µL/h over an insulating glass and a conductive gold film were performed resulting in the curves shown in Figure 6.3b (continuous lines),

and compared qualitatively to approach curves (dashed lines) obtained in the same conditions, but using the carbon working electrode immersed classically in the electrolyte above the substrate. The latter case corresponds to the recently developed soft stylus probe.[57] As expected a decrease of the current is recorded when the soft stylus probe is approached to an insulating substrate, while a current increase is observed when it is approached towards a conductive surface. In contrast, the fountain pen probe gives a continuous increase of the current profile in approach curves both, over glass or over gold. This is due to the fact that the blocking of the redox mediator diffusion is counterbalanced by the solution flux out of the microfluidic channel. Moreover, it has to be taking into account that the lateral flux to the electrode surface will become faster as the probe is located closer to the surface. As a consequence, an enhanced positive feedback behavior is observed. When the soft stylus probe touches the substrate surface, the probe is bended and the current changes as a function of the bending. It should be noted that the probe–sample distance change starts to differ distinctly from the vertical position change of the positioning system when the electrode physically touches the substrate. For this reason, the distance measured from the surface to the lowest point of the fountain pen ($h_P = h_A - l_T$) was defined as the difference between the height of the attachment point of the fountain pen with respect to the sample surface (h_A) and the length of the probe in the unbent state (l_T). When the probe is pressed against the surface a tilt angle (α) between the sample surface and the probe will be established. Thus d is completely defined by $d = h_P + t_L \cdot \sin(\alpha)$, where t_L is the thickness of the polymeric film that is between the sample surface and the carbon electrode (see Figure 5.4c in chapter 5).[57] When the fountain pen probe is closer to the insulating glass, a more efficient

blocking of the redox mediator diffusion is achieved. As a result, the redox mediator flux that is coming from the open microchannel is overcome and a decrease on the current is observed until the probe starts to be bended and the current does not depend anymore strongly on the vertical position of the positioning system. Conversely, an increase on the current takes place when the fountain pen probe is approached to the gold film as expected from positive feedback in conventional SECM setups. It should be noted that the fountain pen can cause a positive feedback although the sample potential is not externally controlled. This can be expected if the area on the sample wetted by the electrolyte is substantially larger than the active electrode area of the fountain pen probe. In this situation a concentration cell can be established between the sample areas in the vicinity of the probe and more distant wetted regions on the conducting sample regions.[72] The fact that the fountain pen probe presents a stronger positive and negative feedback than the soft stylus probe[57] is explained by a more parallel alignment between the active electrode area and the substrate.

From Figure 6.3b, it can be observed that for detecting of surface activity, the fountain pen probe must be used in a contact regime, where the highest current contrast is achieved. This is confirmed by performing lateral line scans over a glass–gold boundary at different h_p values (Figure 6.4a, all the scans were aligned according to the observed position of the glass–gold boundary). When the probe is at 10 µm from the substrate, no current difference is observed between the insulating and the conductive substrates. At h_P equal to –10 µm and –20 µm, a current contrast between the insulating and conductive regions is observed as the blocking of the redox mediator diffusion or its recycling can not be shielded by the flowing solution. It is expected that the fountain pen probe is not

limited to work in contact regime, since it might be also employed in a contact–less regime for micro–structuring and patterning of dry surfaces. In contrast to the bulk–like situation (see Figure 6.3a), the flow rate has an important effect on the steady–state currents, when the probe is in close contact with the otherwise dry substrate (Figure 6.4). When the probe is approached to a conductive substrate, a slightly higher current increase is observed for lower flow rates (Figure 6.4b). The latter might be explained by a lower dilution factor of the redox mediator concentration when lower flow rates are employed. In contrast, when approaching the probe to an insulating substrate, lower currents are recorded as lower flow rates are employed. This phenomenon is a consequence of a faster depletion on the redox species concentration, when less species are delivered to the gap in between the probe and the sample surface. Therefore, higher current contrast between active and non–active surfaces should be obtained when scanning with the fountain pen probe at lower flow rates, as it is confirmed in Figure 6.4c. Figure 6.4c shows several lateral line scans over a glass–gold boundary with a fountain pen probe working in contact regime (h_P = –20 µm) for three different flow rates. Despite a better current contrast with a flow rate of 5 µL/h, evaporation processes started to become crucial, since microchannel blocking by electrolyte precipitation took place. Flow rates values higher than 25 µL/h showed delamination of the PE/PET covering films due to the higher pressure required to achieve this flow rate. For this reason, flow rates between 15 to 25 µL/h are suggested as appropriate flow rates for SECM imaging with the fountain pen.

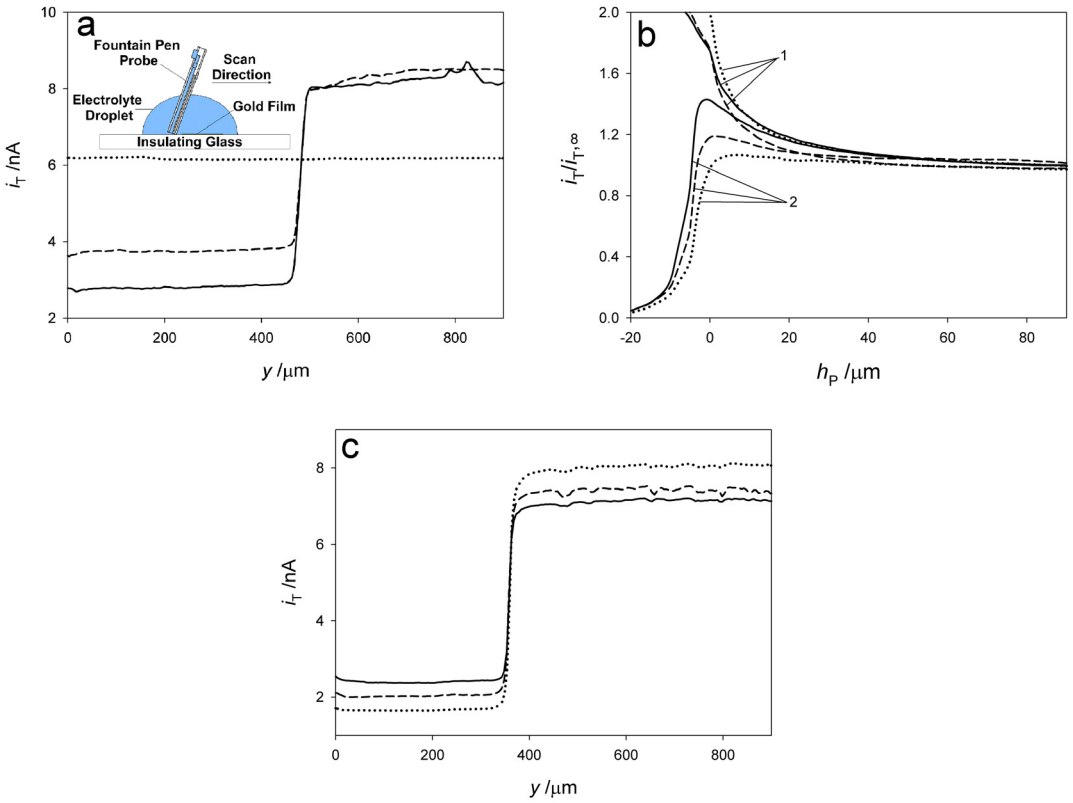

Figure 6.4. a) Lateral SECM line scans in feedback mode with a polished fountain pen probe over a glass partially covered by gold at a h_P value of 10 µm (pointed line), –10 µm (dashed line) and –20 µm (continuous line). E_T = 0.4 V, flow rate = 25 µL/h, step size = 5 µm and translation rate v_T = 25 µm/s. 2.1 mM $FcCH_2OH$ with 0.1 M KNO_3. b) Experimental approach curves of a fountain pen probe over unbiased gold electrode (1) and insulating glass (2) at a flow rate of 25 µL/h (continuous line), 15 µL/h (dashed line) and 5 µL/h (pointed line). E_T = 0.4 V, translation rate 0.5 µm/s. 2.1 mM $FcCH_2OH$ with 0.1 M KNO_3. c) Lateral SECM line scans in feedback mode with a fountain pen probe over a glass partially covered by gold at a flow rate of 25 µL/h (continuous line), 15 µL/h (dashed line) and 5 µL/h (pointed line). h_P = –20 µm, E_T = 0.4 V, step size = 5 µm and translation rate v_T = 25 µm/s. 2.5 mM $FcCH_2OH$ with 0.1 M KNO_3. The inset in Figure 6.4a shows the orientation of the probe during forward scanning.

It is important to recall that evaporation processes are a major issue when working in microvolumes systems. To avoid this major drawback, the use of a humidity chamber, the addition of glycerin to the supporting electrolyte and the covering of the aqueous microsystem with a mineral oil, have been proposed.[176-181] A different approach can be proposed by using the fountain pen probe, since evaporation processes could be partially counterbalanced by the constant flow of solution from the open microchannel. With the aim of assessing this possibility, an EPFL logo prepared by evaporation through a mask

was imaged under dry conditions by using a fountain pen probe in a contact regime (Figure 6.5). This image was build by using a new routine included in the SECMx software, that allows to examine a surface in contact and contact–less regime during the forward and the backward scanning, respectively (see experimental part). The experimental time employed for this image was 2 hours and 15 minutes, during which no apparent changes of the recorded current due to evaporation process (*i.e.* drastically increase on the redox mediator concentration) were observed. The only problem arising from the evaporation of the supporting electrolyte is the deposited material on the sample that actually could affect the degree by which the fountain pen is bended. The latter is most likely the reason for the small shift of the recorded position of the letters "P", "F" and "L" in the bottom part of the image, as compared with the optical picture of EPFL logo taken after the SECM image was obtained from this sample (Figure 6.5b). Future work will be focused on the removal of the solution that is flowing out from the open microchannel using a push–pull system. Only small scratches on the gold film are observed in Figure 6.5b. They were most likely present on the sample before imaging and may come from handling the samples but not from the scanning movement because they are not parallel to the scanning movement and do not occur in a repetitive manner. This is not unexpected because the gold and other substrate materials are harder than the polymeric material employed for the preparation of the fountain pen probe. In Figure 6.5a, the EPFL logo can be clearly observed due to the recycling of the redox mediator obtained over the conductive gold film (positive feedback) and hindered diffusion of the redox mediator over the insulating areas (negative feedback). The SECM image of the EPFL logo shows the feasibility of applying the fountain pen probe to surface activity

characterization of dry surfaces. Additionally, the contact regime allows the fountain pen probe to study moderately tilted surfaces without observing any topographical artifacts, as the gold micro EPFL logo was mounted without any attempt of leveling the surface and a tilt would otherwise clearly visible on scan length of 1400 µm.

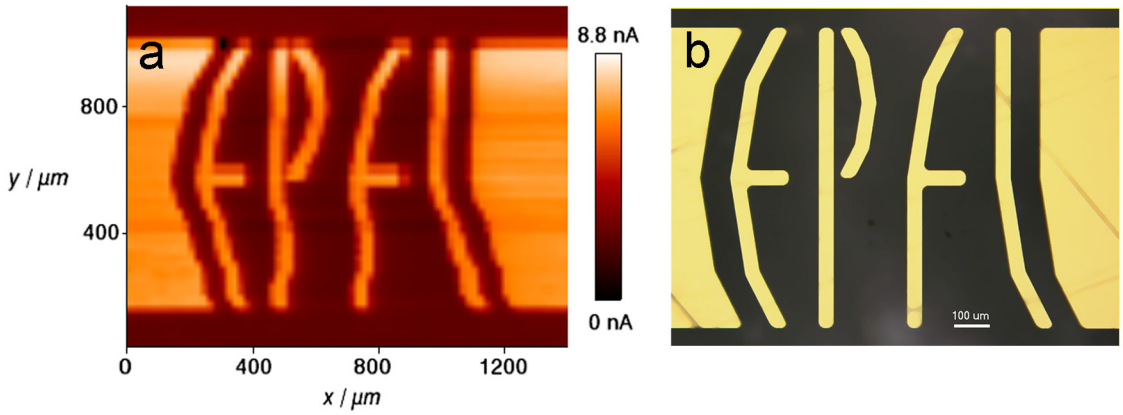

Figure 6.5. a) SECM image of a gold micro EPFL logo taken with a polished fountain pen in feedback mode. The fountain pen was lift off after each forward scan by a stroke height of 200 µm and placed back at the original vertical position of the scanning but shifted by 20 µm in *y* direction. h_P = 30 µm, E_T = 0.4 V, flow rate = 20 µL/h, step size = 20 µm and translation rate v_T = 20 µm/s. 2.6 mM $FcCH_2OH$ with 0.1 M KNO_3. b) Optical picture of the micro EPFL logo employed for this experiment.

6.4. Conclusions

The present work introduced the fabrication of a new fountain pen SECM probe that may extend the scope of SECM to the scanning of dry surfaces in a contact regime by delivering a nanolitre droplet at the bottom of the probe. Electrochemical experiments can be carried out over almost any surface. An optimum flow rate between 15 and 25 µL/h was obtained for spatially resolved surface activity characterization. Due to the stiffness of the fountain pen probe, an almost constant probe–substrate distance can be maintained when scanning in contact regime. As a proof–of–concept the fountain pen probes can be employed for surface activity detection as demonstrated by a feedback image of a gold on

glass pattern. Future experiments are being focused on the extension of this new probe to patterning and micro–structuring of dry surfaces.

7. SOFT MICROELECTRODE LINEAR ARRAY FOR SCANNING ELECTROCHEMICAL MICROSCOPY*

7.1. Introduction

Recently, SECM applications such as screening combinatorial catalyst libraries,[189-192] assessing the integrity of coatings,[36, 37, 193] reading–out electropherograms,[15] human fingerprints[39] or protein arrays[194, 195] call for larger scanning areas approaching the square centimeter. With current instrumentation, this poses a problem because the sample tilt must be minimized. While this might be possible for an experienced operator, curved samples are very difficult to deal with and imaging times become so long that artifacts arising from electrode fouling, supporting electrolyte evaporation or sample aging are introduced.

Usually three different strategies are followed to overcome such problems. The first strategy is based on the increment of the scanning rate and step size of the probe, in which case the image resolution is compromised. Scan rates up to 500 $\mu m \cdot s^{-1}$ and step sizes of 150 μm have been employed with this aim.[190, 196] However, Combellas *et al.*

* Based on Cortés–Salazar, F., Momotenko, D., Lesch, A., Wittstock, G., Girault, H.H., Soft Microelectrode Linear Array for SECM. Submitted to Analytical Chemistry. 2010.

showed that contribution to the measured current originated from convection cannot be neglected when scanning at rates higher than 10 μm·s^{-1}.[197] Indeed, at extreme fast scan rates (~ 1000 μm·s^{-1}) the capability for detecting surface reactivity is lost.[197] A second strategy employed to reduce problems arising from evaporation and electrode fouling is to image subregions of a large sample area with renewal of supporting electrolyte and/or electrode surface in between individual image frames.[190, 198] For instance, areas close to 2 cm^2 have been examined by SECM in order to screen combinatorial libraries for fuel cell electrode applications.[190] The third strategy is based on using multiple independent electrodes. Consequently, a large area is scanned in less time without compromising the image quality and avoiding the associated experimental problems outlined above. Such an approach has been largely followed in AFM imaging.[199-201]

Already in 1995, Meyer *et al.* had reported imaging experiments in the generation–collection mode using 400 individually addressable microelectrodes.[202] The imaging depended completely on the layout of the two dimensional electrode array and no displacement of the multiprobe was employed. Parallel arrays have been used in a SECM–like configuration in the context of the confined etchant layer technique.[203] Here the problem of diffusional interference at 2D array of electrode was overcome by a homogenous scavenger reaction and periodically lifting the tool electrode to renew the solution in the interelectrode gap. Recently, a multi–electrode probe for parallel SECM imaging has been presented by Barker *et al.* that comprised a linear array of 16 independent slightly recessed Pt 10 μm–diameter microelectrodes on a planar insulating chip.[51] For scanning purposes the bundle was kept in a fixed position while the sample was moved along the *x* and *y* axes. The array cannot be regenerated by mechanical

polishing because this would not only destroy the 200 nm thick nitride film that protects the leads of each individual electrode, but also the 130 nm thick Pt film.[51] Leïchle *et al.* used an electrically contacted cantilever with integrated microfluidics for localized copper deposition.[204]

An important issue when working with arrays is the cross–talk between electrodes, which could be avoided if the thickness of the diffusion layer of each microelectrode is smaller than half the distance between adjacent electrodes.[58] With this aim, Barker *et al.* employed an inter–electrode spacing equal to 120 μm for a 10 μm–diameter microelectrode that should be sufficient for avoiding diffusion layer overlapping. However, lower currents than expected were observed by cyclic voltammetry that could indicate an overlap of the diffusion layers of neighboring electrodes. The latter is most likely due to the fact the diffusional independence of microelectrodes in arrays is only valid for a finite time scale that depends on the distance between neighboring probes.[64, 205-209]

In the present chapter, a new concept using an array of individually addressable microelectrodes for SECM imaging based on the recent development of the microfabricated soft stylus probes is introduced.[57] Additionally, improvements related to the scanning in contact mode with an inclined probe coated by a thin Parylene film have been introduced. The soft nature of the electrode allows imaging while the probe is in mechanical contact with the sample. This defines a constant working distance for the electrodes sandwiched between two sheets of insulators similar to the SECM-AFM imaging where the working distance is defined by height of the AFM tip protruding from a sheath containing the microelectrode.[50] By exposing the microelectrode array on the

cross–section of a sheet structure, rather than on the surface of a chip–like overall shape, the problems of diffusional shielding is reduced and the contacting of the array elements is greatly simplified. Finite element method (FEM) simulations were performed in order to establish the effect of diffusion layer overlapping between neighboring electrodes on the respective approach curves. As a proof of concept for high–resolution imaging of large samples, a gold electrode structure on a glass chip and a full human fingerprint were imaged by a soft microelectrode array.

7.2. Experimental section

7.2.1. ***Chemicals***

Ferrocene methanol ($FcCH_2OH$, ≥ 97 %), bovine serum albumin (BSA) (≥ 90 %), benzoquinone (≥ 99.5 %), KCl and KNO_3 (≥ 99 %) were purchased from Sigma–Aldrich (Schnelldorf, Switzerland). Methanol and $K_3[Fe(CN)_6]$ (≥ 99 %) were purchased from Merck (Dietikon, Switzerland). All the chemicals were used as received. Deionized water was produced by a Milli–Q plus 185 model from Millipore (Zug, Switzerland).

7.2.2. ***Preparation of gold electrodes***

Glass slides were treated with piranha solution and cleaned by sequential sonication in ethanol, acetone and purified water followed by drying under a stream of Argon. **Caution:** *This mixture reacts violently with all organic material. Piranha solution has to be handled with extreme care to avoid personnel injury and property damage.* Gold films of 100 nm thickness were prepared in an Edwards Auto 306 evaporator operating at a pressure less than 5×10^{-6} mbar. The film growth was initiated by the thermal evaporation of a 1 nm thick chromium (99.99 %, Balzers) layer at < 0.1 nm/s as adhesion promoter.

Gold (99.99 %, Balzers) was subsequently evaporated at < 0.1 nm/s up to 5 nm, before increasing the deposition rate to 0.2 – 0.3 nm/s for the deposition of a 100 nm layer.

7.2.3. ***Finger printing on PVDF membranes***

The tagging of protein inked human fingerprints was prepared as described elsewhere.[39, 210] Briefly, the finger of a volunteer was soaked with a bovine serum albumin solution (1 g/L) for several seconds and then allowed to dry under a stream of nitrogen. Subsequently, the finger was pressed on a poly–vinyldifluoride membrane (PVDF, Bio–Rad, Hercules, CA, USA) pre–wetted in methanol and water. The PVDF membrane with the fingerprint was dried under a gentle nitrogen flux. For subsequent tagging, the whole membrane was submerged for 3 hours in an aqueous solution of 20 mM benzoquinone under constant shaking. The PVDF membrane was then washed extensively with water, dried, taped over a microscopic glass and finally scanned by SECM.

7.2.4. ***Soft microelectrodes array preparation***

Eight microchannels were prepared into a 100 µm thick polyethylene terephthalate (PET, Melinex® Dupont, Wilmington, DE, USA) film by laser ablation through a metallic mask using a 193 nm ArF excimer laser beam (Lambda Physik, Göttingen, Germany, fluence = 0.2 J, frequency = 50 Hz) as reported in previous papers.[57, 187, 188, 211] The average width, depth and length of the prepared microchannels were 20 µm, 30 µm and 5 cm. The electrode–to–electrode distances employed for the prepared arrays were equal to 130 µm, 250 µm or 500 µm. Laser–machined tracks in PET were filled manually with a spatula by Electrador carbon ink (Electra Polymer & Chemicals Ltd., Roughway Mill, Dunk Green, England) to create conductive tracks for the working electrodes. After

curing at 80 °C for 1 h, a 2 – 5 μm thick Parylene C film was deposited over the electrodes by using a Parylene deposition system (Comelec SA, La Chaux–de–Fonds, Switzerland). A cross–section of the microchannels was then exposed by laser ablation, cutting with a surgical scalpel (No. 10 made in sterile stainless steel, Swan–Morton, Sheffield, England) or mechanical polishing by using a custom–built polishing machine with successively finer diamond lapping discs of different particles sizes 30 μm, 6 μm, and 0.1 μm (Ultra–prep, Buehler, Schlieren, Switzerland). The quality of the electrodes was checked with a Laborlux D optical microscope (Leitz, Germany) and a scanning laser microscope (VK 8700, Keyence).

7.2.5. ***SECM measurements***

SECM measurements were carried out using a custom–built SECM setup running under SECMx software[68] and comprising an IVIUM compactstat (IVIUM Technologies, The Netherlands) operating in a three–electrode mode. The potentiostat was complemented by the WE32 unit (IVIUM Technologies, The Netherlands) that allowed the operation of 32 individually addressable working electrodes against a common counter (Pt wire) and reference electrode (Ag wire as quasi–reference electrode, QRE). All potentials are reported with respect to the Ag–QRE. The interdigitated gold electrode array to be imaged was used as an unbiased substrate. All the samples were mounted on the bottom of a flat cell construction and investigated at room temperature (20 ± 2 °C).

For using the new probe in the contact regime, the probe was mounted with a predefined angle of 70° with respect to the sample surface using a custom–built SECM holder. As a result, both probe bending degree and direction were preset before scanning in contact regime. In order to achieve small working distances, the probe was mounted

such that the 5 µm thick Parylene coating faced the sample surface. For discussing the image routine we distinguish the high frequency axis (*i.e.* the horizontal direction in which individual line scans are performed). The term "high frequency" stands for the fact that the forth and back movement of the probe along this dimension is faster than in the other lateral dimension (*i.e.* the low frequency direction) in which an incremental movement is performed after each forward and reverse line scan along the high-frequency axis. A new routine was included in the SECMx software that allows dragging the inclined probe in the forward line scan of the high-frequency axis but lifting the probe in the reverse scan by a preset stroke height so that the probe is freely suspended. After returning to the start position along the high-frequency axis, the probe is moved horizontally along the low-frequency axis. The probe is brought again into mechanical contact with the sample by a vertical translation equal to the negative value of the stroke height and the next line scan in the contact mode commences. By doing this, the probe bending degree and bending direction are kept constant within one image frame when scanning in contact regime. Images are constructed from the data acquisition of forward line scans in contact mode using MIRA software.[69]

7.2.6. ***Simulations***

Simulations with the microelectrode arrays were performed with the software package COMSOL multiphysics (version 3.5a), which employs the finite element method (FEM) for the numerical resolution of differential equations. All the simulations were performed on a Linux Ubuntu 8.04 platform with a four Core 2.66 GHz CPU and 7.8 GB of RAM.

7.3. Results and discussion

7.3.1. ***Probe characterisation***

A top view of the soft microelectrode array (Figure 7.1a) shows eight carbon tracks with an electrode–to–electrode distance equal to 500 μm. Each electrode leads to a contact pad located in the left part of Figure 7.1a that allows addressing the electrodes individually. Before use, a cross–section of the covered carbon tracks were exposed by laser ablation or blade cutting followed in some cases by mechanical polishing with fine diamond lapping discs. A cross–section defines an array of 8 carbon microelectrodes and is presented in Figure 7.1b (130 μm electrode–to–electrode distance), where the successful filling and closing of the microchannel can be seen. Cutting was performed by laser–ablation. The need of using an UV–laser in order to obtain a fresh surface limits its applicability in daily laboratory routines. Figure 7.1c shows the cross–section of an array of 8 microelectrodes (500 μm electrode–to–electrode distance) obtained by cutting with a surgical scalpel. Although the surface is not as smooth as the laser–ablated surfaces, this process does not affect the active electrode area or the Parylene coating.

The electrochemical behavior of each microelectrode in the arrays was tested individually by cyclic voltammetry in 2 mM $FcCH_2OH$ (Figure 7.2). All the cyclic voltammetries obtained were normalized by the respective steady–state current recorded at the solution bulk ($i_{T,\infty}$). As reported in a previous communication,[57] cutting by laser ablation produces very smooth PET surfaces along with highly active carbon electrodes (Figure 7.2a). Carbon microelectrodes exposed by blade cutting also presented a sigmoidal response, but with higher capacitive currents (Figure 7.2b). Nevertheless, the

absolute steady–state currents recorded with the multiprobe exposed by cutting are similar compared to the ones obtained after laser ablation.

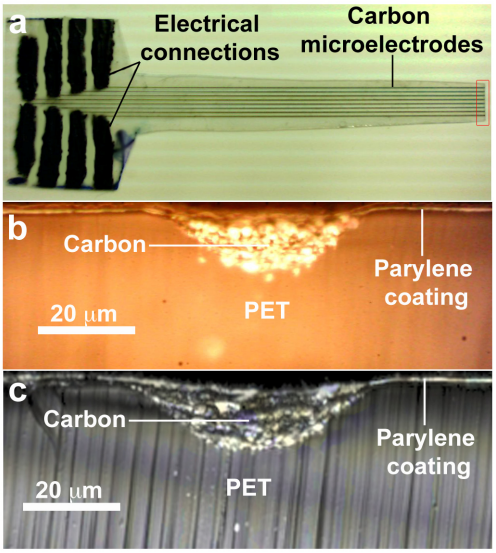

Figure 7.1. a) Optical image of a soft microelectrode array (500 µm electrode spacing) employed as working electrode for SECM experiments and cross–sections of an individual carbon microelectrode exposed by b) laser ablation (130 µm electrode spacing), and c) cutting with a surgical scalpel blade (500 µm electrode spacing).

Due to the microchannel filling processes, different active electrode areas in the array are obtained and as a consequence different diffusion–limited steady–state currents are recorded. For instance, the average of the absolute steady-state current for the array exposed by blade cutting (Figure 7.2b) was equal to 18.3 nA with a standard deviation of 0.8 nA. However, as observed in Figure 7.2, the diffusion–limited currents can be corrected by introducing a scale factor that normalizes all the current values of each individual electrode of the array (*vide infra*). The reproducibility on surface finishing obtained by blade cutting has been found to be adequate for the present imaging goals as shown later in Figure 7.8 and Figure 7.9.

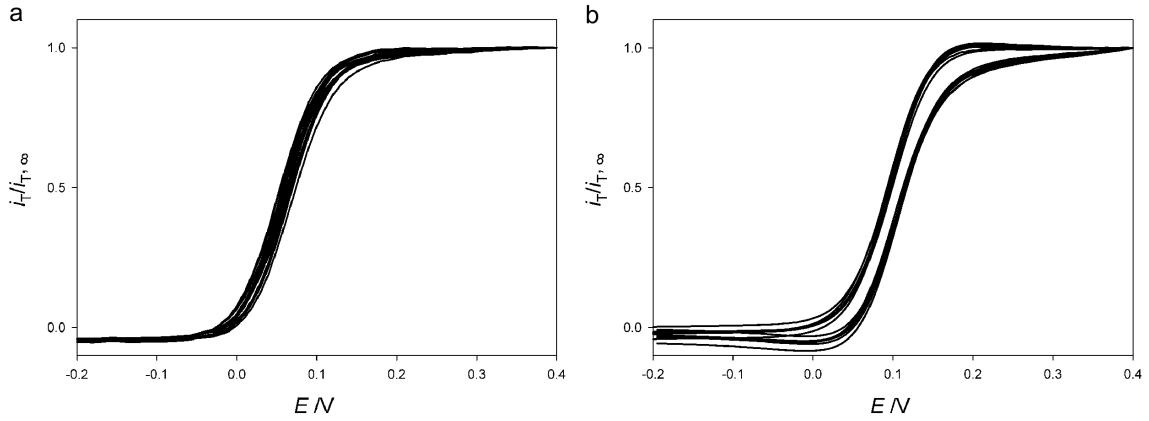

Figure 7.2. Normalized cyclic voltammograms of an array of eight microelectrodes exposed by a) laser ablation and b) cutting with surgical scalpel blade in 2 mM $FcCH_2OH$ and 0.1 M KNO_3. Each microelectrode was tested individually. Scan rate 20 mV/s.

In comparison to the recently developed soft stylus probes,[57] two improvements are introduced here for the fabrication of the array. The first one is related to the SECM holder that allows inclining the bundle by a predefined angle (β). By operating the probe at an angle (see Figure 7.3a) it is possible to control the degree and direction of the probe bending, and to reduce topographic artifacts coming from 3D patterns with heights higher than 100 μm. The angle β decreases the contrast in i_T (*i.e.* current difference between active and non-active regions), because at larger β, the mediator diffusion from the solution bulk is less effectively shielded by the inclined probe. In addition a larger *d* is established (see Figure 7.3b). A β angle of 70° was determined to be a good compromise between diminishing topographic artifacts and maintaining current contrast. The second improvement concerns the thin Parylene coating that replaces the previously used PE/PET lamination film. This thin film coating technique provides a 5 μm thick pinhole–free insulation and reduces the distance *d* defined as the distance from the center of the active electrode area to the outer edge of the probe and therefore guarantees that the electrode is in a very close proximity of the substrate (See Figure 7.4).

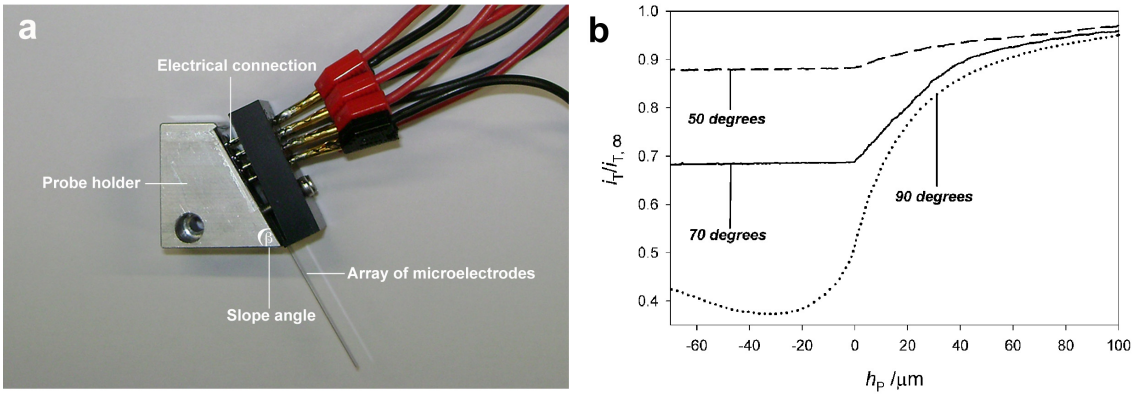

Figure 7.3. a) Photograph of the holder for the array probe with a predefined tilt. b) Approach curves over an insulating substrate in 2.1 mM $FcCH_2OH$, 0.1 M KNO_3. E_T =0.3 V Vs QRE, translation rate 0.5 μm/s. The different angles represent the angle between the sample surface and the probe defined as slope angle β in (a).

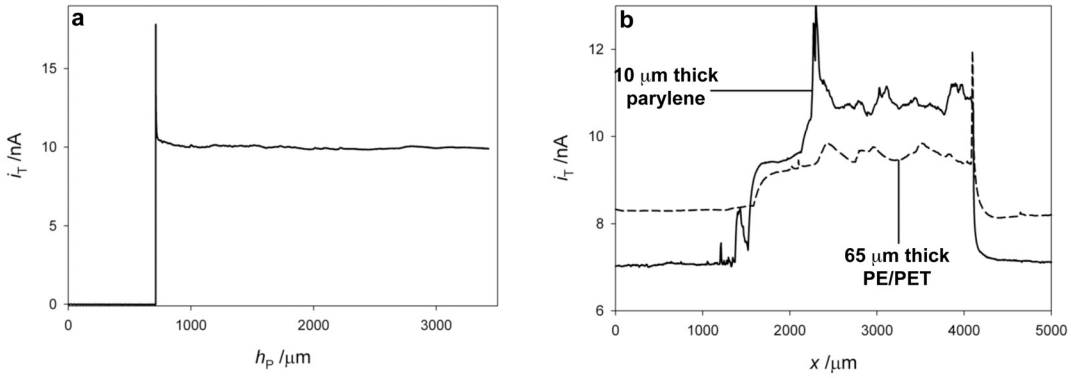

Figure 7.4. a) Experimental approach curve with a parylene coated soft stylus probe toward a solution of $FcCH_2OH$ 2.1 mM in KNO_3 0.1 M. b) Lateral SECM line scan with a soft stylus probe coated by a 10 μm thick parylene coating (continuous line) and a 65 μm thick polyethylene/polyethylene terephthalate lamination foil (dashed line). E_T = 0.3 V, step size = 5 μm, translation rate v_T = 10 μm/s. 2.1 mM $FcCH_2OH$.

Figure 7.4a shows the approach curve of the microelectrode array from air toward the air/solution interface. Upon contact the current rises and after decay of the capacitive current the current settles on a constant value coming from the electrolysis of 2.1 mM of $FcCH_2OH$ contained in the electrolyte. The current does not rise as the probe is further immersed into the electrolyte. This proves the good sealing of the carbon track by the parylene coating since pinholes or defects in this coating would lead to currents that would increase with continuous immersion. Figure 7.4b shows a line scans in contact

mode over a thick carbon electrode (118 µm thick) measured with two soft stylus probes with different thickness of the insulating cover of the carbon tracks. A higher current contrast is obtained when using parylene coating as a smaller effective working distance is achieved with the thinner coating.

7.3.2. ***Simulation of approach curves***

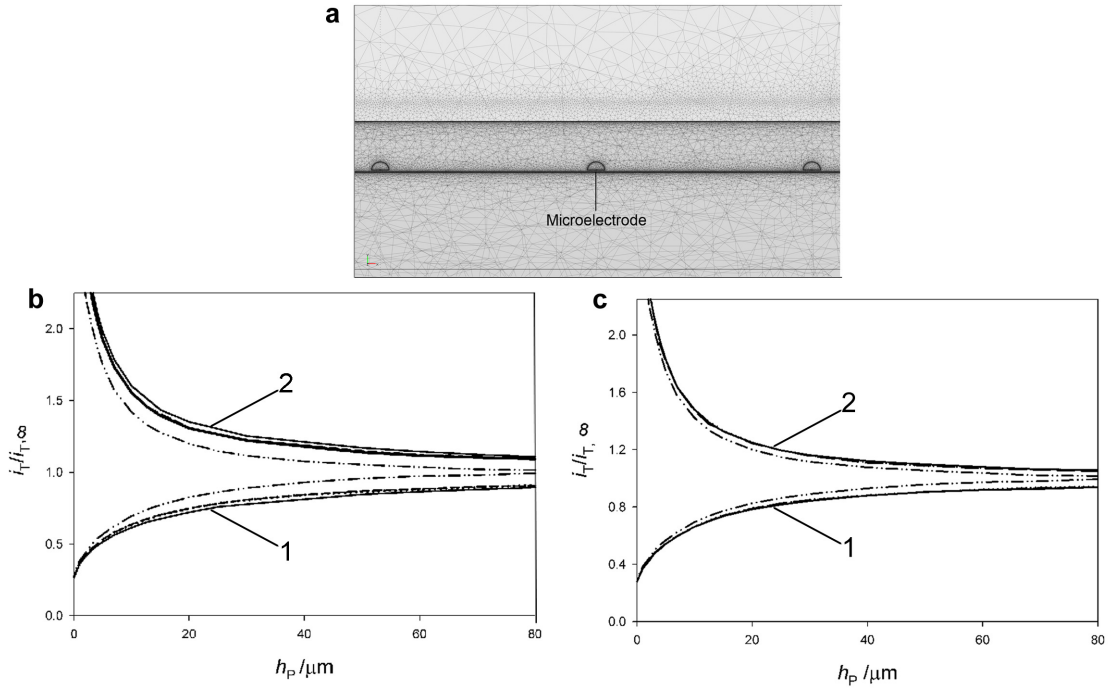

Figure 7.5. a) Shape and extension of the active electrode area considered for the FEM simulations. Simulated SECM feedback approach curves for an array with an inter–electrode distance equal to b) 130 µm or c) 500 µm over an insulating sample (1) and a conductive surface with mass transport–controlled mediator regeneration (2). Outer electrodes are depicted by dashed and dotted lines, while a continuous line represents the inner electrode. The dashed–dotted line corresponds to the calculated approach curve of a single microelectrode.

FEM simulations of two microelectrode arrays with different inter–electrode distances (*i.e.* 130 µm and 500 µm) were performed in order to establish the effect of the diffusion layer overlapping on the respective approach curves. An array of three microelectrodes was chosen for the simulations (Figure 7.5a), since it is the minimum number of microelectrodes that describes the effect on inner and outer electrodes in a linear array.

The model under investigation can be described by the diffusion equations for redox active species assuming steady–state conditions

$$\nabla(-D_i \nabla c_i) = 0 \tag{7.1}$$

where D_i and c_i are the diffusion coefficient and concentration of species *i,* respectively. The electrochemical response of the electrode can be depicted as the consequence of the following reaction at the probe

$$O + e^- \xrightarrow{k_1} R$$

and at the substrate

$$R - e^- \xrightarrow{k_2} O$$

where k_1 and k_2 represents the heterogeneous rate constants for the forward and backward reaction, respectively. The reaction rates can be defined by

$$v_{probe} = k_1 * c_o \tag{7.2}$$

$$v_{sub} = k_2 * (c_{bulk} - c_o) \tag{7.3}$$

v_{probe} and v_{sub} indicate the reaction rates at the electrode and at the substrate, while c_O and c_{bulk} are the local and bulk concentrations of species O. In this work steady–state conditions with $k_1 = k_2 = 10^6$ m s^{-1} are assumed. The diffusion coefficients for species O and R were set to 6.7×10^{-10} m^2 s^{-1}, which corresponds to diffusion coefficient of ferrocene methanol in water and c_{bulk} of O species was 2 mM. By applying the appropriate boundary conditions, the solution of the differential equations is the local concentration c_O. The probe current can be calculated by integrating the normal diffusive fluxes of species O at the electrode surface. The array body was simulated as a

parallelipiped with dimensions 125 μm × 2000 μm × 1000 μm which is placed in a box of 2000 μm × 3000 μm × 1000 μm. The bottom of the array was placed at least 1000 μm far away form the top and side planes of the box. The assumed electrode geometry of the soft microelectrode array is shown in Figure 7.5a. The active area of all the microelectrodes was approximated to a quarter–moon shaped (*i.e.* 20 μm depth and 40 μm width). The minimal mesh size was set to 0.8 μm at the edges of active surface area and the edges of the array. The microelectrode array was approached to the substrate presenting a take–off angle β equal to 70 degrees. 130 μm and 500 μm electrode–to–electrode distances were employed for assessing the effect of the diffusion layer overlapping on the SECM approach curves. The approach curves started at a probe–substrate distance of h_P = 100 μm and 20 further points were calculated until touching the substrate.

In order to plot the approach curves after touching of the sample, a new vertical coordinate h_p was defined. It is the difference $h_P = h_A - l_T$ between the height of the attachment point above the sample h_A and the vertical extension l_T of the unbent probe. Thus the effective working distance d in the contact mode is defined by

$$d = \begin{cases} d = h_P + t_L \sin(\alpha);\ (h_P \geq 0,\ \text{non} - \text{contact regime}) \\ d = t_L \sin(\alpha);\ (h_P < 0,\ \text{contact regime}) \end{cases} \tag{7.4}$$

where α is the angle between the cross–sectional plane of the probe and the sample surface and t_L is the thickness of the polymer film covering the carbon tracks. The geometry of the probes in contact and non–contact regime is shown in Figure 7.6.

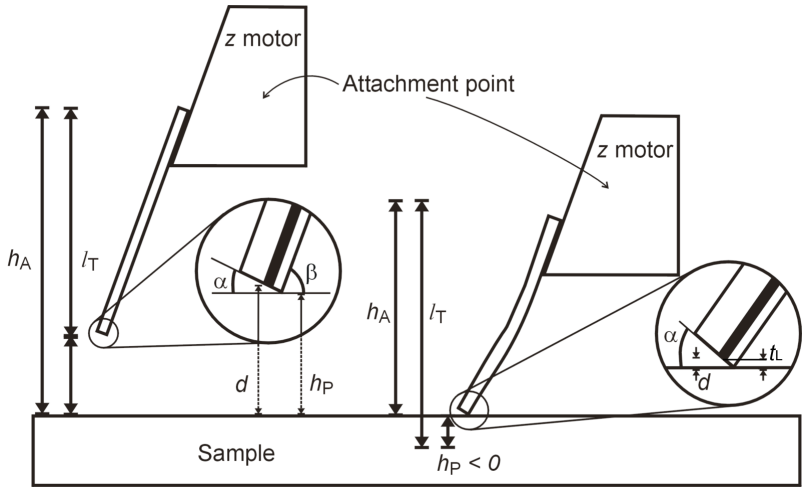

Figure 7.6. Schematic representation of the SECM contact mode and the working distance for unbent and bent soft array of microelectrodes.

Approach curves were simulated only for $h_p > 0$ because elastic deformation and sliding of the probe take place when the soft probe is pressed against the substrate that cannot be described by the current simulation setup.[57] Figure 7.5b shows the simulated approach curves of an array of three microelectrodes with an inter–electrode distance of 130 μm. The simulations predict both, positive and negative feedback responses. The deviation between the behavior of an individual electrode (dashed–dotted lines in Figure 7.5b) and electrodes within an array results from the diffusion layer overlapping of neighboring electrodes. The overlapping on the diffusion layers decreases the currents in the case of negative feedback, as a result of the redox mediator overconsumption produced by the neighboring electrodes. For positive feedback, a higher current is detected because each electrode is also benefiting from electrolysis at neighboring electrodes. Similar results have been obtained when working with heptode microelectrodes in disc generation–ring generation (DG–RG) mode, where overlapping of the diffusion layers among electrodes increased and decreased positive and negative feedback, respectively.[212]

It is important to notice that electrode cross–talk effect is more relevant for inner electrodes (continuous lines). But also the response of outer electrodes deviates (dashed and dotted lines) from the response of a single probe (dashed–dotted lines). According to Figure 7.5b, the highest difference in current–distance curves between outer and inner electrodes is 2.6 %. This should allow the use of these electrodes for qualitative SECM imaging in the feedback mode. Figure 7.5c shows the simulated approach curves performed with an array of three electrodes with an electrode–to–electrode separation of 500 μm. In contrast to the array with an electrode spacing equal to 130 μm, no clear difference is observed on the approach curves obtained for outer and inner electrodes. Moreover, in comparison to the approach curves calculated for a single microelectrode the highest difference when the probes are close to the substrate correspond to a 2.1 %. According to Figure 7.5c, a small diffusion layer overlapping takes place when using an array of microelectrodes with an electrode spacing ≥ 500 μm. It has to be pointed out that when approaching the substrate either for positive or negative feedback, the differences among all the electrodes diminishes probably as a result of the compression of the diffusion layer.

7.3.3. ***Approach curves characterization***

Experimental approach curves over insulating (glass) and conducting (gold film) substrates were performed in 2 mM $FcCH_2OH$ (Figure 7.7). The oxidation of $FcCH_2OH$ under diffusion–controlled conditions at all the microelectrodes was achieved by biasing the array at E_T = 0.3 V during all the experiments. As the array of microelectrodes was approached toward an insulating sample a decrease of the current was recorded due to the hindered $FcCH_2OH$ diffusion (negative feedback). In contrast, when the microelectrode

array was brought into a close contact with a conductive region, an increase on the current was observed as recycling of the redox mediator was achieved by the $FcCH_2OH^+$ reduction at the unbiased gold film (positive feedback). The driving force for the regeneration of $FcCH_2OH$ results from a concentration cell formed by the deviation of the $[FcCH_2OH]/[FcCH_2OH^+]$ under the microelectrodes from the corresponding values far away from the probe.[72] As a consequence, recycling of the redox mediator on unbiased conductive substrate is possible if the sampled area is larger than the size of the microelectrode.[72] For negative feedback, the normalized experimental current is close to the one obtained by simulation for $h_P \approx 0$. For approaching to a conducting surface the experimental current is slightly lower than predicted by simulation probably due to kinetic limitations at the carbon microelectrode and/or the unbiased gold substrate.

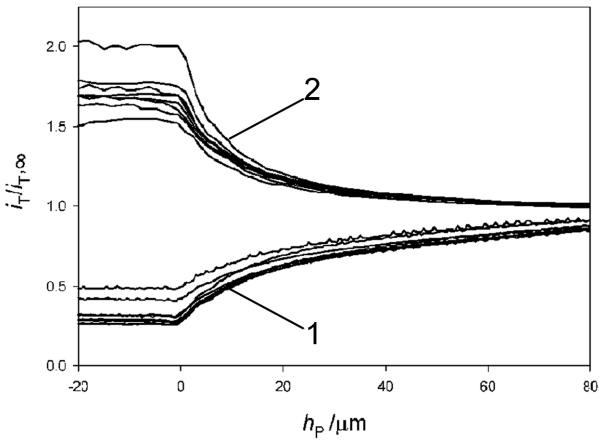

Figure 7.7. Experimental approach curves with an array of eight microelectrodes (130 μm inter–electrode spacing) over insulating glass (1) and unbiased gold electrode (2), in 2 mM $FcCH_2OH$ and 0.1 M KNO_3. E_T = 0.35 V, translation rate v_T = 0.5 μm/s.

After mechanically touching the substrate, the current assumes an almost constant value because the probe angle and bending and hence *d* is not drastically altered upon further movement of the vertical positioning system (Eq. 7.4). Figure 7.7 demonstrates the higher immunity against topographic artifacts of the new soft probes when compared to the

previously reported soft stylus probe, mainly due to the preset probe slope and the thin Parylene coating.[57] The approach curves in Figure 7.7 also show slightly varying currents at the point of mechanical contact most likely indicating small different probe–substrate distances among the microelectrodes contained in the array. This can for instance be caused by roughness at the cutting line and variation in the carbon track thickness.

7.3.4. ***High throughput SECM imaging***

SECM imaging in contact regime has been introduced elsewhere.[57, 211] The polymeric probe is pressed against the sample and dragged over the sample while brushing it. The main advantage of this mode is the possibility to scan at constant *d* over corrugated and tilted surfaces without artifacts and without the need of an instrumentally demanding electronic feedback system to keep *d* constant. Indeed, as the bended probe can adjust to the sample corrugation and tilt, the probe–substrate distance remains almost constant upon scanning. Consequently, sample leveling before SECM imaging is not needed, even for large area samples. Figure 7.8 shows a typical 3D SECM image of an interdigitated array of gold microelectrodes shown in Figure 7.8d and obtained with an array of eight carbon microelectrodes (250 µm inter–electrode distance). This test sample was chosen as it allows to detect easily eventual registration shift and represents at the same time an ideal specimen for proving the soft microelectrode array capacities for surface activity characterization at the micron resolution over a large area. The image in Figure 7.8b was constructed from the forward scans data recorded in contact mode. During the reverse scans the probe was lifted off 200 µm from the substrate and returned to the starting position with an increment on the low frequency axis (Figure 7.8a). Before the next forward scan starts, the probe was lowered by 200 µm to re–establish the mechanical

contact to the sample. In order to achieve large imaging the increments are 9 times performed by a 25 µm step to completely cover the area between the initial *y* positions of the microelectrodes. After that the electrode array is translated by 2000 µm to attach a complete new image directly adjacent to the first image. The schematic of this procedure is shown in Figure 7.8a.

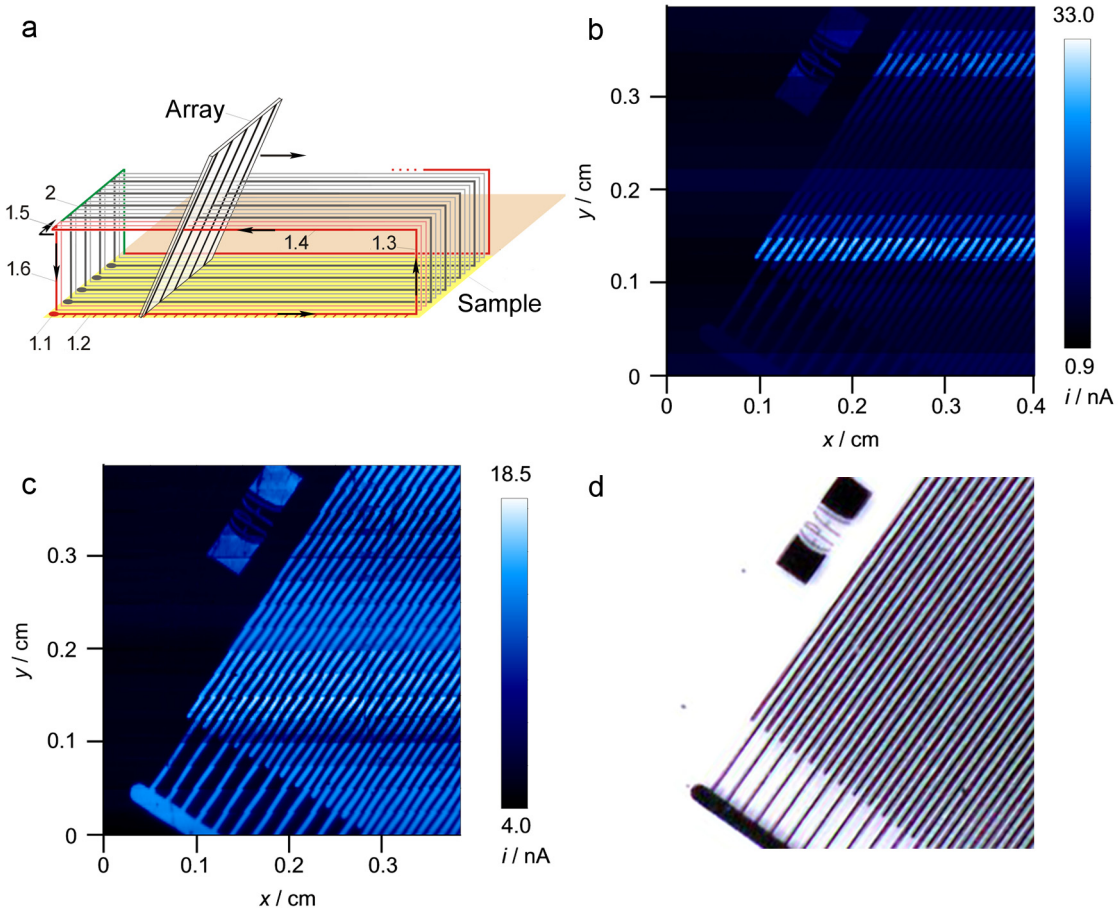

Figure 7.8. Principle of SECM imaging with a soft microelectrode array. (a) Schematic of the probe array movement (linear multiprobe with 5 sensors); 1 – line scan of the first sensor: 1.1 – starting point; 1.2 – forward scan of high frequency axis; 1.3 – lift off; 1.4 – reverse scan; 1.5 – step of standard size of low frequency axis; 1.6 – re–approach; 2 – large step of low frequency axis. Black arrows depict the probe scanning direction. b) SECM feedback image of a gold on glass microstructure with an array of 8 microelectrodes and an inter–electrode spacing of 250 µm. h_P = –60 µm, step size = 10 µm and translation rate v_T = 25 µm/s. 2 mM $FcCH_2OH$ with 0.1 M KCl. c) Image corrected for different sensitivities of the individual microelectrodes and positional offsets of the individual electrodes (details in the text). d) Optical picture of the micro EPFL logo employed for this experiment. Note: Figures 7.8a-c were kindly provided by Andreas Lesch from the University of Oldenburg.

Figure 7.8b shows the uncorrected image. The gold bands are clearly resolved, due to the current contrast originated from the negative and positive feedback achieved over the insulating glass and the unbiased gold bands, respectively. The gold band width and spacing in between gold patterns is equal to 50 µm that represents a very high resolution if one takes into account the dimension of the complete area scanned (0.4 cm × 0.4 cm). This was covered by a total of 401 data points in *x* direction and a total of 160 individual line scans performed by the eight microelectrodes and defining the point number in *y* direction. The time required for recording this image with the microelectrode array was around 3 hours 10 min, roughly eight times less than the expected time for imaging the same sample region by a single microelectrode and using the same experimental parameters. No particular alignment procedure of sample plane and *x*,*y*–plane of the positioning system was used.

Figure 7.8c shows the corrected image. The corrections include the adjustment of the lateral positions of each individual electrode of the array. While the spacing in *y* direction is well defined by the laser ablation process, the exact position in *x* directions is slightly different for each electrode due to the slight misalignment and the cutting procedure with a scalpel. These positional offsets are obvious from the offsets in the image of the straight gold lines in Figure 7.8b. For correcting the *x* position of each data point, an offset $x_{\mathrm{offs},i}$ of the particular electrode that acquired this data point was added to the *x* position of each point recorded by this electrode. The vector of the correction values is $\boldsymbol{x}_{\mathrm{offs}}$/ µm = {0; 5; 10; 15; 20; 25; 30; 35}. The resulting data set is not anymore an orthogonal grid with equal intervals within one horizontal dimension. In order to plot the image, the data were triangulated by the Delaunay triangulation implemented in the

interface description language (IDL) programming used to produce the image processing software MIRA. After establishing the triangulation with 64160 points and 381160 triangles, inner points were interpolated by bilinear interpolation. In addition the measured current values were corrected. First a current offset $i_{T,offset,i}$ was subtracted from each measured current value that reflects an offset between the channels of the microelectrodes, as observed in Figure 7.2b at the beginning of each cyclic voltammogram. Such offsets result from a combination of instrumental limitations in the WE32 unit. The different sizes of the individual microelectrode arrays were corrected by a dimensionless scale factor s_i for each microelectrode of the array. Thus the corrected current value is

$$i_T' = (i_T - i_{T,offset,i}) \times s_i \tag{7.5}$$

The used values are $\boldsymbol{i}_{T,offset}$ / nA = {3.2; 1.5; 0.4; –1.9; –4.0; –11.8; –4.8; 0.1} and **s** = {3.0; 4.0; 2.7;1.4; 1; 0.42; 0.72; 1.72}. The EPFL logo (gold on glass) is resolved as it can be compared with the optical picture of this sample shown in Figure 7.8d. While samples with regular and known patterns such as that in Figure 7.8 make it easy to select the suitable positional and current correction values, such regions for current and positional referencing can rather easily be incorporated into material libraries. Often an inert background can already serve as a reference point for either the current scaling or offset. However it should be pointed out that the array used for Figure 7.8 represents a rather extreme case of deviation in the response of individual electrodes. As shown in the next example, there are probes that do not require current or positional offset corrections at all.

An additional proof–of–concept is shown in Figure 7.9, where a complete human fingerprint was scanned by SECM for first time. The SECM imaging of this fingerprint is based on the detection of a protein–inked fingermark deposited on a PVDF membrane and tagged with benzoquinone.[210] The microelectrodes carried out the diffusion–controlled reduction of ferricyanide. At the sample areas tagged with benzoquinone, benzoquinone molecules are reduced and the oxidized mediator is regenerated.[210] The benzoquinone will then be regenerated by oxidation from dissolved dioxygen in the solution. Positive feedback will then be encountered when scanning protein–containing regions of the fingerprint, while negative feedback will be developed for protein–free PVDF zones.

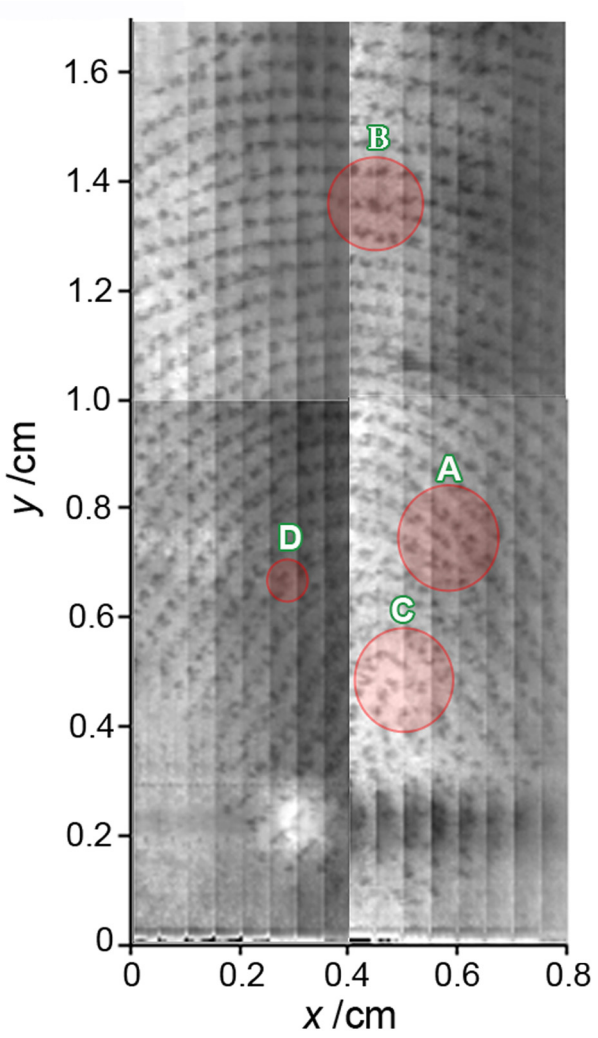

Figure 7.9. SECM feedback image of a human fingerprint developed by benzoquinone tagging with an array of eight microelectrodes of 500 µm interelectrode spacing. E_T = –0.35 V, h_P = –50 µm, step size = 50 µm and translation rate v_T = 50 µm/s (acquisition time = 5 hours 12 min). 2 mM $K_3[Fe(CN)_6]$ with 0.1 M KCl.

Human fingerprints are valuable tools for personal identity verification, since each individual fingerprint has unique features like the flow of the ridges (*i.e.* the overall pattern), the ridge path deviations (*e.g.* ridge endings and bifurcations marked in Figure 7.9 as zones A and B), and finally the intrinsic ridge characteristics (*e.g.* ridge shape and pores marked in Figure 7.9 as zones with letters C and D). Recently it has been shown that SECM provides forensic scientist a new tool for the visualization of human fingerprints on unusual surfaces (*e.g.* multicoloured backgrounds, body fluids or other

components contamination and porous surfaces) with high resolution and sensitivity.[12, 39, 213] However, the approximately 1–2 days would be required to image a full fingerprint with a single electrode. This excessively long–time has restricted the use of SECM for identification purposes. The fingerprint shown in Figure 7.9 was constructed from four different images taken in a total experimental time of 5 hours 12 min.

7.4. Conclusions

The present chapter illustrates the possibility of performing high throughput SECM imaging with a linear array of eight microelectrodes prepared by microfabrication techniques. Soft microelectrode arrays are intended to be used in contact regime avoiding topographic artifacts arising from corrugated or tilt substrates when scanning large sample areas. The surface of the active electrode area can be easily renewed by simple blade cutting, thanks to the mechanical stability of the polymeric materials employed for the probe preparation. As a consequence, the array of microelectrode is capable of being used several times and it could be implemented with minor changes in any conventional SECM setup. The arrangement of the electrode in a sheet–like body reduces the diffusional interference between them compared to the integration into a planar chip. A drastic reduction of imaging time was achieved for image frames with areas in the cm^2 range, while conserving the high sensitivity and resolution of SECM feedback images.

The successful imaging of an entire human fingerprint in a reasonable time provides more evidences that imaging with high resolution is possible in the contact regime. Furthermore, arrays with only eight microelectrodes have been developed so far. Current work is under development to further automate the probe fabrication and connecting to the potentiostat. With the current equipment 32 individual electrodes could be used in

parallel. This could be increased to 128 by extension with commercially available hardware components, resulting in a linear array able to cover in only one scan a 2.5 cm wide area with a 200 µm resolution (*i.e.* for a 200 µm electrode spacing). Imaging with an array of 32 probe electrodes measurements like that in Figure 7.9 could be recorded in about 1 hour. These perspectives offer further possibilities for scanning electrophoresis gels, thin layer chromatographic plates, material libraries, checking the integrity of corrosion protection coatings and so forth.

8. PERSPECTIVES AND ON GOING WORK

SECM is increasingly becoming a popular technique to study chemical surface reactivity, thanks to the well–developed theory and the recently overcome instrumental limitations. Additionally, the SECM versatility provide a tool that can be applied to a wide range of sample areas (*i.e.* nano–, micro– and macro–dimensions) and as demonstrated in chapter 3 is possible to couple to miniaturized electrophoresis for protein detection. By applying the microelectrode array concept to such microseparations, not only a fast separation method, but also a fast and sensitive protein detection technique could offer a high throughput tool for proteomic analysis. Moreover, Righetti *et al.*[214-216] reported recently a new protein separation technique namely "SDS–PAGE focusing electrophoresis". This technique allows the separation of proteins by molecular mass (*i.e.* mass to charge ratio) in a way that separated proteins are focused in a specific region, no matters the potential applied, similar to IEF electrophoresis. By performing a miniaturized two–dimensional PAGE electrophoresis (e.g. SDS–PAGE focusing with IEF), a high amount of information could be concentrated in a small area and can be read by the linear microelectrode array presented in this thesis. Moreover, with the protein detection method shown in chapter 4, a selective SECM detection of proteins with free cysteine

groups could be followed by a general detection of proteins after a second tagging process or by using the indirect detection method proposed in chapter 4. As a result, important structural information could be obtained, which simplify the protein identification process (see Figure 8.1).

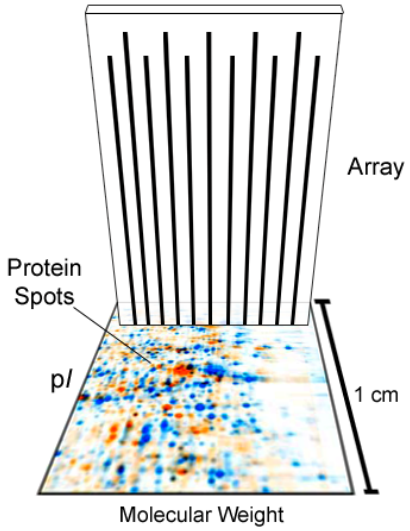

Figure 8.1. Schematic representation of the possible coupling of 2D PAGE (SDS–PAGE focusing and IEF) and SECM with a linear array of microelectrodes. The 2D-PAGE was taken from Berth *et al.*[217]

Scanning large sample areas is now becoming possible with the use of soft microelectrode arrays as SECM probes. Amperometry being a technique that can easily be multiplexed, hundreds or even thousands of microelectrodes could be used for imaging. Electrochemical scanners based on this concept will undoubtedly provide new tools for surface analysis and surface patterning in biological, nano– and micro–technology sciences. The application of the soft stylus probe concept should increase the use of SECM, as the simplicity of the method becomes one of the most obvious SECM features and specialized microelectrodes could be prepared easily by modifying the carbon ink with electrocatalysts such as Pt nanoparticles.

Combination of microfluidic systems with the microelectrode array in a multi–fountain pen array configuration could open new horizons for fast, simple and high resolution write and read–out scanning of almost any interface. For instance, multi–fountain pen scanners could be used in forensic sciences for human fingerprint imaging at the crime scene (see Figure 8.2).

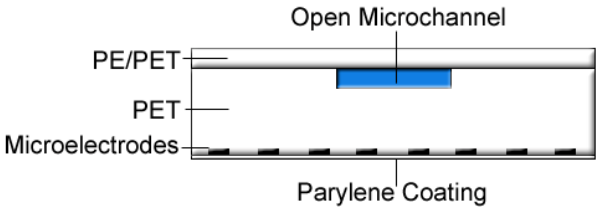

Figure 8.2. Front view schematic representation of a fountain pen array for SECM imaging.

Additionally, the fountain pen probe might be employed in particular to study living cell response under an *in situ* localized variation of cell media conditions such as pH, drug concentration or embryo growth control by following oxygen consumption. For doing this, cells can be encapsulated into well arrays as reported by Torisawa *et al.*[218] The advantages that the fountain pen probe could offer over the conventional microelectrodes is the spatial localized dynamic control of the cell media, thanks to the fact that it can operate in a pointillist mode. In such situation a nanolitre droplet at the bottom of the probe connects it, to a well–defined surface area to study locally the substrate. Moreover, the fountain pen probe can also operate in a scanning mode avoiding topographic artifacts.

Furthermore, more complicated microfluidic systems can be prepared by adding supplementary open microchannels for the aspiration of the flowing redox mediator solution, avoiding sample contamination encountered during scanning with a fountain pen device. Moreover, such microfluidic systems might be also useful for surface

patterning by reacting (electro)chemically one or two different components at the tip of the probe, similar to the capillary–based droplet–cell concept reported recently by Schuhmann *et al.*[130] The advantages that this dual microchannel device could offer is the feasibility to introduce more chemicals into the reaction, be used as a write and read device and lower possibilities of capillary or substrate destruction when a physical contact between them is established. In addition, one can envisage to use the aspiration channel for coupling SECM with others analytical techniques such mass spectrometry, chromatography or capillary electrophoresis. Therefore, relevant analytes detected by SECM over dry or wet surfaces can be extracted by the aspiration channel and delivered to a complementary analytical technique. As a consequence, on–line monitoring of electrochemical and chemical surface information can be imagined (see Figure 8.3).

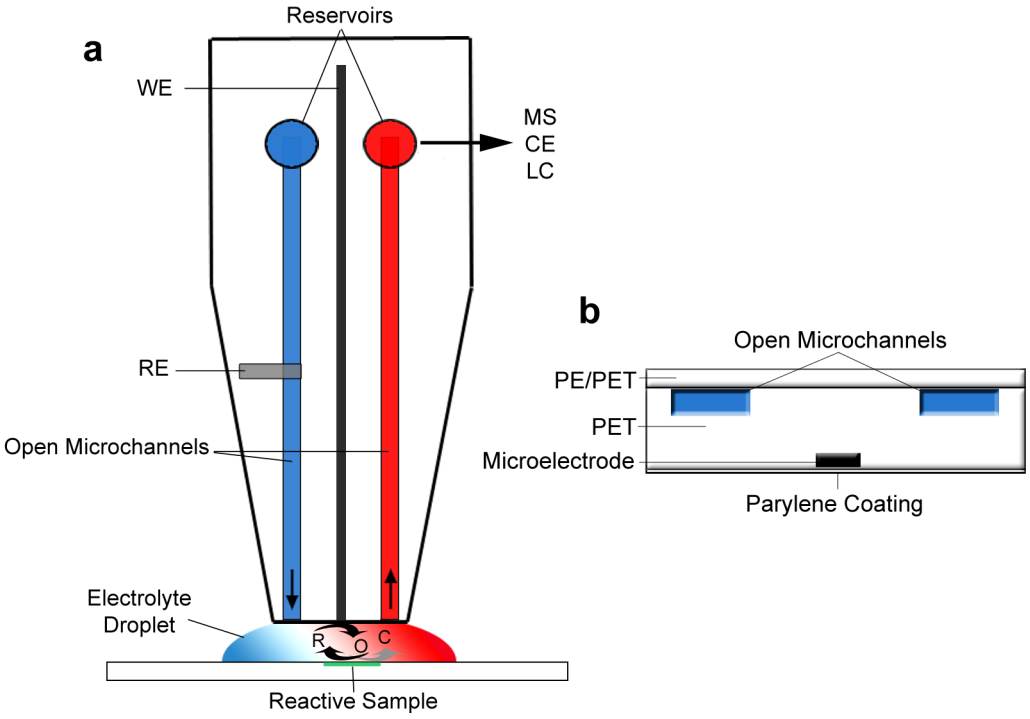

Figure 8.3. a) Schematic representation of the push and pull system as a writing and reading device. It might be possible to connect it with a secondary analytical technique such as mass spectrometry (MS), capillary electrophoresis (CE) and liquid chromatography (LC). b) Front view of the push and pull system tip.

From the fabrication point of view, soft SECM probes can be prepared by using different approaches, such as photolithography, in which case a wafer–level batch fabrication for reproducible production of standard soft stylus probes can be achieved (see Figure 8.4.). Less demanding techniques might be used for the preparation of microelectrodes simply by printing processes.

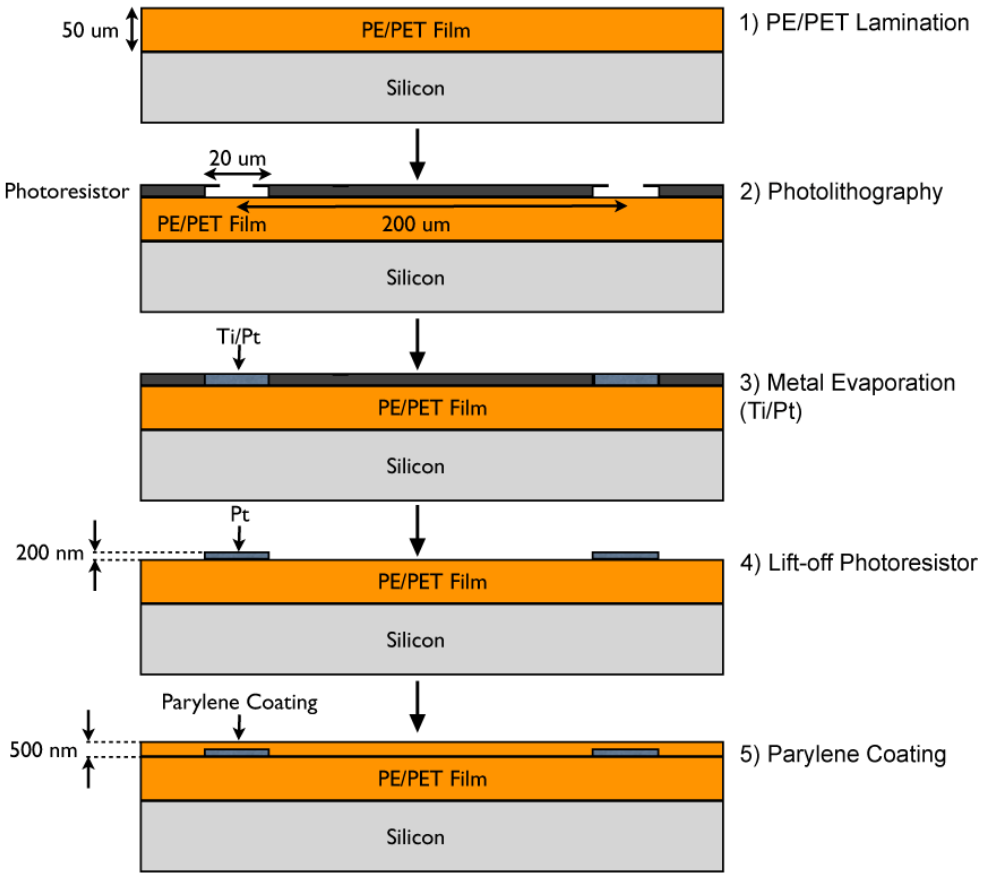

Figure 8.4. Schematic representation of the microelectrode array preparation by photolithography. Only the preparation of two microelectrodes is shown, but it can be extended to 32 or 128 microelectrodes.

In summary, the time has come for imaging chemical reactivity on substrates of different shapes and sizes, and for SECM to become a routine imaging tool with applications ranging from biological tissue imaging to process control.

9. BIBLIOGRAPHY

1. E. S. Lander*, et al.*, Nature. 2001, 409. 860-921.
2. T. G. Ksiazek*, et al.*, New England Journal of Medicine. 2003, 348. 1953-1966.
3. M. J. Van De Vijver*, et al.*, New England Journal of Medicine. 2002, 347. 1999-2009.
4. I. S. Farooqi, J. M. Keogh, G. S. H. Yeo, E. J. Lank, T. Cheetham, S. O'Rahilly, New England Journal of Medicine. 2003, 348. 1085-1095.
5. S. K. Pedersen*, et al.*, Journal of Proteome Research. 2003, 2. 303-311.
6. V. C. Wasinger*, et al.*, Electrophoresis. 1995, 16. 1090-1094.
7. P. G. Righetti, Electrophoresis. 2004, 25. 2111-2127.
8. P. G. Righetti, Isoelectric focusing: theory, methodology and applications. Third ed.; Elsevier biomedical press: Amsterdam, 1983; Vol. 11.
9. H. Zhang, E. S. Yeung, Electrophoresis. 2006, 27. 3609-3618.
10. A. Xu, C. Sluszny, E. S. Yeung, Journal of Chromatography A. 2005, 1087. 177-182.
11. C. Sluszny, E. S. Yeung, Analytical Chemistry. 2004, 76. 1359-1365.
12. M. Zhang, H. H. Girault, Electrochemistry Communications. 2007, 9. 1778-1782.
13. M. Carano, N. Lion, H. H. Girault, Journal of Electroanalytical Chemistry. 2007, 599. 349-355.
14. M. Carano, N. Lion, J. P. Abid, H. H. Girault, Electrochemistry Communications. 2004, 6. 1217-1221.
15. M. Zhang, G. Wittstock, Y. Shao, H. H. Girault, Analytical Chemistry. 2007, 79. 4833-4839.
16. G. Binnig, H. Rohrer, C. Gerber, E. Weibel, Applied Physics Letters. 1982, 40. 178-180.
17. G. Binnig, C. F. Quate, C. Gerber, Physical Review Letters. 1986, 56. 930-933.
18. S. R. Higgins, R. J. Hamers, Journal of Vacuum Science and Technology B: Microelectronics and Nanometer Structures. 1996, 14. 1360-1364.
19. M. Nonnenmacher, M. P. O'Boyle, H. K. Wickramasinghe, Applied Physics Letters. 1991, 58. 2921-2923.
20. E. Betzig, J. K. Trautman, T. D. Harris, J. S. Weiner, R. L. Kostelak, Science. 1991, 251. 1468-1470.
21. R. C. Engstrom, Analytical Chemistry. 1984, 56. 890-894.
22. R. C. Engstrom, M. Weber, D. J. Wunder, R. Burgess, S. Winquist, Analytical Chemistry. 1986, 58. 844-848.
23. H. Y. Liu, F. R. F. Fan, C. W. Lin, A. J. Bard, Journal of the American Chemical Society. 1986, 108. 3838-3839.
24. A. J. Bard, F. R. F. Fan, J. Kwak, O. Lev, Analytical Chemistry. 1989, 61. 132-138.
25. J. Kwak, A. J. Bard, Analytical Chemistry. 1989, 61. 1221-1227.
26. R. C. Engstrom, C. M. Pharr, Analytical Chemistry. 1989, 61. 1099 A-1104 A.

27. A. J. Bard, F. R. F. Fan, D. T. Pierce, P. R. Unwin, D. O. Wipf, F. Zhou, Science. 1991, 254. 68-74.
28. A. L. Barker, M. Gonsalves, J. V. MacPherson, C. J. Slevin, P. R. Unwin, Analytica Chimica Acta. 1999, 385. 223-240.
29. E. M. Hussien, T. Erichsen, W. Schuhmann, M. Maclejewska, Analytical and Bioanalytical Chemistry. 2008, 391. 1773-1782.
30. T. Wilhelm, G. Wittstock, Angewandte Chemie - International Edition. 2003, 42. 2248-2250.
31. G. Wittstock, R. Hesse, W. Schuhmann, Electroanalysis. 1997, 9. 746-750.
32. T. Yasukawa, T. Kaya, T. Matsue, Electroanalysis. 2000, 12. 653-659.
33. H. Shiku*, et al.*, Analytica Chimica Acta. 2004, 522. 51-58.
34. J. Velmurugan, P. Sun, M. V. Mirkin, Journal of Physical Chemistry C. 2009, 113. 459-464.
35. P. Sun, M. V. Mirkin, Analytical Chemistry. 2006, 78. 6526-6534.
36. K. Fushimi, T. Okawa, K. Azumi, M. Seo, Journal of the Electrochemical Society. 2000, 147. 524-529.
37. K. Fushimi, M. Seo, Zairyo to Kankyo. 1997, 46. 797-803.
38. D. A. Walsh, J. L. Fernandez, A. J. Bard, Journal of the Electrochemical Society. 2006, 153. E99-E103.
39. M. Zhang, H. H. Girault, Analyst. 2009, 134. 25-30.
40. D. Mandler, in Scanning Electrochemical Microscopy, ed. A. J. Bard, M. V. Mirkin. Marcel Dekker: New York, Basel., 2001, pp 593-627.
41. C. J. Slevin, J. V. Macpherson, P. R. Unwin, Journal of Physical Chemistry B. 1997, 101. 10851-10859.
42. R. Cornut, C. Lefrou, Journal of Electroanalytical Chemistry. 2008, 621. 178-184.
43. M. V. Mirkin, A. J. Bard, Journal of Electroanalytical Chemistry. 1992, 323. 29-51.
44. C. Wei, A. J. Bard, M. V. Mirkin, Journal of Physical Chemistry. 1995, 99. 16033-16042.
45. J. L. Amphlett, G. Denuault, Journal of Physical Chemistry B. 1998, 102. 9946-9951.
46. O. Sklyar, G. Wittstock, Journal of Physical Chemistry B. 2002, 106. 7499-7508.
47. T. Nann, J. Heinze, Electrochimica Acta. 2003, 48. 3975-3980.
48. C. G. Zoski, Electroanalysis. 2002, 14. 1041-1051.
49. G. Zhao, D. M. Giolando, J. R. Kirchhoff, Journal of Electroanalytical Chemistry. 1994, 379. 505-508.
50. C. Kranz, G. Friedbacher, B. Mizaikofft, A. Lugstein, J. Smoliner, E. Bertagnolli, Analytical Chemistry. 2001, 73. 2491-2500.
51. A. L. Barker, P. R. Unwin, J. W. Gardner, H. Rieley, Electrochemistry Communications. 2004, 6. 91-97.
52. C. Demaille, M. Brust, M. Tsionsky, A. J. Bard, Analytical Chemistry. 1997, 69. 2323-2328.
53. K. R. Wehmeyer, R. M. Wightman, Analytical Chemistry. 1985, 57. 1989-1993.
54. K. R. Wehmeyer, M. R. Deakin, R. M. Wightman, Analytical Chemistry. 1985, 57. 1913-1916.

55. D. R. MacFarlane, D. K. Y. Wong, Journal of Electroanalytical Chemistry. 1985, 185. 197-202.
56. M. Fleischmann, S. Bandyopadhyay, S. Pons, Journal of Physical Chemistry. 1985, 89. 5537-5541.
57. F. Cortes-Salazar, M. Traeuble, F. Li, J.-M. Busnel, A. Gassner, M. Hojeij, G. Wittstock, H. H. Girault, Analytical Chemistry. 2009, 81. 6889-6896.
58. K. Stulik, C. Amatore, K. Holub, V. Marecek, W. Kutner, Pure and Applied Chemistry. 2000, 72. 1483-1492.
59. J. Heinze, Angewandte Chemie (International Edition in English). 1993, 32. 1268-1288.
60. K. Aoki, J. Osteryoung, Journal of Electroanalytical Chemistry. 1981, 122. 19-35.
61. D. Shoup, A. Szabo, Journal of Electroanalytical Chemistry. 1982, 140. 237-245.
62. D. Shoup, A. Szabo, Journal of Electroanalytical Chemistry. 1984, 160. 27-31.
63. C. G. Zoski, M. V. Mirkin, Analytical Chemistry. 2002, 74. 1986-1992.
64. G. Wittstock, B. Grondig, B. Strehlitz, K. Zimmer, Electroanalysis. 1998, 10. 526-531.
65. Y. Shao, M. V. Mirkin, G. Fish, S. Kokotov, D. Palanker, A. Lewis, Analytical Chemistry. 1997, 69. 1627-1634.
66. O. Ordeig, J. Del Campo, F. X. Muñoz, C. E. Banks, R. G. Compton, Electroanalysis. 2007, 19. 1973-1986.
67. A. Bard, L. Faulkner, Electrochemical methods. Fundamentals and applications. Second edition ed.; Wiley: New York, 2001.
68. K. Nunes, K. Hallmeier, R. Szargan, T. Raschke, C. Radehaus, G. Wittstock, Electroanalysis. 2007, 19. 1023-1031.
69. G. Wittstock, T. Asmus, T. Wilhelm, Fresenius' Journal of Analytical Chemistry. 2000, 367. 346-351.
70. G. Wittstock, M. Burchardt, S. E. Pust, Y. Shen, C. Zhao, Angewandte Chemie - International Edition. 2007, 46. 1584-1617.
71. P. Sun, F. O. Laforge, M. V. Mirkin, Physical Chemistry Chemical Physics. 2007, 9. 802-823.
72. D. O. Wipf, A. J. Bard, Journal of the Electrochemical Society. 1991, 138. 469-474.
73. A. L. Whitworth, D. Mandler, P. R. Unwin, Physical Chemistry Chemical Physics. 2005, 7. 356-365.
74. S. E. Pust, M. Salomo, E. Oesterschulze, G. Wittstock, Nanotechnology. 2010, 21. 105709-105701-105709-105712.
75. Q. Fulian, A. C. Fisher, G. Denuault, Journal of Physical Chemistry B. 1999, 103. 4393-4398.
76. Q. Fulian, A. C. Fisher, G. Denuault, Journal of Physical Chemistry B. 1999, 103. 4387-4392.
77. Q. Fulian, A. C. Fisher, Journal of Physical Chemistry B. 1998, 102. 9647-9652.
78. T. Nann, J. Heinze, Electrochemistry Communications. 1999, 1. 289-294.
79. P. Hoffmann, T. Sidler, Course Micro-Machining with Laser.; Ecole Polytechnique Federale de Lausanne. Lausanne, 2009.
80. D. Bauerle, Laser processing and chemistry. Third ed.; Springer-Verlag: Berlin, 2000.

81. H. Svensson, Acta chemica Scandinavica. 1961, 15. 325-341.
82. O. Vesterberg, H. Svensson, Acta chemica Scandinavica. 1966, 20. 820-834.
83. C. Cao, Journal of Chromatography A. 1998, 813. 153-171.
84. A. Ros, M. Faupel, H. Mees, J. Van Oostrum, R. Ferrigno, F. Reymond, P. Michel, J. S. Rossier, H. H. Girault, Proteomics. 2002, 2. 151-156.
85. H. H. Girault, Analytical and physical electrochemistry. EPFL press and Marcel Dekker Inc: New York, 2004; p 254.
86. G. T. Matioli, H. B. Niewisch, Science. 1965, 150. 1824-1826.
87. J. Han, A. K. Singh, Journal of Chromatography A. 2004, 1049. 205-209.
88. Z. Demianova, M. Shimmo, E. Poysa, S. Franssila, M. Baumann, Electrophoresis. 2007, 28. 422-428.
89. J. Gutenwik, B. Nilsson, A. Axelsson, Biochemical Engineering Journal. 2004, 19. 1-7.
90. T. Rabilloud, L. Vuillard, C. Gilly, J. J. Lawrence, Cellular and Molecular Biology. 1994, 40. 57-75.
91. V. Neuhoff, N. Arold, D. Taube, W. Ehrhardt, Electrophoresis. 1988, 9. 255-262.
92. T. H. Steinberg*, et al.*, Proteomics. 2003, 3. 1128-1144.
93. C. R. Merril, Methods in Enzymology. 1990, 182. 477-488.
94. A. Mayer, S. Neuenhofer, Angewandte Chemie (International ed. in English). 1994, 33. 1044 - 1072.
95. R. Westermeier, R. Marouga, Bioscience Reports. 2005, 25. 19-32.
96. W. F. Patton, Journal of Chromatography B: Analytical Technologies in the Biomedical and Life Sciences. 2002, 771. 3-31.
97. L. R. R. Ogorzalek, C. Mitchell, T. I. Stevenson, J. A. Loo, P. C. Andrews, International Journal of Mass Spectrometry and Ion Processes. 1997, 169-170. 273-290.
98. B. K. Sørensen, P. Højrup, E. Østergård, C. S. Jørgensen, J. Enghild, L. R. Ryder, G. Houen, Analytical Biochemistry. 2002, 304. 33-41.
99. H. Chen, G. D. Chang, Electrophoresis. 2001, 22. 1894-1899.
100. B. P. Voris, D. A. Young, Analytical Biochemistry. 1980, 104. 478-484.
101. M. C. Pietrogrande, N. Marchetti, F. Dondi, P. G. Righetti, Electrophoresis. 2003, 24. 217-224.
102. M. C. Pietrogrande, N. Marchetti, F. Dondi, P. G. Righetti, Electrophoresis. 2002, 23. 283-291.
103. C. Zhao, G. Wittstock, Biosensors and Bioelectronics. 2005, 20. 1277 - 1284.
104. Q. Fu, J. E. Van Eyk, Expert Review of Proteomics. 2006, 3. 237-249.
105. J. A. Burgess*, et al.*, Journal of Proteome Research. 2006, 5. 1674-1681.
106. W. F. Patton, Journal of Chromatography B. 2002, 771. 3-31.
107. S. Sriyam, S. Sinchaikul, P. Tantipaiboonwong, C. Tzao, S. Phutrakul, S. T. Chen, Journal of Chromatography B. 2007, 849. 91-104.
108. P. G. Righetti, A. Castagna, B. Herbert, G. Candiano, Bioscience Reports. 2005, 25. 3-17.
109. A. Mayer, S. Neuenhofer, Angewandte Chemie - International Edition. 1994, 33. 1044-1072.
110. D. S. Wilbur, Bioconjugate Chemistry. 1992, 3. 433-470.
111. K. Berggren*, et al.*, Analytical Biochemistry. 1999, 276. 129-143.
112. G. Wittstock, Analytical and Bioanalytical Chemistry. 2001, 370. 303-315.

113. G. Wittstock, K. J. Yu, H. B. Halsall, T. H. Ridgway, W. R. Heineman, Analytical Chemistry. 1995, 67. 3578-3582.
114. M. Carano, N. Lion, H. H. Girault, Chimia. 2005, 59. 105-108.
115. S. Wang, X. Zhang, F. E. Regnier, Journal of Chromatography A. 2002, 949. 153-162.
116. S. Sechi, B. T. Chait, Analytical Chemistry. 1998, 70. 5150-5158.
117. T. C. Rohner, J. S. Rossier, H. H. Girault, Electrochemistry Communications. 2002, 4. 695-700.
118. C. Roussel, L. Dayon, N. Lion, T. C. Rohner, J. Josserand, J. S. Rossier, H. Jensen, H. H. Girault, Journal of the American Society for Mass Spectrometry. 2004, 15. 1767-1779.
119. C. Roussel, T. C. Rohner, H. Jensen, H. H. Girault, ChemPhysChem. 2003, 4. 200-206.
120. L. Dayon. Thiol-targeted microspray mass spectrometry of peptides and proteins through on-line ec-tagging. Ecole Polytechnique Federale de Lausanne (EPFL), Lausanne, 2006.
121. K. Nakano, K. Nakamura, K. Iwamoto, N. Soh, T. Imato, Journal of Electroanalytical Chemistry. 2009, 628. 113-118.
122. L. Dayon, C. Roussel, H. H. Girault, Journal of Proteome Research. 2006, 5. 793-800.
123. M. P. Lutolf, N. Tirelli, S. Cerritelli, L. Cavalli, J. A. Hubbell, Bioconjugate Chemistry. 2001, 12. 1051-1056.
124. C. Roussel, L. Dayon, H. Jensen, H. H. Girault, Journal of Electroanalytical Chemistry. 2004, 570. 187-199.
125. S. Harper, D. W. Speicher, in Current protocols in protein science, ed. J. E. Coligan. John Wiley & Sons, Inc., 2001.
126. J. Sasse, S. R. Gallagher, in Current Protocols in Immunology, ed. J. E. Coligan. John Wiley & Sons, Inc., 2008.
127. M. Carano, K. B. Holt, A. J. Bard, Analytical Chemistry. 2003, 75. 5071-5079.
128. G. B. Sigal, M. Mrksich, G. M. Whitesides, Journal of the American Chemical Society. 1998, 120. 3464-3473.
129. B. Wang, B. Shi, Journal of Macromolecular Science, Part B: Physics. 2010, 49. 383-391.
130. X. Chen, K. Eckhard, M. Zhou, M. Bron, W. Schuhmann, Analytical Chemistry. 2009, 81. 7597-7603.
131. T. C. Nagaiah, A. Maljusch, X. Chen, M. Bron, W. Schuhmann, ChemPhysChem. 2009, 10. 2711-2718.
132. S. Schwamborn, L. Stoica, X. Chen, W. Xia, S. Kundu, M. Muhler, W. Schuhmann, Chemphyschem : a European journal of chemical physics and physical chemistry. 2010, 11. 74-78.
133. X. Chen, M. Bron, L. Stoica, W. Schuhmann, The 60th Annual Meeting of the International Society of Electrochemistry., Bejing, China, 2009.
134. C. Wei, A. J. Bard, G. Nagy, K. Toth, Analytical Chemistry. 1995, 67. 1346-1356.
135. D. O. Wipf, A. J. Bard, Analytical Chemistry. 1992, 64. 1362-1367.

136. D. O. Wipf, A. J. Bard, D. E. Tallman, Analytical Chemistry. 1993, 65. 1373-1377.
137. J. V. Macpherson, P. R. Unwin, Analytical Chemistry. 2000, 72. 276-285.
138. A. Kueng, C. Kranz, A. Lugstein, E. Bertagnolli, B. Mizaikoff, Angewandte Chemie - International Edition. 2003, 42. 3238-3240.
139. O. Sklyar, A. Kueng, C. Kranz, B. Mizaikoff, A. Lugstein, E. Bertagnolli, G. Wittstock, Analytical Chemistry. 2005, 77. 764-771.
140. A. Davoodi, J. Pan, C. Leygraf, S. Norgren, Electrochimica Acta. 2007, 52. 7697-7705.
141. R. J. Fasching, Y. Tao, F. B. Prinz, Chem. Sens. 2004, 20. 318-319.
142. P. L. T. M. Frederix*, et al.*, Nanotechnology. 2008, 19.
143. A. Ueda, O. Niwa, K. Maruyama, Y. Shindo, K. Oka, K. Suzuki, Angewandte Chemie - International Edition. 2007, 46. 8238-8241.
144. T. H. Treutler, G. Wittstock, Electrochimica Acta. 2003, 48. 2923-2932.
145. M. Ludwig, C. Kranz, W. Schuhmann, H. E. Gaub, Review of Scientific Instruments. 1995, 66. 2857-2860.
146. H. Shin, P. J. Hesketh, B. Mizaikoff, C. Kranz, Sensors and Actuators, B: Chemical. 2008, 134. 488-495.
147. N. R. Wilson, D. H. Cobden, J. V. Macpherson, Journal of Physical Chemistry B. 2002, 106. 13102-13105.
148. N. R. Wilson, J. V. Macpherson, Nano Letters. 2003, 3. 1365-1369.
149. D. P. Burt, N. R. Wilson, J. M. R. Weaver, P. S. Dobson, J. V. Macpherson, Nano Letters. 2005, 5. 639-643.
150. D. P. Burt, P. S. Dobson, J. M. R. Weaver, N. R. Wilson, P. R. Unwin, J. V. Macpherson, Proceedings of IEEE Sensors, Atlanta, GA, 2007. 712-715.
151. P. I. James, L. F. Garfias-Mesias, P. J. Moyer, W. H. Smyrl, Journal of the Electrochemical Society. 1998, 145.
152. Y. Lee, Z. Ding, A. J. Bard, Analytical Chemistry. 2002, 74. 3634-3643.
153. B. Ballesteros Katemann, A. Schulte, W. Schuhmann, Chemistry - A European Journal. 2003, 9. 2025-2033.
154. N. Baltes, L. Thouin, C. Amatore, J. Heinze, Angewandte Chemie - International Edition. 2004, 43. 1431-1435.
155. H. Yamada, H. Fukumoto, T. Yokoyama, T. Koike, Analytical Chemistry. 2005, 77. 1785-1790.
156. D. Oyamatsu, Y. Hirano, N. Kanaya, Y. Mase, M. Nishizawa, T. Matsue, Bioelectrochemistry. 2003, 60. 115-121.
157. A. S. Baranski, P. M. Diakowski, Journal of Solid State Electrochemistry. 2004, 8. 683-692.
158. P. M. Diakowski, Z. Ding, Electrochemistry Communications. 2007, 9. 2617-2621.
159. M. Etienne, A. Schulte, W. Schuhmann, Electrochemistry Communications. 2004, 6. 288-293.
160. K. B. Ballesteros, A. Schulte, E. J. Calvo, M. Koudelka-Hep, W. Schuhmann, Electrochemistry Communications. 2002, 4. 134-138.
161. M. A. Alpuche-Aviles, D. O. Wipf, Analytical Chemistry. 2001, 73. 4873-4881.

162. M. Zhang, A. Becue, M. Prudent, C. Champod, H. H. Girault, Chemical Communications. 2007. 3948-3950.
163. M. Zhang, B. Su, F. Cortes-Salazar, M. Hojeij, H. H. Girault, Electrochemistry Communications. 2008, 10. 714-718.
164. M. A. Roberts, J. S. Rossier, P. Bercier, H. Girault, Analytical Chemistry. 1997, 69. 2035-2042.
165. J. S. Rossier, M. A. Roberts, R. Ferrigno, H. H. Girault, Analytical Chemistry. 1999, 71. 4294-4299.
166. K. D. Sternitzke, R. L. McCreery, Analytical Chemistry. 1990, 62. 1339-1344.
167. M. Etienne, J. Oni, A. Schulte, G. Hartwich, W. Schuhmann, Electrochimica Acta. 2005, 50. 5001-5008.
168. J. S. Rossier, H. H. Girault, Physical Chemistry Chemical Physics. 1999, 1. 3647-3652.
169. M. D. Osborne, B. J. Seddon, R. A. W. Dryfe, G. Lagger, U. Loyall, H. Schafer, H. H. Girault, Journal of Electroanalytical Chemistry. 1996, 417. 5-15.
170. O. Sklyar, M. Trauble, C. Zhao, G. Wittstock, Journal of Physical Chemistry B. 2006, 110. 15869-15877.
171. O. Sklyar, T. H. Treutler, N. Vlachopoulos, G. Wittstock, Surface Science. 2005, 597. 181-195.
172. M. N. Holder, C. E. Gardner, J. V. Macpherson, P. R. Unwin, Journal of Electroanalytical Chemistry. 2005, 585. 8-18.
173. G. Wittstock, H. Emons, T. H. Ridgway, E. A. Blubaugh, W. R. Heineman, Analytica Chimica Acta. 1994, 298. 285-302.
174. A. Davoodi, A. Farzadi, J. Pan, C. Leygraf, Y. Zhu, Journal of the Electrochemical Society. 2008, 155. C474-C485.
175. M. M. Lohrengel, A. Moehring, M. Pilaski, Fresenius' Journal of Analytical Chemistry. 2000, 367. 334-339.
176. T. W. Spaine, J. E. Baur, Analytical Chemistry. 2001, 73. 930-938.
177. F. Turcu, A. Schulte, W. Schuhmann, Analytical and Bioanalytical Chemistry. 2004, 380. 736-741.
178. T. M. Day, P. R. Unwin, J. V. Macpherson, Nano Letters. 2007, 7. 51-57.
179. A. P. Suryavanshi, M. F. Yu, Nanotechnology. 2007, 18. art. no. 105305.
180. J. C. Ball, D. L. Scott, J. K. Lumpp, S. Daunert, J. Wang, L. G. Bachas, Analytical Chemistry. 2000, 72. 497-501.
181. C. D. T. Bratten, P. H. Cobbod, J. M. Cooper, Analytical Chemistry. 1997, 69. 253-258.
182. D. Juncker, H. Schmid, E. Delamarche, Nature Materials. 2005, 4. 622-627.
183. A. Lewis, Y. Kheifetz, E. Shambrodt, A. Radko, E. Khatchatryan, C. Sukenik, Applied Physics Letters. 1999, 75. 2689-2691.
184. S. Eklund, L. Hedlund, Journal of Scientific Instruments. 1951, 28. 30.
185. C. Shin, K. Hwang, Y. Kim, H. Kim, Digest of Papers - Microprocesses and Nanotechnology 2007; 20th International Microprocesses and Nanotechnology Conference, MNC. 2007. 502-503.
186. S. Deladi, N. R. Tas, J. W. Berenschot, J. H. De Boer, M. J. De Boer, G. J. M. Krijnen, M. C. Elwenspoek, Proceedings of the IEEE International Conference on Micro Electro Mechanical Systems (MEMS). 2005. 564-567.

187. M. A. Roberts, J. S. Rossier, P. Bercier, H. H. Girault, Analytical Chemistry. 1997, 69. 2035-2042.
188. J. S. Rossier, M. A. Roberts, R. Ferrigno, H. H. Girault, Analytical Chemistry. 1999, 71. 4294-4299.
189. J. L. Fernandez, D. A. Walsh, A. J. Bard, Journal of the American Chemical Society. 2005, 127. 357-365.
190. M. Black, J. Cooper, P. McGinn, Measurement Science and Technology. 2005, 16. 174-182.
191. A. Minguzzi, M. A. Alpuche-Aviles, J. R. Lopez, S. Rondinini, A. J. Bard, Analytical Chemistry. 2008, 80. 4055-4064.
192. A. J. Bard, Journal of the American Chemical Society. 2010, 132. 7559-7567.
193. I. Rianasari, L. Walder, M. Burchardt, I. Zawisza, G. Wittstock, Langmuir. 2008, 24. 9110-9117.
194. G. Wittstock, Fresenius Journal of Analytical Chemistry. 2001, 370. 303-315.
195. C. Nunes Kirchner, M. Traeuble, G. Wittstock, Analytical Chemistry. 2010, 82. 2626-2635.
196. W. Liu, H. Ye, A. J. Bard, Journal of Physical Chemistry C. 2010, 114. 1201-1207.
197. C. Combellas, M. Fermigier, A. Fuchs, F. Kanoufi, Analytical Chemistry. 2005, 77. 7966-7975.
198. C. G. Zoski, N. Simjee, O. Guenat, M. Koudelka-Hep, Analytical Chemistry. 2004, 76. 62-72.
199. S. Hong, C. A. Mirkin, Science. 2000, 288. 1808-1811.
200. P. Vettiger*, et al.*, IBM Journal of Research and Development. 2000, 44. 323-340.
201. R. J. Fasching, Y. Tao, F. B. Prinz, Sensor Actuat B-Chem. 2005, 108. 964-972.
202. H. Meyer, H. Drewer, B. Gründig, K. Cammann, R. Kakerow, Y. Manoli, W. Mokwa, M. Rospert, Analytical Chemistry. 1995, 67. 1164-1170.
203. L. Zhang, X. Z. Ma, J. L. Zhuang, C. K. Qiu, C. L. Du, J. Tang, Z. W. Tian, Advanced Materials. 2007, 19. 3912-3918.
204. T. Leïchlé, L. Nicu, E. Descamps, B. Corso, P. Mailley, T. Livache, C. Bergaud, Applied Physics Letters. 2006, 88. 254108.
205. C. Amatore, J. M. Saveant, D. Tessier, Journal of Electroanalytical Chemistry. 1983, 147. 39-51.
206. D. Shoup, A. Szabo, Journal of Electroanalytical Chemistry. 1984, 160. 19-26.
207. D. Menshykau, X. Huang, N. V. Rees, F. J. del Campo, F. X. Munoz, R. G. Compton, Analyst. 2009, 134. 343-348.
208. A. M. Bond, K. B. Oldham, C. G. Zoski, Analytica Chimica Acta. 1989, 216. 177-230.
209. R. M. Wightman, D. O. Wipf, in Electroanalytical Chemistry, ed. A. J. Bard. Marcel Dekker: New York 1989, 1989, vol. 15, pp 267–353.
210. F. Cortés-Salazar, J.-M. Busnel, F. Li, H. H. Girault, Journal of Electroanalytical Chemistry. 2009, 635. 69-74.
211. F. Cortés-Salazar, A. Lesch, D. Momotenko, J.-M. Busnel, G. Wittstock, H. H. Girault, Analytical Methods. 2010, 2. 817-823.
212. O. Sklyar, J. Ufheil, J. Heinze, G. Wittstock, Electrochimica Acta. 2003, 49. 117-128.

213. F. Cortes-Salazar, M. Zhang, A. Becue, J.-M. Busnel, M. Prudent, C. Champood, H. H. Girault, Chimia. 2009, 63. 580.
214. G. Zilberstein, L. Korol, P. G. Righetti, S. Bukshpan, Analytical Chemistry. 2007, 79. 8624-8630.
215. G. Zilberstein, L. Korol, P. Antonioli, P. G. Righetti, S. Bukshpan, Analytical Chemistry. 2007, 79. 821-827.
216. G. Zilberstein, S. Bukshpan, P. G. Righetti, Electrophoresis. 2010, 31. 1747-1753.
217. M. Berth, F. M. Moser, M. Kolbe, J. Bernhardt, Applied Microbiology and Biotechnology. 2007, 76. 1223-1243.
218. Y. S. Torisawa, T. Kaya, Y. Takii, D. Oyamatsu, M. Nishizawa, T. Matsue, in Analytical Chemistry. 2003, vol. 75, pp 2154-2158.

Appendix 1. Corrosion stability study of a ball alloy in different commercial inks by SECM.

The following appendix presents the corrosion evaluation of a ball alloy in the presence of different commercial inks by SECM. This project was developed in collaboration with a Swiss company and that for term contract agreement it is not possible to show completely here. For this reason only few experiments are contained in this appendix, without reporting the composition of the alloy or the tested inks.

This project has the following milestones:

1. Fabrication of a supporting setup for 16 balls of 500 μm diameter.
2. Lecture of the balls with SECM in an alkaline solution of ferrocene methanol.
3. Electrochemical oxidation of the balls in the alkaline media and two commercial inks (Ink number 1 and number 2).
4. Lecture of the balls after the oxidation process with SECM in an alkaline solution of ferrocene methanol.

Project development:

1. Fabrication of a supporting setup for 16 balls of 500 μm diameter.

For testing purposes a supporting setup for 16 balls (4 balls x 4 balls) have been build. Different views of the setup can be observed in Figure A1.1. As it can be seen 16 holes

with a diameter equal to 300 μm has been drilled on a stainless steel sheet (see Figure A1.1b). The balls are fixed by a negative pressure that is applied from the bottom of the holder with a vacuum system (see Figure A1.a). The stainless steel holder has an electrical connection in order to be used as working electrode during the electrochemical oxidation of the balls. In the latter case, a mesh of stainless steel is used as counter electrode (see Figure A1.1c).

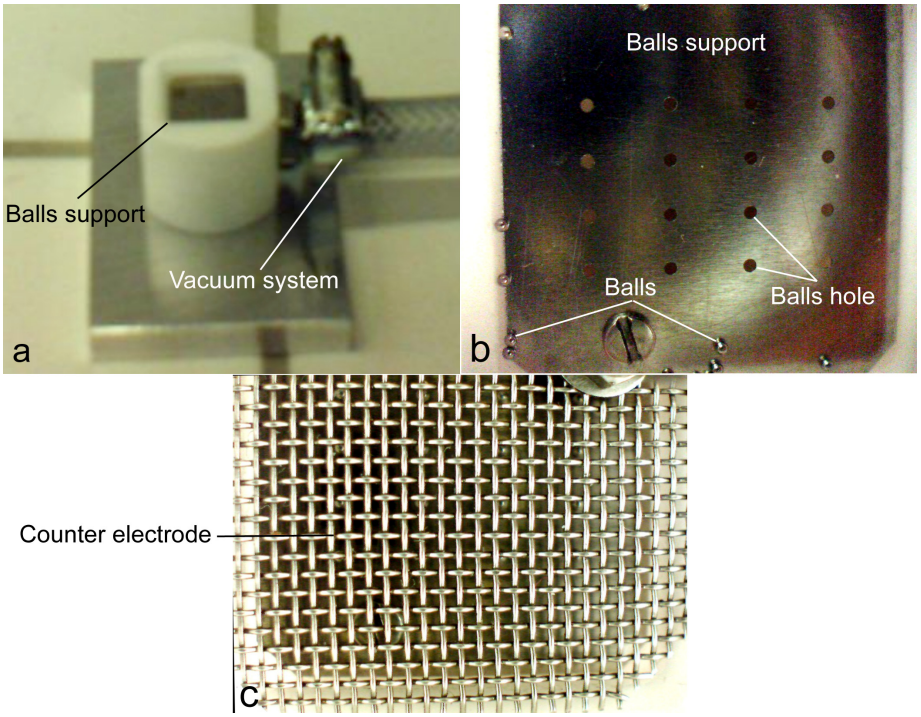

Figure A1.1. Developed setup for the assessment of the corrosion stability of one alloy in the presence of different commercial inks.

After the balls have been fixed, the system of vacuum can be stopped without loosing balls position. Then the electrolyte solution is added gently over the surface until it is completely cover.

2. Balls reading with SECM.

A solution of $FcCH_2OH$ 2 mM was prepared in Trys(hidroxymethyl) amino methane

(TRIS) 0.05 M with a pH equal to 8.68 in order to use it as redox mediator. Then one approach curve was performed over each one of the balls in order to determine the (electro)chemical activity on the tested balls. Figure A1.2 shows the approach curves over different balls before and after the polarization (electrochemical oxidation) of four balls. Since all the balls are made with the same alloy type, the reproducibility of the experiments can be controlled.

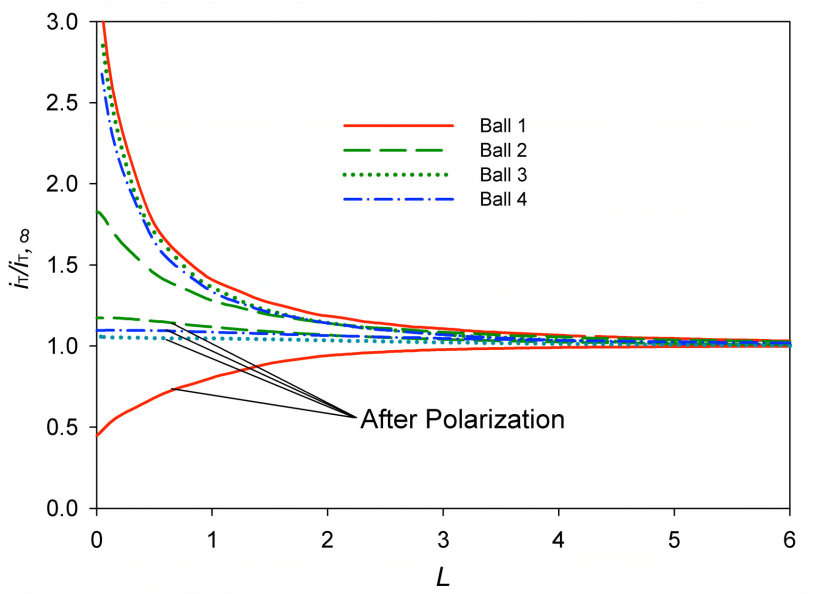

Figure A1.2. Experimental approach curves with a Pt microelectrode (diameter = 25 µm, *RG* = 8 – 9) in 2mM $FcCH_2OH$ with 0.05 M TRIS (pH = 8.68) over four different balls made of the same alloy, before and after electrochemical oxidation (Potential applied = 1.5 V, Time = 4 hours, 0.05 M TRIS). E_T = 0.35 V, translation rate 0.5 µm/s.

3. Electrochemical oxidation of the balls in alkaline media and lecture of the balls after the polarization with SECM.

The polarization process consisted on the application of a voltage equal to 1,5 V between the ball's support and a counter electrode placed on the top of the balls (stainless steel mesh) in a solution of TRIS 0.05M or in a commercial ink. Afterwards, the solution is replaced by a new TRIS 0.05 M solution and new approach curves are performed over each tested ball (see Figure A1.2).

When the electrode is approached to the ball surface before polarization, a current increment is observed most likely due to the electrical conductivity of the balls and its (electro)chemical surface activity. After polarization the current is decreased in all the cases, but in a different extent. This behavior could be explained taking into account that the alloy contains chromium and the formation of a chromium oxide (Cr_2O_3) film on the surface of the ball as a consequence of the polarization could take place. In fact this oxide is a good anticorrosive coating since it is not permeable by water and it presents a good mechanical and chemical stability on wide range of pH conditions. Therefore, the ball alloy is isolated, reducing the positive feedback. When the same procedure was repeated, but using during the polarization two different commercial inks (*i.e.* ink number 1 and number 2), a similar behavior was observed (see Figure A1.3a and Figure A1.b, respectively). The approach curves were performed on the same position over each ball before and after polarization.

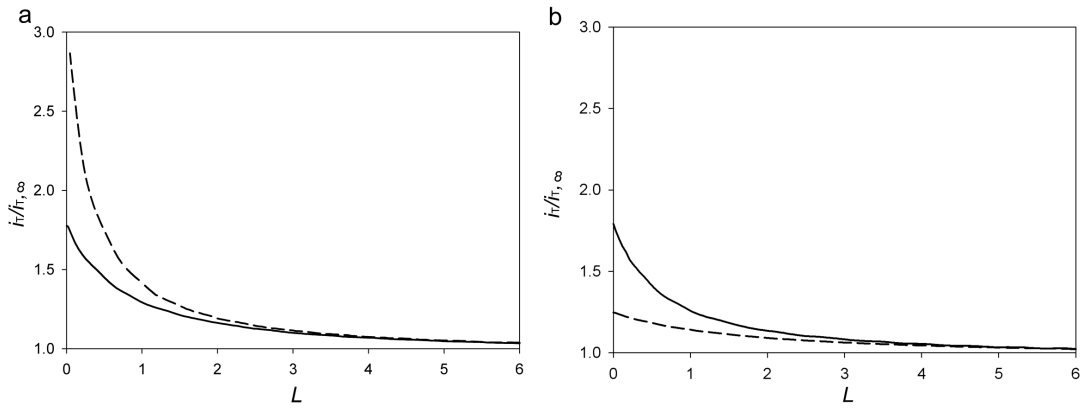

Figure A1.3. Experimental approach curves with a Pt microelectrode (diameter = 25 μm, *RG* = 8 – 9) in 2mM $FcCH_2OH$ with 0.05 M TRIS (pH = 8.68) over four different balls made of the same alloy, before (continuous line) and after (dashed line) electrochemical oxidation. The polarization process was performed in the ink a) 1 and b) 2. (Potential applied = 1.5 V, Time = 4 hours, 0.05 M TRIS). E_T = 0.35 V, translation rate 0.5 μm/s.

For the ink number 1 (see Figure A1.3a), the fact that SECM approach curves presented a higher current after ball polarization means that the formation of protective

oxide films (passivation) did not take place in the conditions in which the experiments were performed. It is expected that passivation processes mainly due to the formation of Cr_2O_3 is the most important strategy against corrosion for this type of alloy. As a consequence this alloy would be corroded continuously on the present conditions. In contrast, according to Figure A1.3b after the polarization of the balls in presence of the ink number 2, a decrease on the positive feedback is observed. The latter result means that less corrosive conditions are encountered in the ink number 2. By following the presented methodology, the swiss company could test the corrosion stability of ball alloys in different commercial inks in a reliable and less time consuming way.

Curriculum Vitae

FERNANDO CORTES SALAZAR

Date and place of Birth: May 23th, 1981, Bogotà, Colombia
Chemin de la Graviére 9, 1007 – Lausanne, Switzerland
Phone: (+41) 78 72 40 221
Email: fernando.cortessalazar@epfl.ch

EDUCATION

PhD (Chemistry) 2007 – 2010
Thesis: *Electrochemical and Electrokinetic Tools for Proteomics.*
Chemistry and Chemical Engineer Department, EPFL.
Supervisor: Professor Hubert H. Girault (PhD).
Expected graduation: October 2010.

Master (Chemistry) 2004 – 2006
Thesis: Electrochemical Characterization of Piperonilic Alcohol.
Chemistry Department, Universidad Nacional de Colombia.
Supervisor: Professor Marco Fidel Suarez (D.Phill).

Bachelor (Chemistry) 1999 – 2003
Thesis: Electrochemical Study of the Uncatalyzed Oscillating Reaction of Phenol and Bromate in an Acidic Medium.
Chemistry Department, Universidad Nacional de Colombia.
Supervisors: Professor Marco Fidel Suarez (D.Phill).
Professor Daniel Barragán (Dr.Sc).

AWARDS

- Oct. 2008. Best teaching assistant at the chemistry department. Ecole Polytechnique Fedérale de Lausanne.
- Aug. 2006. Outstanding Master Thesis Award Universidad Nacional de Colombia.

- 2004–2006. Outstanding Postgraduate Students Scholarship. Universidad Nacional de Colombia.

- Dec. 2003. Outstanding Bachelor Thesis Award Universidad Nacional de Colombia.

- Jan. 2002–Jul. 2002. Best GPA Award Universidad Nacional de Colombia.

- Jan. 2003–Jul. 2003. Best GPA Award Universidad Nacional de Colombia.

TEACHING AND WORKING EXPERIENCE

- 2009 – 2010 *Corrosion stability study of ball's alloys in different commercial inks by scanning electrochemical microscopy.* Consultancy given to PREMEC S.A. Ecole Polytechnique Fedérale de Lausanne. Switzerland.

- 2008 – 2009 *Scanning Electrochemical Microscopy*. Theoretical and practical course for chemistry (Master program). Ecole Polytechnique Fedérale de Lausanne. Switzerland.

- 2007 – 2009 *Analytical Chemistry*. Practical course for chemistry (Bachelor program). Ecole Polytechnique Fedérale de Lausanne. Switzerland.

- 2006 *Analytical Chemistry*. Practical course for engineering careers (Bachelor program). Universidad de los Andes. Colombia.

- 2004 – 2006 *Analytical Electrochemistry*. Practical course for chemistry (Bachelor program). Universidad Nacional de Colombia. Colombia.

- 2004 Basic Chemistry. Theoretical and practical course for engineering careers (Bachelor program). Universidad Nacional de Colombia. Colombia.

CONFERENCES PARTICIPATIONS

- SECM Imaging of Oxygen Reduction on PVDF Membranes: Indirect Protein Detection and Human Fingerprint Imaging (Poster). 60th Annual Meeting of the International Society of Electrochemistry. August 16 – 21, 2009 Beijing, China.

- Protein Imaging by Scanning Electrochemical Microscopy (Oral presentation). Colloque Electrochimie dans les Nanosciences. April 21 – 22, 2009 Paris, France.

- Soft Stylus Probe for Scanning Electrochemical Microscopy (Oral presentation). 5th Workshop on Scanning Electrochemical Microscopy. August 24 – 28, 2008 Minnowbrook, USA.

- Miniaturized IEF Separation Imaged by Scanning Electrochemical Microscopy (Poster). 22nd Symposium on MicroScale Bioseparations. March 9 – 13, 2008 Berlín, Germany.

- Electrosynthesis of Polyaniline (PANY) (Oral presentation). Noveno encuentro de estudiantes colombianos en química. October 15 – 20,2002 Cartagena de Indias, Colombia.

PUBLICATIONS

During the course of this PhD thesis:

- Cortés-Salazar, F., Momotenko, D., Lesch, A., Wittstock, G., Girault, H.H., Soft Microelectrode Linear Array for SECM. Submitted to Analytical Chemistry. 2010.

- Cortés-Salazar, F., Lesch, A., Momotenko, D., Busnel, J.-M., Wittstock, G., Girault, H.H., Fountain Pen for SECM. Analytical Methods, 2010. DOI: 10.1039/C1030AY00096E.

- Olaya, A.J., Mendez, M.A., Cortés-Salazar, F., Girault, H.H., Voltammetric determination of extreme standard Gibbs ion transfer energy. Journal of Electroanalytical Chemistry, 2010, 644, 60–66.

- Cortés-Salazar, F., Busnel, J-M., Li, F., Girault, H.H., Adsorbed protein detection by scanning electrochemical microscopy. Journal of Electroanalytical Chemistry, 2009, 635, 69–74.

- Cortés-Salazar, F., Traeuble, M., Li, F., Busnel, J-M., Gassner, A., Hojeij, M., Wittstock, G., Girault, H.H.,. Soft Stylus Probes for Scanning Electrochemical Microscopy. Analytical Chemistry, 2009, 81, 6889–6896.

- Cortés-Salazar, F., Zhang, M., Becue, A., Busnel, J-M., Prudent, M., Champood, C., Girault, H.H., Human fingerprint imaging by Scanning Electro-Chemical Microscopy (SECM). Chimia, 2009, 63, 580.

- Li, F., Su, B., Cortés-Salazar, F., Nia, R.P., Girault, H.H.,. Detection of hydrogen peroxide produced at a liquid/liquid interface using scanning electrochemical microscopy. Electrochemistry Communications, 2009, 11, 473–476.

- Zhang, M., Su, B., Cortés-Salazar, F., Hojeij, M., Girault, H.H., SECM photography. Electrochemistry Communications, 2008, 10, 714–718.

Before this PhD thesis:

- Cortés-Salazar, F., Suarez, M.F., Barragan, D., Conductimetric and amperometric study of the bromate-phenol-sulphuric acid oscillating reaction. Indian Journal of Chemistry - Section A Inorganic, Physical, Theoretical and Analytical Chemistry, 2008, 47, 1775–1779.

- Cortés-Salazar, F., Avella-Moreno, E., Cortés, M.T., Suarez-Herrera, M.F., Study of the electrochemical oxidation process of 3,4-(methylenedioxy)phenylmethanol in non-aqueous solvents. Journal of Electroanalytical Chemistry, 2007, 606, 1–7.

- Cortés-Salazar, F., Barragan, D., Suarez, M.F., In situ monitoring of the uncatalyzed oscillating reaction of phenol and bromate in an acidic medium by ultrasonically enhanced chronoamperommetry. Electrochemistry Communications, 2004, 6, 470–474.